

# Origins of magnetite nanocrystals in Martian meteorite ALH84001

K.L. Thomas-Keprta<sup>a,\*</sup>, S.J. Clemett<sup>a,\*</sup>, D.S. McKay<sup>b</sup>, E.K. Gibson<sup>b</sup>,  
S.J. Wentworth<sup>a</sup>

<sup>a</sup> ESCG at NASA/Johnson Space Center, Houston, TX 77058, USA

<sup>b</sup> KR, ARES, NASA/Johnson Space Center, Houston, TX 77058, USA

Received 20 July 2008; accepted in revised form 18 May 2009; available online 16 June 2009

## Abstract

The Martian meteorite ALH84001 preserves evidence of interaction with aqueous fluids while on Mars in the form of microscopic carbonate disks. These carbonate disks are believed to have precipitated 3.9 Ga ago at beginning of the Noachian epoch on Mars during which both the oldest extant Martian surfaces were formed, and perhaps the earliest global oceans. Intimately associated within and throughout these carbonate disks are nanocrystal magnetites ( $\text{Fe}_3\text{O}_4$ ) with unusual chemical and physical properties, whose origins have become the source of considerable debate. One group of hypotheses argues that these magnetites are the product of partial thermal decomposition of the host carbonate. Alternatively, the origins of magnetite and carbonate may be unrelated; that is, from the perspective of the carbonate the magnetite is allochthonous. For example, the magnetites might have already been present in the aqueous fluids from which the carbonates were believed to have been deposited. We have sought to resolve between these hypotheses through the detailed characterization of the compositional and structural relationships of the carbonate disks and associated magnetites with the orthopyroxene matrix in which they are embedded. Extensive use of focused ion beam milling techniques has been utilized for sample preparation. We then compared our observations with those from experimental thermal decomposition studies of sideritic carbonates under a range of plausible geological heating scenarios. We conclude that the vast majority of the nanocrystal magnetites present in the carbonate disks could not have formed by any of the currently proposed thermal decomposition scenarios. Instead, we find there is considerable evidence in support of an alternative allochthonous origin for the magnetite unrelated to any shock or thermal processing of the carbonates.

© 2009 Published by Elsevier Ltd.

## 1. INTRODUCTION

The Allan Hills 84001 (ALH84001) meteorite is a coarse grained orthopyroxenite that solidified from a melt ~4.51 Ga ago (Nyquist et al., 2001). Approximately 600 Ma later (Borg et al., 1999), secondary carbonates were deposited by low temperature hydrothermal processes in pre-existing fractures and fissures within the groundmass.

The majority of these carbonates appear as circular or elliptical features, which range from ~10 to 300  $\mu\text{m}$  along the major axis (i.e., eccentricity >0.5). When viewed optically within an exposed fracture surface they range in color from gold to burnt orange in their centers and are typically surrounded by a thin black–white–black rim (Fig. 1A). The three dimensional morphology of these carbonates can best be described as an inverted conic frustum in which the base of the conic lies flush with the orthopyroxene (OPX) surface and the apex lies under the exposed surface (Fig. 1B). For reasons of brevity we will subsequently use the simpler, albeit less accurate, description of ‘disk’ when referring to these carbonates.

\* Corresponding authors. Tel.: +1 281 483 5029.

E-mail addresses: [kathie.thomas-keprta-1@nasa.gov](mailto:kathie.thomas-keprta-1@nasa.gov) (K.L. Thomas-Keprta), [simon.j.clemett@nasa.gov](mailto:simon.j.clemett@nasa.gov) (S.J. Clemett).

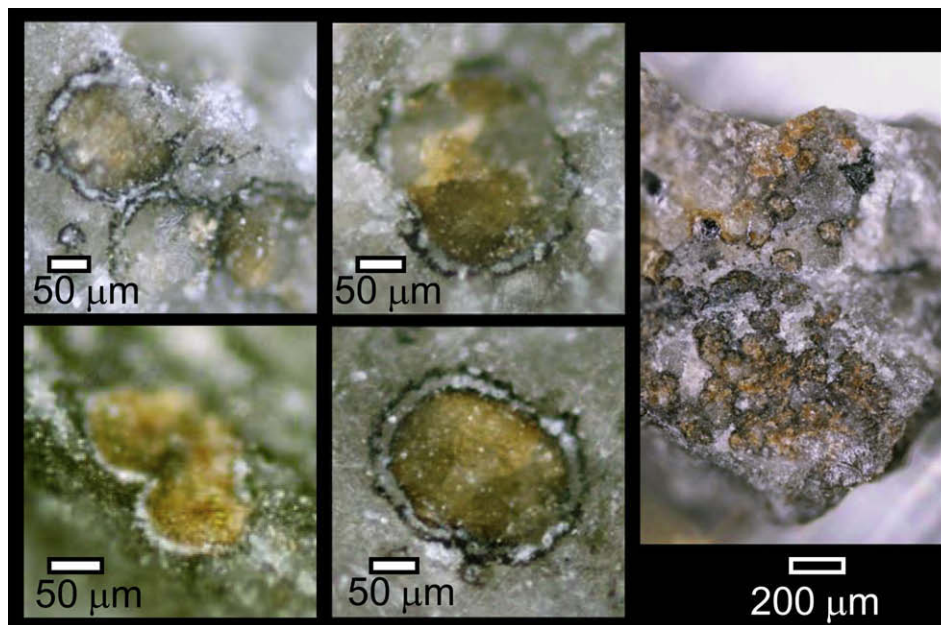


Fig. 1A. Optical images of ALH84001 disk-like carbonates. These disks precipitated in fractures produced during shock impacts while the meteorite was on Mars. The majority of these carbonates appear as circular or elliptical features which range from  $\sim 10$  to  $300 \mu\text{m}$  along the major axis. Visually they have colors that vary from gold to burnt orange in their centers which are typically surrounded by a thin black-white-black rim. Some carbonates occur as single entities while others are spatially associated and occur in groups of 10s of carbonates (image at far right). The black rims typically range from  $\sim 5$ – $10 \mu\text{m}$  in thickness and are composed primarily of nanophase magnetite embedded in a matrix of Mg-bearing sideritic carbonate while the white bands, typically  $\sim 10$ – $15 \mu\text{m}$  thick, are composed of nearly pure magnesite with minor Ca and nanophase magnetite.

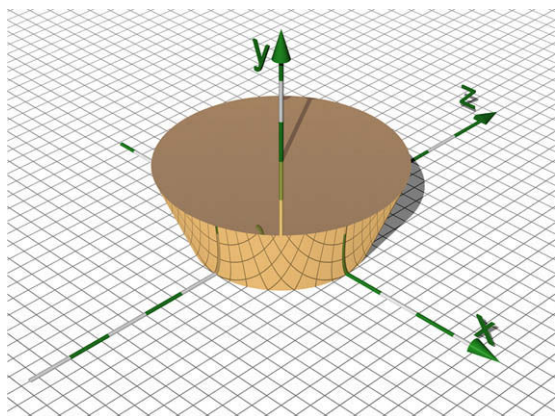


Fig. 1B. Illustration of an inverted conic frustum, that is, the polygon which remains after a cone is cut by a plane parallel to the base with the apical part removed and the remaining polygon inverted. While single ALH84001 carbonates have been loosely described as rosettes, globules, concretions, or pancakes, they are more accurately described as being shaped like an inverted conical frustum.

Chemically the disk carbonates have a complex mixed cation composition with an empirical formula  $(\text{Fe}_x\text{Mg}_y\text{Ca}_z\text{Mn}_{[1-x-y-z]})\text{CO}_3$  where  $x + y + z = 1$ . The values of  $x$ ,  $y$ , and  $z$  vary with radial distance in such a way that the carbonate disks can be envisioned as being composed of three concentric annular zones; starting from the center there is an inner central and outer core surrounded by a

thin rim. Embedded within these carbonates are discrete nanocrystal magnetites ( $\text{Fe}_3\text{O}_4$ ) that exhibit super-paramagnetic to single-domain properties (Muxworthy and Williams, 2008). While the largest population of these magnetites occurs within the rim zone of the carbonate disks, e.g., McKay et al. (1996) and Thomas-Keprta et al. (2000a), a small but significant fraction is also found within the inner and outer core zones.

When the carbonate disks were initially characterized, they were interpreted as products of high temperature processes ( $T > 573 \text{ K}$ ) (Harvey and McSween, 1996; Mittlefehldt, 1994a; Mittlefehldt, 1994b; Scott et al., 1997). Subsequently, isotopic and chemical data has forced a revision in this interpretation and it is now generally accepted they were deposited by low temperature ( $T < 573 \text{ K}$ ) hydrothermal processes (Eiler et al., 2002; Kent et al., 2001; Kirschvink et al., 1997; McSween and Harvey, 1998; Romanek et al., 1994; Saxton et al., 1998; Treiman, 1997; Valley et al., 1997; Warren, 1998). While the consensus of opinion on the temperature of formation of the carbonates has converged, that of their subsequent thermal evolution has not because of the differing hypotheses invoked to explain the presence of the nanocrystal magnetites present within the carbonate. To first order, these magnetites were either already present when the carbonates formed and so became embedded during carbonate deposition, or they were formed *a posteriori* by partial thermal decomposition of the pre-existing carbonate. In the latter case, the heating of the meteorite is envisioned to have occurred through the adiabatic propagation of one or more impact shock events.

ALH84001 shows evidence of having undergone multiple impact events, the last resulting in its ejection from Mars, e.g., Treiman (1998). In general, the peak shock pressures experienced by Martian meteorites are thought to range from less than 14 gigapascals (GPa) up to  $\sim 55$  GPa (Fritz et al., 2004; Fritz et al., 2003; Langenhorst et al., 2000; Stöffler, 2000; Treiman, 2003; van der Bogert et al., 1999). These estimates are based on the conversion of plagioclase to either a diaplectic ‘maskelynite’ ( $\sim 14$ – $45$  GPa) or melt glass ( $>45$  GPa) with a resulting increase in the refractive index and/or Raman band broadening, compared to unshocked plagioclase (Fritz et al., 2004). Specifically, for ALH4001, estimated values for peak shock pressure have evolved over time –  $\sim 50$ – $60$  GPa (Langenhorst et al., 2000);  $<40$  GPa (van der Bogert et al., 1999);  $\sim 35$ – $40$  GPa (Stöffler, 2000);  $35.7 \pm 4.5$  GPa (Fritz et al., 2003);  $>35$ – $40$  GPa (Fritz et al., 2004) – with the best current estimate at  $32 \pm 1$  GPa (Fritz et al., 2005).

The extent to which impact shocks to ALH84001 lead to thermal excursions that could have partially decomposed the ALH84001 carbonate disks remains ambiguous (note, in this context any impacts occurring in the  $\sim 600$  Ma prior to carbonate formation have no bearing). Results from simulations of shockwave propagation through compositionally and texturally complex matrices are computationally difficult and sensitive to initial starting conditions, but do indicate that shock heating would have been highly heterogeneous at all size scales. Using a Hugoniot equation-of-state experimentally derived from Stillwater pyroxenite, Twin Sister dunite (Stöffler, 1982), and a gabbroic rock (Trunin et al., 2001), the post-shock temperature elevation for ALH84001 associated with a 32 GPa shock event lies in the range of  $\sim 373$ – $383$  K (Fritz et al., 2005). If we assume ALH4001 prior to ejection was at the average Martian ground-surface temperature of  $\sim 230$  K and that the peak shock pressure experienced corresponded to this final ejection event (note, paleomagnetic data of Weiss et al. (2000) suggest the interior of ALH84001 was not heated above  $\sim 313$  K), this would imply an average maximum heating, post-ejection, to a temperature of  $\sim 610$  K. This is in broad agreement with recent (U–Th)/He analyses of ALH84001 phosphate grains that suggest a peak ejection temperature of  $\sim 673$  K or less (Min and Reiners, 2006).

To address these unresolved questions we have utilized focused ion beaming techniques in conjunction with conventional ultramicrotomy to provide the most detailed picture yet of the spatial, structural and chemical relationships present within ALH84001 carbonate disks. We have then used these new observations to evaluate the merits of both theoretical and experimental attempts to reproduce ALH84001-like disks with embedded magnetites through partial thermal decomposition of Fe-bearing carbonate. In the larger context, resolving or at least constraining the origin of the magnetites within ALH84001 carbonate disks has importance in that it has been previously suggested that the precipitation of the carbonate disks may have been facilitated through biogenic activity (McKay et al., 1996) and that a fraction of the embedded magnetites exhibit chemical and physical features identical to those produced by contemporary magnetotactic bacteria (McKay et al.,

1996; Thomas-Keprta et al., 2000a; Thomas-Keprta et al., 2001; Thomas-Keprta et al., 2002).

## 2. METHODOLOGY

### 2.1. ALH84001 carbonate disks

Table 1 lists the ALH84001 rock splits used in the research presented herein. Prior to any extraction, fracture surfaces containing carbonate disks were first characterized by optical and electron microscopy. This involved optical imaging under both bright and dark-field illumination conditions. Given the topographic variations present within a given fracture surface, a long working distance Nikon Eclipse ME600 microscope was used for this task. Due to the low numerical apertures associated with long working distance microscope objectives, the depth-of-field was

Table 1  
Rock splits of Martian meteorite ALH84001.

Split	Parent
157	21
158	40
160	2
161	17
162	41
163	69
164	76
165	103
166	147
174	39
175	39
180	69
181	69
182	69
184	14
185	14
186	14
188	69
189	26
190	147
191	128
192	34
193	134
195	59
197	40
198	0
200	0
208	14
217	69
283	214
284	208
286	218
289	202
297	213
372	239
374	103
383	66
384	61
385	104
386	247
388	153

generally insufficient for any single image to be in complete focus. We therefore acquired image stacks over a range of focus planes for each imaged sample surface, which were then subsequently combined using a complex-wavelet algorithm (Forster et al., 2004) to generate a single in-focus image with an extended depth-of-field. After optical imaging, selected fracture surfaces were transferred to 1/2-inch Al pin mounts and attached using conductive C tape before being lightly coated with either C or Pt (<1 nm) to enable imaging using a JEOL 6340F field-emission scanning electron microscope (SEM) at 15 kV. In one case, a sample chip containing a large, elongated ( $\sim 250 \times 115 \mu\text{m}$ ) carbonate disk (a.k.a. 'Ear' carbonate) was also analyzed using a Cameca SX100 electron probe microanalyzer at 15 kV and 10 nA to determine both major and minor element compositions. Both quantitative linescans and qualitative 2-D element maps were collected at a lateral spatial resolution of  $\sim 1 \mu\text{m}$  for C (dolomite standard), Mg (kaersutite standard), Si (kaersutite standard), S (troilite standard), Ca (calcite standard), and Fe (kaersutite standard).

After the initial in situ characterization, parts of selected carbonates were extracted for analysis at higher resolution using transmission electron microscopy (TEM) and energy dispersive X-ray spectroscopy (EDX). Several extraction procedures were utilized; at its simplest, this involved the direct mechanical separation of either a complete or partial carbonate disk from its OPX fracture surface using a pair of surgical austenitic stainless steel tweezers. Removed carbonate fragments were then crushed between a pair of clean glass microscope slides to reduce the average particle size to less than  $50 \mu\text{m}$ . From this crushed material, individual fragments of carbonate, typically less than  $20 \mu\text{m}$  in size, were dry-picked and embedded within a small drop of uncured Embed 812 epoxy resin atop an epoxy-potted butt. After curing the carbonate, embedded epoxy samples were sectioned into 70–100 nm thick electron transparent sections using a Reichert MT 7000 ultramicrotome equipped with a  $45^\circ$  angle diamond knife. Individual sections were 'floated off' the diamond knife after cutting using a triple distilled water bath and transferred to either Cu or Au 200 mesh thin-bar TEM grids.

While ultramicrotomy is the *de facto* preparation technique for TEM thin sections, it proved to have two significant disadvantages in the case of ALH84001 carbonate disks. First, all essential spatial information is lost between the final thin section and the source carbonate disk from which it was extracted. Second, the risk exists of potential aqueous alteration and/or contamination when a cut thin section is floated-off off the diamond ultramicrotome knife using a water bath. To circumvent these issues, we used a second approach for the preparation of carbonate sections, that being a focused ion beam (FIB) instrument (Giannuzzi and Stevie, 1999). In the FIB technique, a tightly focused ion beam is used to selectively cut a TEM section directly from the surface of a sample; this permits site specific extraction with complete preservation of spatial location. Furthermore, FIB section preparation introduces very little mechanical stress, so that the size of the thin section that can be obtained is limited only by the tendency of large area surfaces to eventually warp or curl due to differences in sur-

Table 2

Split number and size of ALH84001 focused ion beam sections.

Carbonate section	Split number	FIB extracted section size ( $\mu\text{m}$ )
<i>Texas</i> , Section 1	,286	$\sim 15 \times 8$
<i>Texas</i> , Section 2	,286	$\sim 17 \times 5$
<i>Posterboy</i> , Section 1	,386	$\sim 17 \times 10$
<i>Posterboy</i> , Section 2	,386	$\sim 16 \times 11$
<i>Posterboy</i> , Section 3	,386	$\sim 15 \times 9$
<i>Posterboy</i> , Section 4	,386	$\sim 13 \times 8$
<i>Posterboy</i> , Section 5	,386	$\sim 15 \times 10$

face tension between and across adjacent faces. In practical terms for  $\sim 150 \text{ nm}$  thick carbonate thin sections we found the length-to-thickness ( $l/w$ ) ratio could not practically exceed  $\sim 200$ , with the largest FIB section extracted here being  $\sim 20 \mu\text{m}$  in length ( $l/w \sim 130$ ).

In all, seven FIB thin sections were acquired using the standard 'H'-bar extraction procedure from two carbonates on unrelated fracture surfaces as documented in Table 2. Sections were prepared using either a FEI Dual-Beam Strata 237 ('*Texas*' Sections 1 and 2; '*Posterboy*' Sections 1–4) or Strata 400 ('*Posterboy*' Section 5) workstations. Both instruments were equipped with a field emission electron source, a  $\text{Ga}^+$  ion source, a 30 kV scanning TEM detector, an EDX spectrometer, and an Omniprobe in vacuo micro-manipulator. Sample mounting used the same 1/2-inch Al pin mounts used in the preliminary SEM imaging. The first two FIB thin sections were acquired from an interior carbonate fragment designated '*Texas*' plucked from a freshly exposed OPX fracture surface of rock split ALH84001,286. Both sections were transferred directly to a continuous C film Cu TEM grid. The remaining five FIB thin sections were extracted from both core and rim of a carbonate disk designated '*Posterboy*' located on a freshly exposed fracture surface of rock split ALH84001,386. Note that for these sections the carbonate was not removed from its fracture surface, rather the entire chip containing the fracture surface was mounted in the FIB instrument. This was done in order to permit the study of both carbonate and the interface with the surrounding and underlying OPX. Each removed thin section was welded on one or both sides in situ to a Cu crescent TEM mount.

Both ultramicrotome and FIB thin sections were analyzed using either a JEOL 2000 FX 200 kV STEM and/or a JEOL 2500SE 200 kV field emission STEM. Both instruments were equipped with light element ( $Z > 5$ ) Si-drift EDX detectors (Noran System 6), and in the case of the 2500SE, a modified objective-lens pole piece allowed a collimator-equipped 0.3 steradian large area ( $50\text{-mm}^2$ ) EDX detector for increased sensitivity. The JEOL 2500SE instrument was also equipped with a Gatan Tridim Imaging Filter for energy-filtered imaging and electron energy-loss spectroscopy, and a high-angle annular darkfield detector for  $z$ -contrast imaging.

## 2.2. Roxbury siderite

To investigate the chemical compositions of magnetite formed from the decomposition of Fe-rich carbonates, a

186 g sample of siderite ( $\text{FeCO}_3$ ) from the Roxbury iron mine in Litchfield, Connecticut was obtained from the Excalibur Mineral Company. Roxbury siderite has previously been reported as having a bulk composition of  $(\text{Fe}_{0.84}\text{Mg}_{0.10}\text{Mn}_{0.04}\text{Ca}_{0.02})\text{CO}_3$  (Lane and Christensen, 1997) and provides (compositionally) a reasonable terrestrial analog to the Fe-rich component of ALH84001 carbonates disks, e.g., a composition of  $(\text{Fe}_{0.750}\text{Mg}_{0.240}\text{Mn}_{0.003}\text{Ca}_{0.004})\text{CO}_3$  was calculated by Treiman (2003) for the inner rim of a carbonate disk.

Three separate sample fractions of Roxbury siderite were prepared by mechanical abrasion from the bulk sample. One fraction served as a control while the remaining two were thermally decomposed. In one case, decomposition occurred under a very slow, controlled heating rate, while in the other, the heating event was essentially instantaneous. We will, for brevity, subsequently refer to these heating scenarios as either being ‘*slow*’ or ‘*fast*’, respectively.

In the ‘*slow*’ heating experiment the large sealed quartz tube (LSQT) method was used to produce a closed reaction under conditions approximating thermal equilibrium (Lauer et al., 2005). In this method, the siderite sample is placed in small open quartz crucible, which is in itself within a larger evacuated quartz tube, along with a second crucible containing lime ( $\text{CaO}$ ). The lime serves as a sink for  $\text{CO}_2$  liberated during carbonate decomposition and so acts to maintain a constant oxygen fugacity ( $f_{\text{O}_2}$ ). The whole assembly is heated in a vertical tube furnace, with the temperature being controlled using a J-type thermocouple attached to the LSQT. In our experiment, the siderite sample was heated at a rate of  $1 \text{ K} \cdot \text{min}^{-1}$  to a maximum temperature of 848 K, after being held at this temperature for 24 h, it was to be cooled back to room temperature at a rate of  $\sim -10^{-2} \text{ K} \cdot \text{s}^{-1}$ .

In the ‘*fast*’ heating experiment, the siderite sample was heated under vacuum with a pulsed  $10.6 \mu\text{m}$   $\text{CO}_2$  laser (PRF-150 Laser Science, Inc.) focused onto the sample using a Cassegrainian microscope objective. The temporal profile of the  $\text{CO}_2$  laser pulse had an  $\sim 300 \text{ ns}$  initial spike accounting for  $\sim 30\%$  of the total pulse energy which was then followed by a slow oscillatory decay extending up to  $\sim 1\text{--}2 \mu\text{s}$ . Results using a thin-film Pt thermocouple suggest that the heating rates were on the order of  $\sim 10^8\text{--}10^9 \text{ K} \cdot \text{s}^{-1}$  with a peak temperature of  $\sim 573\text{--}673 \text{ K}$  being reached at the laser focus (Zenobi et al., 1995).

### 3. RESULTS

#### 3.1. ALH84001 carbonate disks

##### 3.1.1. Spatial location and distribution of carbonate disks

Carbonates account for  $\sim 1\%$  by volume of ALH84001 and are distributed throughout the multiple internal fracture surfaces that pervade the meteorite (Mittlefehldt, 1994a; Mittlefehldt, 1994b). While single isolated carbonates do occur, most often they are found in clusters ranging from a few to tens of carbonates, some of which appear partially fused (Fig. 1A). These carbonates are not simple vein-filling deposits since their center-of-mass lies not

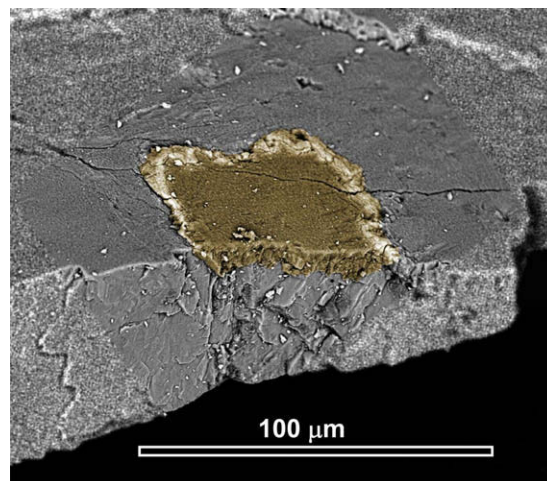


Fig. 1C. Backscatter electron image (BSE) of a partial, false-colored ALH84001 carbonate disk embedded within the OPX matrix of a freshly fractured chip. The uppermost surface of the carbonate lies flush with the surrounding OPX (gray). The body of the carbonate disk is inset within a form-fitting depression  $\sim 5$  to  $8 \mu\text{m}$  deep within the OPX. All ALH84001 carbonate disks we have investigated have this common morphological context.

between the adjacent fracture surfaces, but rather, is offset such that the carbonate disk is either mostly or wholly inset within a form-fitting pit in one or other surface. Intriguingly, in fractures in which multiple carbonates are present, the pits in which each of the carbonates are inset all lie on the same OPX surface. *A priori* it might be expected that the carbonate pits would be evenly distributed between the adjacent fracture surfaces, however, this is not so.

##### 3.1.2. External shape of ALH84001 carbonate disks

The carbonate disks within each OPX pit show a relatively constant thickness that does not change, proceeding from the core outward, until the onset of the inner magnetite band where upon it abruptly decreases, in an approximately linear fashion, all the way to the carbonate edge. Hence, as noted previously, the most accurate terminology describing this shape is that of an inverted conic frustum<sup>1</sup>, see Fig. 1B, as opposed to the more widely used, but inaccurate description, as disks, rosettes, or pancakes. In general, while the diameter of carbonate disks can vary by a factor of 10 or more, even within a single fracture surface, the thickness is relatively invariant being typically  $\sim 10\text{--}15 \mu\text{m}$ . Consequently this implies that the radial thickness of the carbonate rims must also be similarly invariant, as is observed with a typical width of  $\sim 10 \mu\text{m}$ .

<sup>1</sup> In the rim region the inner and outer magnetite bands do not lie perpendicular to the fracture surface but rather are canted outward with acute angles  $\phi$  and  $\theta$ , where  $\phi > \theta$  and  $\theta \sim (90 - \phi)$ , with  $\phi$  being the angle between the generatrix and the axis of the conic frustum.

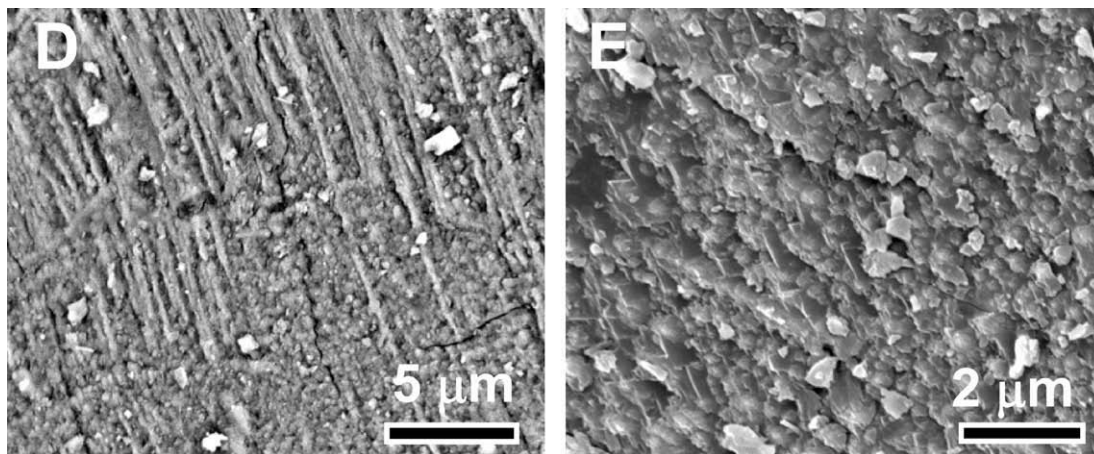


Fig. 1D and 1E. SEM images typical of the striated/ridged texture that characterize the OPX fracture surface adjacent to carbonate disks. Such textures could result from fluid dissolution of the OPX surface.

### 3.1.3. Morphology, textures, and relationship of carbonate to OPX

Carbonates are inset within form fitting pits and lie flush with the OPX fracture surface as illustrated in Fig. 1C. The OPX fracture surfaces in which carbonates are found all demonstrate an aligned striated texture, Fig. 1D and 1E, which can be interpreted as the result of differential weathering of OPX lamellae that is characteristic of partial aqueous chemical dissolution (Velbel, 2007). This texture contrasts sharply with that of the OPX underlying the carbonate which forms the base of the pits, which has a loosely oriented botryoidal or micro-dendritic texture (Fig. 1F and 1G). These Martian ‘microdenticles’ share some physical similarities to terrestrial denticles formed by the low temperature aqueous alteration/weathering of chain-silicates<sup>2</sup> (e.g., pyroxene, amphibole) (Velbel, 2007; Velbel et al., 2007). Although the majority of terrestrial denticles are larger in size than their putative Martian counterparts (up to 10s of microns in length) the lower end of the size distribution does overlap that of the Martian microdenticles (Velbel, 2007; Velbel et al., 2007). Hence, this suggests that the OPX textures, including pits and etched surfaces, formed either prior to, or contemporaneously, with the deposition of carbonate through a process of chemical dissolution of the silicate.

In the terrestrial context, aqueous weathering of chain-silicates results in the concurrent formation of other low temperature secondary minerals such as kaolinite

( $\text{Si}_2\text{Al}_2\text{O}_5(\text{OH})_4$ ), smectite<sup>3</sup> and serpentine<sup>4</sup> clay minerals, and oxyhydroxides such as goethite ( $\alpha\text{-FeOOH}$ ) (Velbel, 2007). While there have been sporadic observations of smectites in ALH84001 (Thomas-Keprta et al., 2000b), generally the most remarkable observation is how scarce they appear to be. Given the age and uncertainty in the history of ALH84001, it is possible that such minerals might have once been present but were not preserved (Velbel, 2007), nevertheless the lack of such weathering minerals associated with ALH84001 fracture surfaces and their associated carbonate disks has yet to be satisfactorily explained and remains an enigma.

### 3.1.4. Surface textures of carbonate disks

SEM images of the upper surfaces of carbonate disks exposed to fracture space are shown in Fig. 1H and 1I. At low magnification, carbonates display a pitted texture interspersed with lamellar striations, while at high magnification the surface texture is composed of discrete particles ranging from  $\sim 20$  to 250 nm with ovoid to irregular shapes. This texture is unlikely to represent the primordial texture of the carbonate at the time of its deposition, but rather represents the products of subsequent superficial erosion and carbonate dissolution during post-depositional fluid interactions.

### 3.1.5. Composition of ALH84001 carbonate disks

The largest carbonate within a cluster of carbonates on a freshly exposed fracture surface of ALH84001,286 was designated as the ‘Ear’ carbonate (Figs. 2A and 2B). This ‘Ear’ carbonate provides a good example of the typical carbonate

<sup>2</sup> Pyroxenes have the general formula  $\text{XY}(\text{Si,Al})_2\text{O}_6$  (where X generally represents Na, Mg, Ca, and  $\text{Fe}^{2+}$  and Y generally represents Mg, Al, Sc, Ti, V, Cr, Mn, and  $\text{Fe}^{3+}$ ). Amphiboles have chemical compositions and general characteristics that are similar to the pyroxenes although extensive substitution of Si by Al can occur. The chief difference between amphiboles and pyroxenes is that the basic structure of an amphibole is a double chain of  $\text{SiO}_4$  tetrahedra compared to a single chain structure for pyroxene.

<sup>3</sup> The smectite group of minerals includes dioctahedral phyllosilicates including  $\text{Fe}^{3+}$ -rich nontronite ( $\text{Na}_{0.3}\text{Fe}_2(\text{Si,Al})_4\text{O}_{10}(\text{OH})_2 \cdot n\text{H}_2\text{O}$ ),  $\text{Fe}^{3+}$ -poor montmorillonite ( $(\text{Na,Ca})_{0.33}(\text{Al,Mg})_2\text{Si}_4\text{O}_{10}(\text{OH})_2 \cdot n\text{H}_2\text{O}$ ) and trioctahedral clays including saponite with the general chemical formula  $\text{Ca}_{0.25}(\text{Mg,Fe}^{2+})_3(\text{Si,Al})_4\text{O}_{10}(\text{OH})_2 \cdot 4\text{H}_2\text{O}$ .

<sup>4</sup> Serpentine represents a group of hydrous Mg, Fe-phyllsilicate ( $(\text{Mg,Fe})_3\text{Si}_2\text{O}_5(\text{OH})_4$ ) minerals.

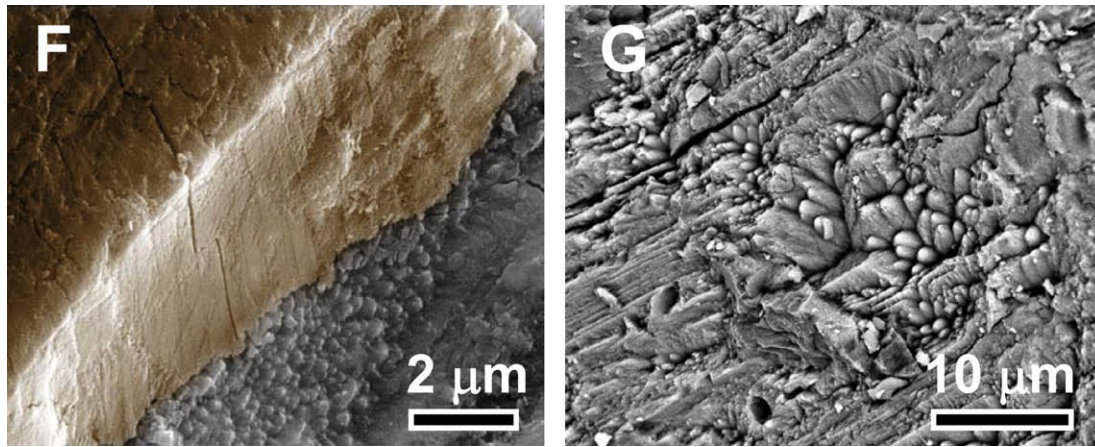


Fig. 1F and 1G. SEM views of the typical OPX surface texture that underlies carbonate disks (residual overlying carbonate is shown false colored in orange in 1F), composed of loosely oriented, botryoidal or micro-denticular features with apices that range from sharply pointed to rounded. In terrestrial weathered silicates, the nature of such denticulated features is strongly influenced by the composition of the dissolution fluid and its degree of undersaturation relative to the etched surface, see Velbel (2007) and Velbel et al. (2007) and references therein. While the Martian microdenticles are smaller in scale than those observed in terrestrial silicates, there is sufficient similarity in the textures of the Martian and terrestrial denticles to permit the interpretation that aqueous dissolution could account for their presence. (For interpretation of the references to color in this figure legend, the reader is referred to the web version of this paper.)

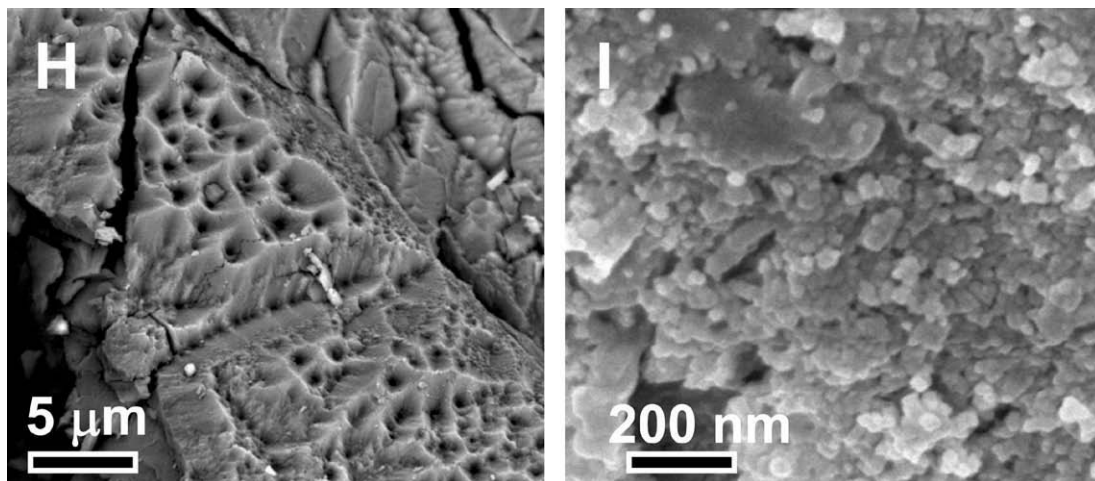


Fig. 1H and 1I. SEM view (H) showing the characteristic deeply ridged and pitted (e.g., honeycomb) textures of the carbonate disk contiguous with the OPX fracture surface. At higher magnification (I) this surface texture is comprised of a matrix of spheroidal, ovoid, and irregular-shaped grains ranging from  $\sim 10$  to 300 nm along the longest axis. Note that this surface texture is independent of the underlying carbonate composition, that is, the magnetite-rich rims display a texture nearly identical to that of the core carbonate.

disk. While there are compositional variations between carbonate disks, both on the same and different fracture surfaces, many of the broader characteristics demonstrated by the ‘*Ear*’ carbonate are representative of all carbonates, albeit to differing degrees. Hence we have used the ‘*Ear*’ carbonate as the archetype to describe the spatial and compositional relationships exhibited by carbonate disks<sup>5</sup>. Fig. 2A shows quantitative 2-D cation distributions

<sup>5</sup> For example, the Ca-rich cores characteristic of the larger carbonates are generally absent in those carbonates that populated the lower end of the carbonate size distribution.

obtained by electron microprobe analyses of the ‘*Ear*’ carbonate, while Table 3 lists the bulk composition.

While at the one micrometer resolution limit of the electron microprobe the variations of Ca, Mg, Fe, and Mn cations appear complex and sometimes chaotic, at a broader scale clear radial symmetric zoning patterns are apparent that can be described as three approximately equivolume concentric zones<sup>6</sup>: an inner core ( $\sim 50$   $\mu\text{m}$  radius along the major axis;  $\sim 30$  vol.%), surrounded by an outer core

<sup>6</sup> This delineation into three zones is purely a construct to simplify the description of the carbonates and does not necessarily imply any underlying significance.

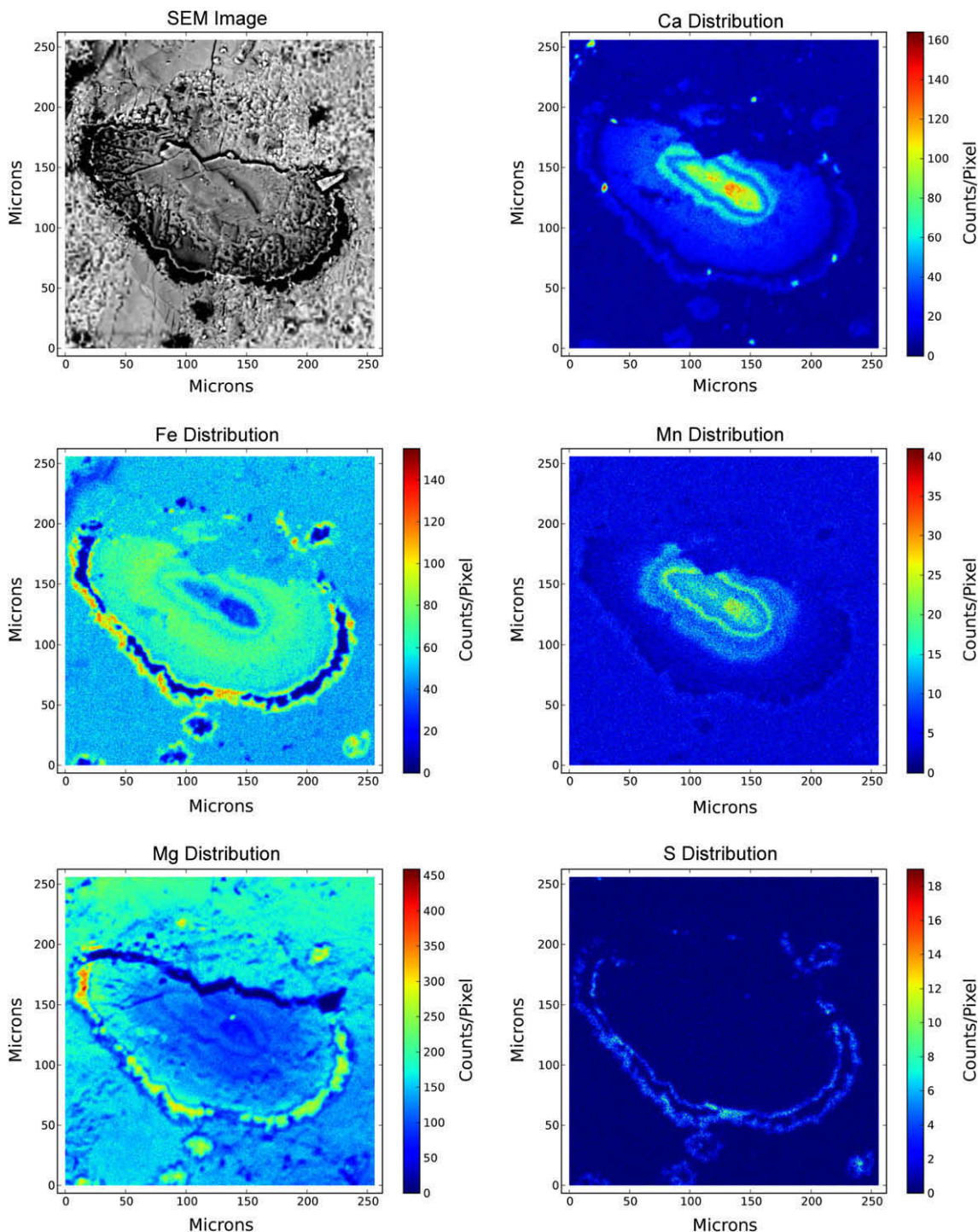


Fig. 2A. BSE view of a single ALH84001 carbonate disk, designated as ‘Ear’ carbonate and its associated quantitative element distribution maps for Ca, Fe, Mn, Mg, and S, acquired by wavelength dispersive electron microprobe analyses using a  $\sim 1 \mu\text{m}$  probe beam. The region we designate as the inner core is characterized a significant enrichment in Ca and Mn, with both showing oscillatory, radial zoning patterns. The region that separates the inner core from the rim we designate as the outer core. The transition between the inner and outer core is characterized by a sharp ( $< 1 \mu\text{m}$ ) compositional boundary in Ca and Mn distribution. The major cation distribution (Ca, Mg, Fe, and Mn) in this outer core is radially invariant, that is it changes little with increasing radius. Enrichment of S in the inner and outer magnetite-rich rims is attributed to the presence of nanophase Fe-sulfides.

( $\sim 20 \mu\text{m}$  thick radial band;  $\sim 30 \text{ vol.}\%$ ), which itself is surrounded by a rim ( $\sim 20 \mu\text{m}$  thick radial band;  $\sim 40 \text{ vol.}\%$ ) as illustrated in Fig. 2B.

The simplest of the three zones is the rim which is composed of a relatively thick band of almost pure magnesite ( $\text{MgCO}_3$ ) ( $> 90 \text{ mol.}\%$  Mg) which is bordered on its inner

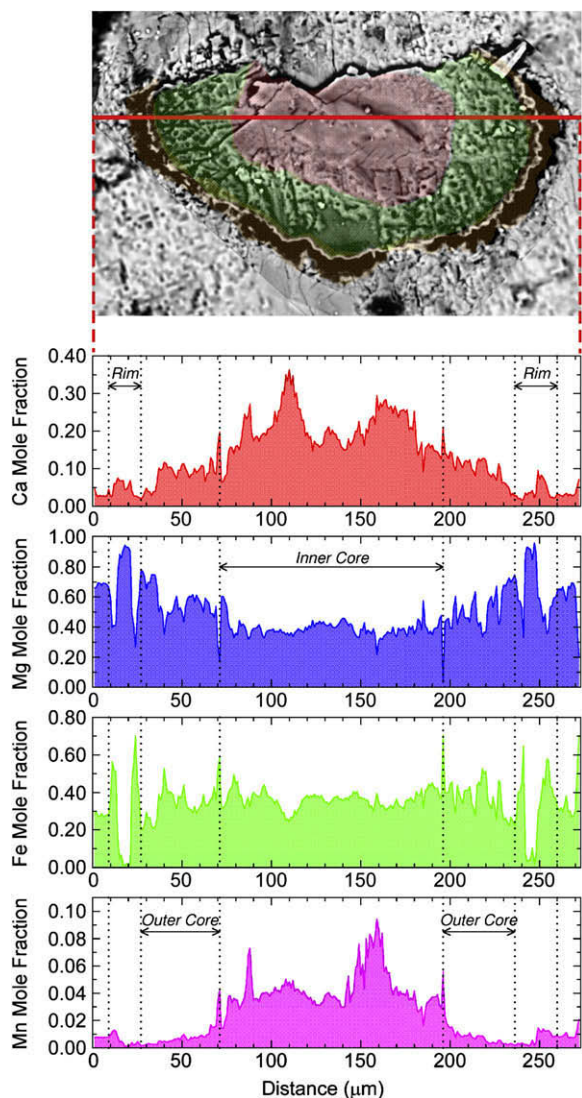


Fig. 2B. Upper image: colored image of the 'Ear' carbonate,  $\sim 250 \times 115 \mu\text{m}$  in size, shown in 2A indicating approximate contours of the inner and outer cores, and rim. The solid red line bisecting the carbonate represents the axis along which 151 electron microprobe spot analyses were acquired. Lower image: cation mole fractions for 'Ear' carbonate regions analyzed along the solid red line. Transitions between the inner and outer core and rim appear as abrupt changes ( $< 1 \mu\text{m}$ ) in the carbonate cation composition as indicated. (For interpretation of the references to color in this figure legend, the reader is referred to the web version of this paper.)

and outer perimeter by thin Fe-rich bands composed primarily of magnetite embedded in a Mg:Fe ( $\sim 60:40$ ) carbonate matrix. Within the rim lies the outer and inner cores of which the latter is the compositionally most complex. At its very center, the inner core has a Ca-rich (Ca:Mg:Fe:Mn  $\sim 45:30:15:10$ ) nucleus ( $75 \times 20 \mu\text{m}$  major/minor axis) accounting for  $\sim 5\%$  of the total volume of the carbonate. This is encircled by a thin ( $\sim 10 \mu\text{m}$ ) Ca-rich halo (Ca:Mg:Fe:Mn  $\sim 30:30:30:10$ ) separated from the nucleus by a thin band ( $\sim 10 \mu\text{m}$ ) of Mg-Fe-rich carbonate (Mg:Fe:Ca:Mn  $\sim 40:40:16:4$ ). Beyond the Ca-rich halo, the Ca concentration decreases proportionally to increasing Mg, while Fe concentration remains relatively invariant. Although Mn is always the minor cation, its relative abundance closely correlates with that of the Ca cation distribution, and is loosely inversely correlated to the Fe cation distribution. The outer core which separates the inner core from the rim is characterized by Ca, Mg, Fe, and Mn cation distributions that do not change significantly with changing radius, i.e., they are radially invariant.

Another way to visualize the compositional differences between the inner and outer cores and rim is to use the Ca, Mg, Fe + Mn ternary diagram in which the carbonate compositions associated with these three zones can then be seen to form three separate, but partially overlapping, density ellipses (Fig. 2C). For comparison to Fig. 2C, the Ca, Mg, Fe ternary diagram outlining the stability fields for calcite ( $\text{CaCO}_3$ ), dolomite ( $\text{Mg,Ca}(\text{CO}_3)_2$ ) – ankerite ( $\text{Ca,Fe}(\text{CO}_3)_2$ ), and the complete magnesite-siderite solid solution series is shown in Fig. 2D. It is apparent that the compositions of many ALH84001 core and rim carbonates lie outside of these thermodynamic stability fields. Combined with the complex radial oscillatory zoning and sharp compositional boundaries observed, it is clear that ALH84001 carbonate disks represent assemblages in a high degree of disequilibrium, consistent with the chemical and isotopic findings from previous studies, e.g., Treiman (1997) and Valley et al. (1997). If the carbonate disks evolved by successive radial deposition of carbonate from a central nucleus it would therefore imply that the pore- or fracture-filling fluid was out of thermodynamic equilibrium with the surrounding rock matrix, and that variations in diffusion parameters led to the development of the complex deposition patterns. This is commonly observed in environments where the rate of fluid-rock mass transfer is limited by diffusion. The observed complex mineral zonation patterns thus record the changes in the fluid composition caused by variable kinetic dispersion and fluid flow rates at the site of crystal growth. Oscillatory patterns formed where the rate of

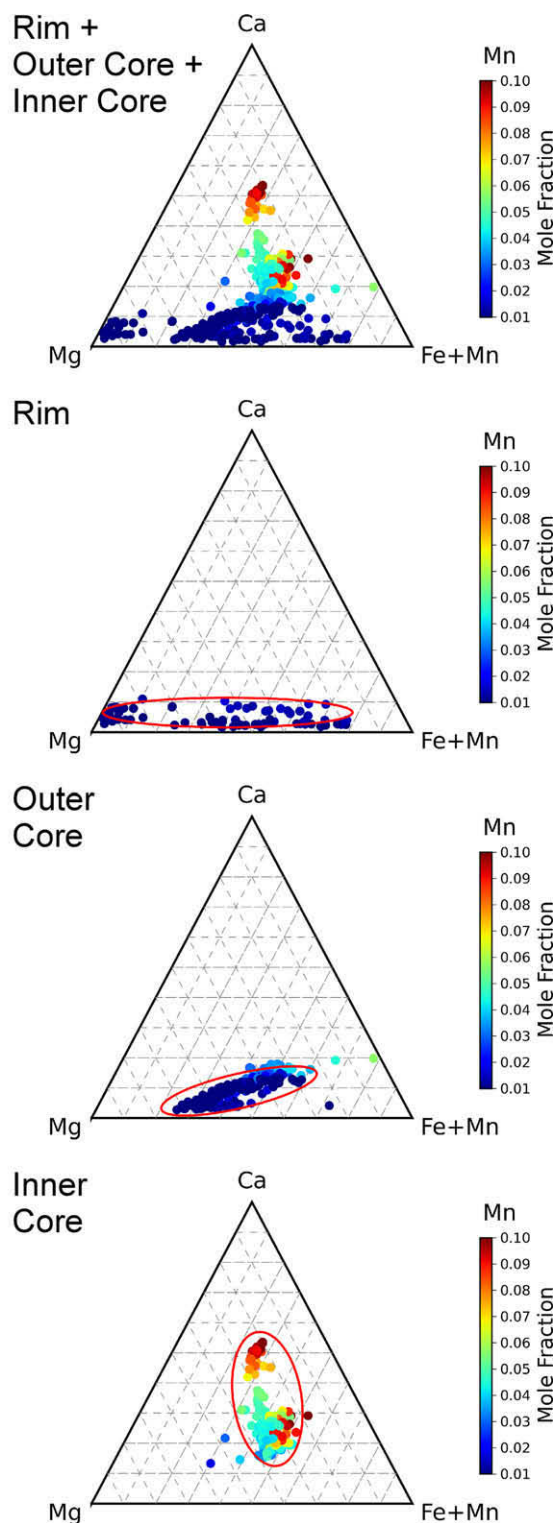
Table 3  
Electron microprobe analyses of ALH84001 'Ear' carbonate.

ALH84001 Carbonate Disk 'Ear' carbonate	Min. (mol.%)	Max. (mol.%)	Ave. 1 (mol.%)	Weighted Ave. 241 analyses (mol.%)	ALH84001 Carbonate Ave. (mol.%) (Mittlefehldt, 1994b)	Roxbury Siderite Ave. (mol.%) (Lane and Christensen, 1997)
Fe	0.011	0.731	$0.336 \pm 0.102$	0.375	0.294	0.84
Mg	0.028	0.951	$0.462 \pm 0.147$	0.493	0.580	0.10
Ca	0.015	0.526	$0.172 \pm 0.115$	0.114	0.115	0.02
Mn	0.001	0.098	$0.030 \pm 0.024$	0.018	0.011	0.04

diffusion was sluggish enough to permit the establishment of sharp stationary chemical potential gradients.

### 3.2. ALH84001 FIB sections

SEM images of ‘Texas’ and ‘Posterboy’ carbonates prior to and after FIB extraction are shown in Figs. 3A and 3B,



respectively. TEM overview images of ‘Texas’ FIB Sections 1 and 2, and ‘Posterboy’ FIB Sections 1–5 are shown in Figs. 3C–3I, respectively. Rather than discuss each section individually, for succinctness Fig. 4 summarizes the underlying characteristics of the rim and core carbonate structures observed in these sections.

#### 3.2.1. Sections of rim carbonate: ‘Posterboy’ Sections 1–5

Compositionally the inner and outer magnetite rims are composed of an approximately 50:50 vol.% mixture of fine grained carbonate and single crystal magnetites (Figs. 2A and 2B; Fig. 5A), with Fe-sulfides also present as a minor phase (Fig. 5A). The carbonate has a Mg:Fe cation ratio of approximately 40:60 with minor and trace amounts of Mn and Ca, respectively. Pervading this carbonate is a poorly constrained, minor amorphous silica phase (Fig. 5A). Although this silica phase is also present throughout the entire carbonate, it is enriched ~3-fold within these rims. In some cases, we have also observed it to constitute a major phase and note that Si-rich veins in ALH84001 carbonates were also described by McKay et al. (1998). The magnetites are predominately stoichiometrically pure  $\text{Fe}_3\text{O}_4$  (Fig. 5B), although some do contain Cr and/or Al (Fig. 5C) as noted previously by Thomas-Keprta

Fig. 2C. Ternary cation plots for ‘Ear’ carbonate based on 449 electron microprobe spot analyses. In each plot the three cation end-members are Ca, Mg, and (Fe + Mn) and each data point is colored according to the mole fraction of Mn. In the top plot all 449 data points are shown together while in the lower plots, data points corresponding to the inner and outer core and rims are shown plotted separately. The carbonate compositions associated with these three zones can be seen to form three separate, but partially overlapping, density ellipses. In the rim zone, the major axes of the density ellipse lies perpendicular to the Ca-end member calcite ( $\text{CaCO}_3$ ), encompassing a range of Ca-poor carbonate compositions with varying Fe:Mg ratios. Transitioning to the outer core, the density ellipse that encompasses these carbonates has a composition that, while overlapping the rim density ellipse, nevertheless has a slight positive gradient with respect to the horizontal axis defined by the Mg- and Fe(Mn)-end member carbonates, magnesite and siderite (rhodochrosite;  $\text{MnCO}_3$ ). Hence, the more Fe-rich carbonates tend to be proportionally more Ca-rich, although the total fraction of Ca still remains low. The carbonate composition of the inner core shows a density ellipse that is almost perpendicular to that of both the outer core and rim, defining a range of Ca-rich to Ca-poor carbonates that share similar Mg:Fe ratios. The lower, Ca-poor, end of the density ellipse overlaps with that of the outer core while the upper Ca-rich end extends up to carbonates with an ankeritic ( $\text{Ca,Fe}(\text{CO}_3)_2$ )/dolomitic ( $\text{Mg,Ca}(\text{CO}_3)_2$ ) composition. The different compositions of the inner and outer cores and rim are reflected in the separate data point clusters associated with each region. In the Ca-poor carbonate of the rim, the (Fe + Mn):Mg ratios are seen to vary nearly over the complete range between end-members. In the outer core, a smaller spread in (Fe + Mn):Mg ratios are observed and the carbonate tends to be proportionally more Ca-rich, although the total fraction of Ca still remains low. Finally in the Ca-rich inner core, the (Fe + Mn):Mg ratios are almost invariant relative to the mole fraction of Ca, which ranges up to almost an ankeritic-dolomitic composition. This results in an elliptical distribution of points with the major axis perpendicular to that defined by the (Fe + Mn) – Mg end members.

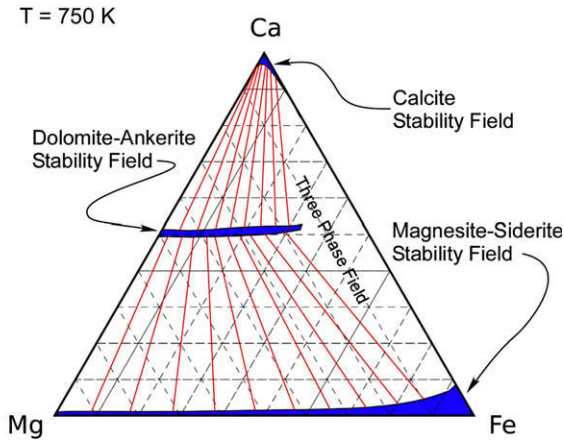


Fig. 2D. Calculated thermodynamic stability phase diagram for Fe-Mg-Ca carbonates at 750 K and 1 bar pressure, using the approach of McSwiggen (1993a) and McSwiggen (1993b). Not all carbonate compositions are thermodynamically stable resulting in three distinct stability fields, highlighted in blue, corresponding to calcite, dolomite-ankerite, and the magnesite-siderite solid solution series. While the compositional range of ALH84001 carbonate disks extends into both the magnesite-siderite (2C; rim carbonate) and ankerite-dolomite stability fields (2C; inner core carbonate), most carbonate compositions lie between these stability fields indicating that for any given carbonate disk, taken as a whole, is in a state of thermodynamic disequilibrium. (For interpretation of the references to color in this figure legend, the reader is referred to the web version of this paper.)

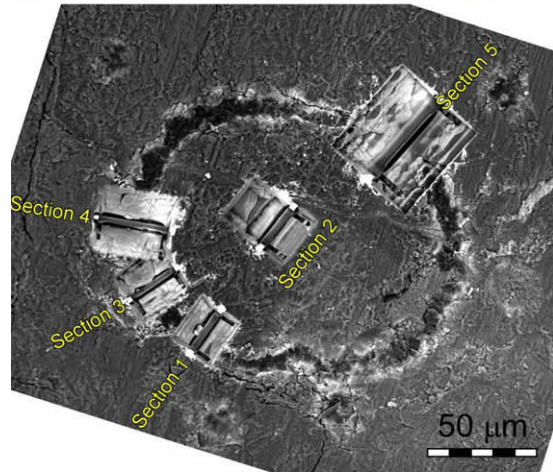
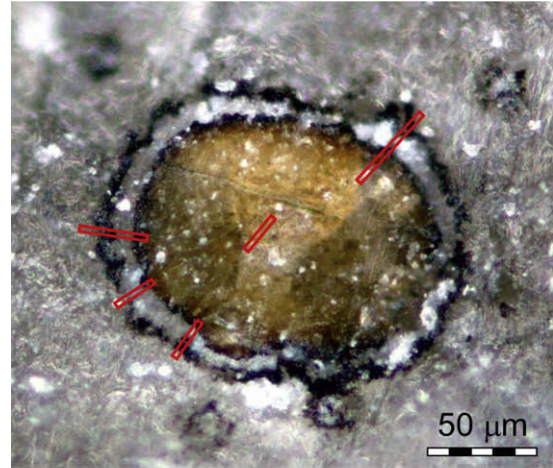


Fig. 3B. Optical (upper) and BSE (lower) views of ALH84001 carbonate disk designated as ‘PosterBoy.’ In the upper optical image the carbonate is shown prior to FIB extraction (red boxes) while the lower BSE image was acquired after five separate FIB extractions, four of the rim and one of the core. (For interpretation of the references to color in this figure legend, the reader is referred to the web version of this paper.)

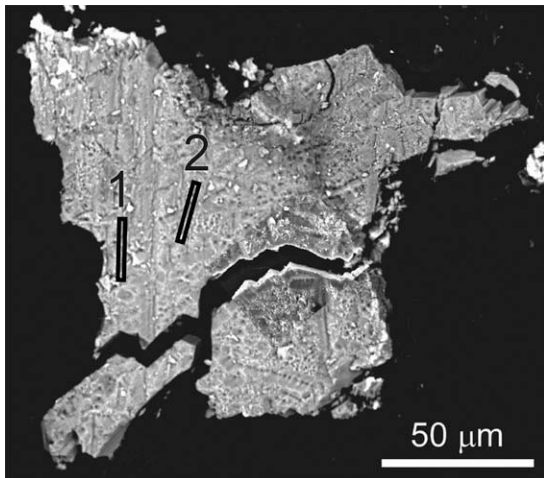


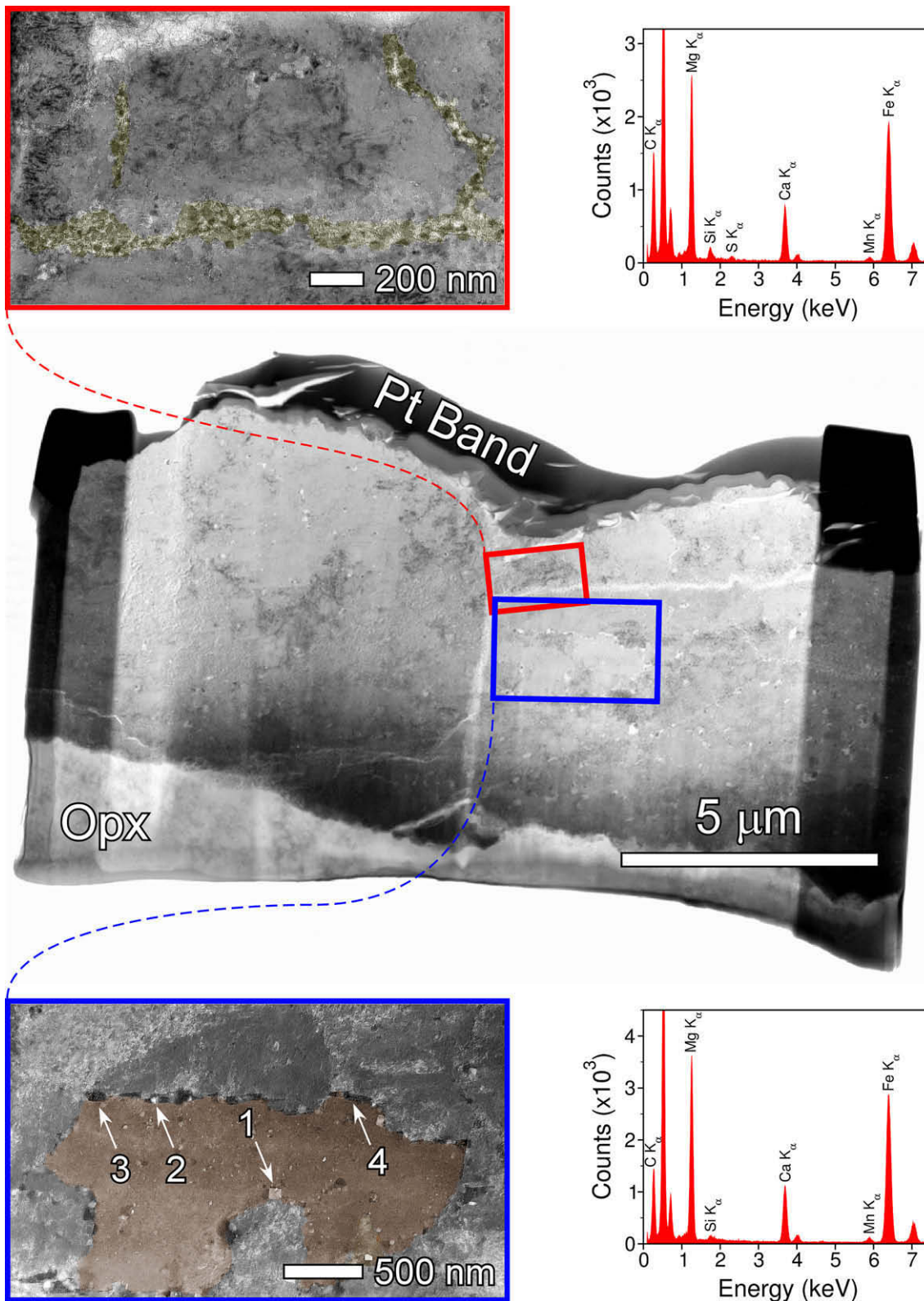
Fig. 3A. BSE view of a partial ALH84001 carbonate disk designated ‘Texas’ that was removed from the OPX fracture surface in which it was embedded and transferred to electron conductive double-sided C tape (black background). The surface shown corresponds to the exposed surface which was contiguous with the OPX. Locations of the two core carbonate FIB sections that were extracted are shown by the boxes.

et al. (2000a). Sandwiched between the inner and outer magnetite bands is the almost pure magnesite band containing minor Ca and Si (Fig. 3G) and sporadic magnetite crystals (Fig. 3G).

Morphologically the inner and outer cores and magnesite band are cross-cut by numerous veins (Figs. 3E, 3H and 3I, Figs. 5A and 5D) and open fractures (Fig. 3I), respectively, which must have formed after initial carbonate deposition. In the case of the magnesite band (Fig. 3I) most fractures appear open and are oriented along grain boundaries. A small percentage appears to be partially filled with an amorphous Fe phase(s) (Fig. 3I) that we have not yet been able to characterize. In the case of the outer core carbonate, there is extensive penetration by veins that radiate inward toward the inner core, either horizontally from the inner magnetite rim, or vertically from the upper carbonate surface (Figs. 3E, 3H and 3I, Figs. 5A and 5D). These veins are completely filled with a fine grained carbonate compositionally similar to the carbonate into which it intrudes. However, unlike the surrounding carbonate, the vein filling is intimately mixed with one or more amorphous silica phases (Figs. 5A and 5D) enriched by a factor of  $\sim 3$  with respect to the surrounding carbonate, and contains embedded stoichiometrically pure single crystal magnetites

(Fig. 5B). These magnetites range in size from  $\sim 10$  to 150 nm, and are similar to those observed in the inner and outer magnetite rims (Figs. 5A and 5C). Although magnetite-rich veins that cross-cut the outer cores are texturally identical to those of the magnetite-rich rims, one difference between them is that the veins contain few or no detectable Fe-sulfides (Figs. 5A and 5D) arguing for a different mode of formation or a different generation.

urally identical to those of the magnetite-rich rims, one difference between them is that the veins contain few or no detectable Fe-sulfides (Figs. 5A and 5D) arguing for a different mode of formation or a different generation.



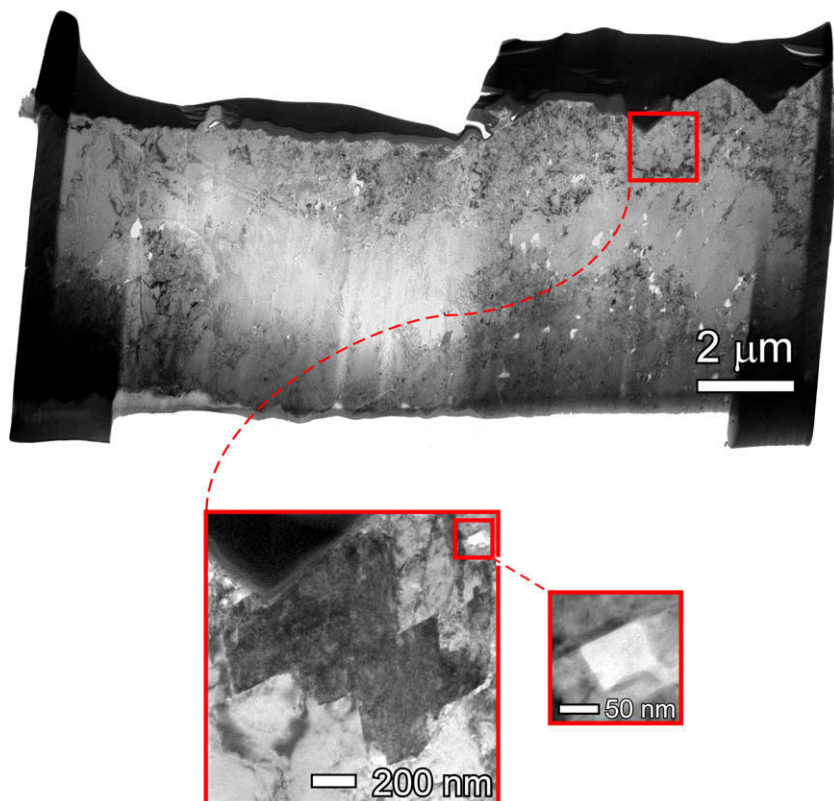


Fig. 3D. Upper view: TEM image of ‘Texas’ FIB Section 2 extracted from the disk core (see 3A). Carbonate is coarse-grained ( $\sim 1\text{--}5\ \mu\text{m}$  along the longest axis) and displays low porosity. Lower views: expanded view of ROI outlined by red box showing interlocking rhombohedral-shaped carbonate crystals visible at a tilt angle of  $+30^\circ$ . Although few magnetites are apparent, this is misleading since at this angle few of the numerous magnetites present were in a strongly diffracting orientation. A rectangular-shaped void,  $\sim 60\ \text{nm}$  in length, is present in the upper right corner of the view and is shown enlarged on the right. This feature is consistent in both size and shape to negative crystals imaged by TEM (Viti and Frezzotti, 2001). (For interpretation of the references to color in this figure legend, the reader is referred to the web version of this paper.)

### 3.2.2. ‘Posterboy’ Section 2 and ‘Texas’ Sections 1 and 2

The carbonate cores are predominantly composed of blocky interlocking, irregularly shaped carbonate crystals (Figs. 3C and 3D, 3F) ranging up to  $\sim 5\ \mu\text{m}$  in size. Inter-

spersed both within these crystals, and along grain boundaries (Fig. 3C), are sub-micron ‘void’ spaces which demonstrate a range of morphologies from amoeboidal to well faceted polygonal negative crystals (Fig. 3D). Only

Fig. 3C. Center: TEM image of ‘Texas’ FIB Section 1 extracted from the disk core (see 3A). The micron thick upper band of Pt was deposited as protection from  $\text{Ga}^+$  ion beam damage during FIB milling. The core region is composed of interlocking, mixed-cation, carbonate crystals ranging up to  $\sim 5\ \mu\text{m}$  in size cross-cut by multiple veins. This coarse-grained interior texture contrasts sharply with that of the fine-grained upper surface texture described earlier (see Fig. 1I). Two regions of interest (ROIs) are indicated by red and blue boxes. Top views: Expanded view of ROI outlined by red box showing several veins cross-cutting the host carbonate. Veins are composed of fine grained ( $< 100\ \text{nm}$ ) randomly oriented carbonate grains intimately mixed with an amorphous S-bearing phase that appears homogeneously distributed. The associated EDX spectrum was acquired using  $\sim 100\ \text{nm}$  spot size and 1000 s dwell time. We suggest the veins formed by dissolution of core carbonate during exposure to a S-containing (possibly acidic) fluid. Lower views: expanded view of ROI outlined by blue box showing numerous nanophase magnetite and voids which appear to comprise  $< 1\ \text{vol.}\%$  of the total FIB section in this TEM view (During full TEM rotation ( $\pm 44^\circ$ ) a significant increase of magnetite crystals (up to  $\sim 5\ \text{vol.}\%$ ) is observed in this FIB section. This is due to image contrast obtained by the interaction of the electron beam with the sample. In a TEM image of an ALH84001 FIB section, denser areas appear darker due to scattering of the electrons in the sample. In addition, scattering from crystal planes introduces diffraction contrast. This contrast depends on the orientation of the magnetite crystal with respect to the direction of the incoming electron beam. Thus, tilting a crystal will cause the gray-level of that crystal to change. As a result, in a TEM image of a sample consisting of randomly oriented crystals, each one will have its own gray-level at a given orientation. In this way discrete magnetites can be distinguished from each other and their carbonate matrix at different tilt angles). Magnetites (e.g., arrows 1–2) and void spaces (e.g., arrows 3–4) are located at the margin of the false colored carbonate crystal. The concentration of magnetites and void spaces at grain boundaries may due to the migration of impurities which occurred during minor carbonate recrystallization. EDX spectrum of false color carbonate shows major Mg, Ca, and Fe with minor Si and Mn. The analysis spot size and acquisition time are  $\sim 100\ \text{nm}$  and 1000 s, respectively. (For interpretation of the references to color in this figure legend, the reader is referred to the web version of this paper.)

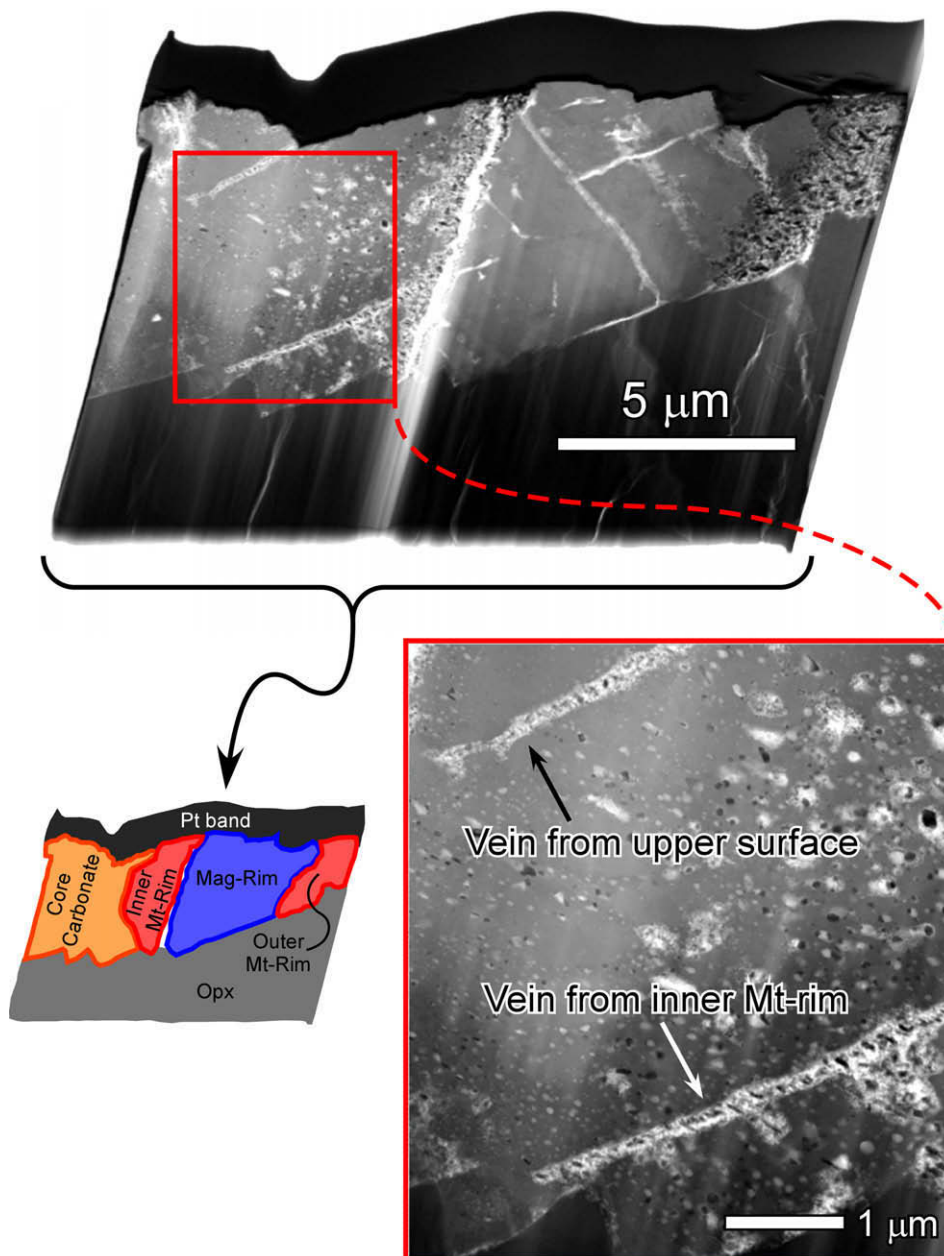


Fig. 3E. Upper: TEM view of 'Poster Boy' FIB Section 1. This section was extracted from the rim zone (see Fig. 3B) and contains both inner and outer magnetite-rich rims separated by a magnesite band (as indicated in schematic inset). The underlying OPX displays saw-tooth projections, also known as microdenticular features, previously noted to be consistent with silicate dissolution (see Figs. 1F and 1G). ROI highlighted by the red box shows two subparallel, finger-like projections or veins, ranging from  $\sim 2$  to  $5 \mu\text{m}$  in length and  $\sim 300 \text{ nm}$  in width, which extend into the outer core carbonate. The top magnetite-rich vein originates from the uppermost surface (i.e., carbonate/Pt band interface) of the carbonate disk while the bottom vein originates from the inner magnetite-rich rim. Veins are texturally identical to the inner and outer magnetite-rich rims being composed of abundant nanophase magnetite embedded in a fine-grained carbonate matrix. Both rims and veins are enriched in Si, present as an amorphous phase (see Figs. 5A and 5D), compared to the surrounding carbonate matrix. However the veins are different from the rims in that they contain far fewer Fe-sulfides (see Fig. 5A). Although the general perception of the magnetite-rich rims is of simple well demarcated bands that are vertically contiguous, this is an over simplification as evidenced by the observation of these magnetite-rich veins. Magnetite abundances in veins mimics that of the rims ( $\sim 50$ – $70 \text{ vol.}\%$ ), while those in the carbonate cores and magnesite bands are much lower.

a small amount of the observed pore space ( $<10\%$  of surface area in the imaged sections) is associated with those grain boundaries (Fig. 3C) along which are also located

single stoichiometrically pure  $\text{Fe}_3\text{O}_4$  crystals (Fig. 5B). By analogy with terrestrial carbonates, it is unlikely that this texture is primordial, but rather is the result of

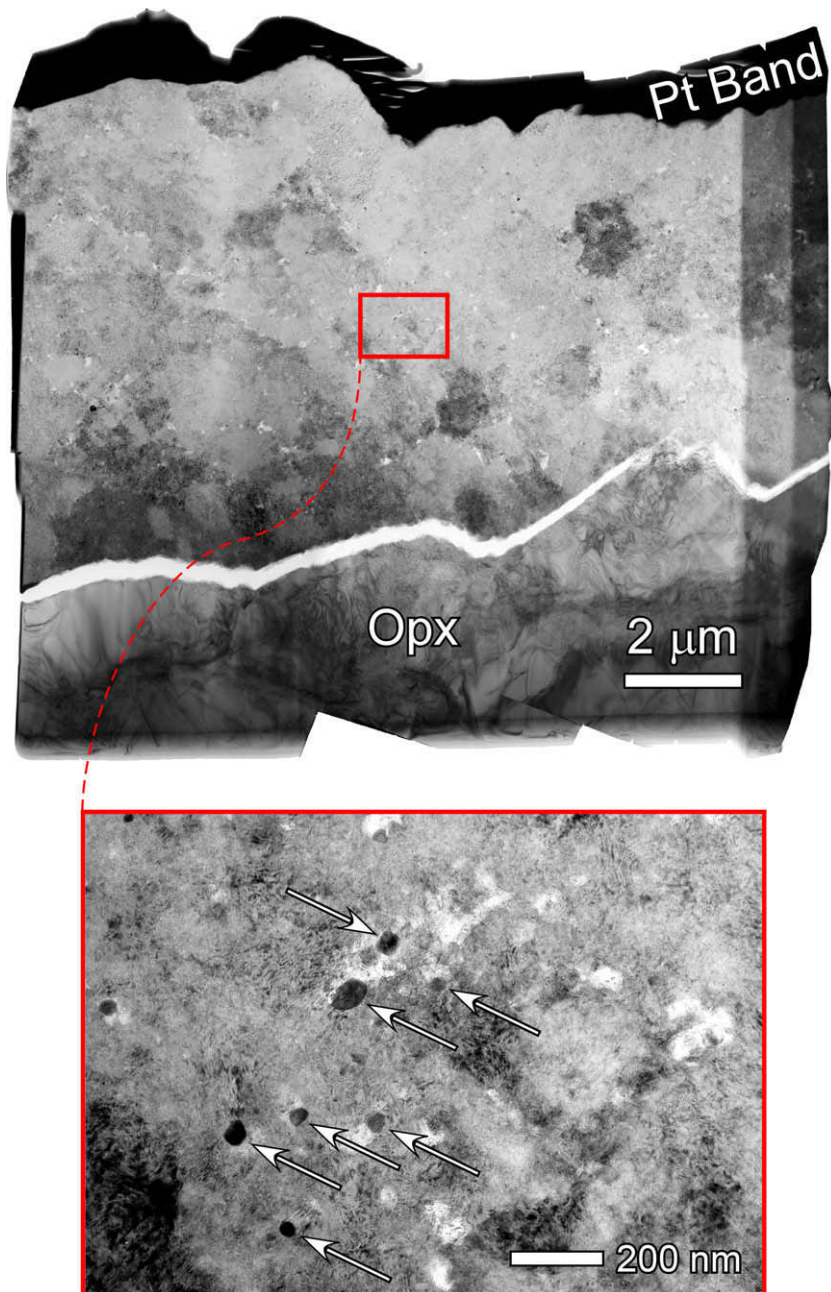
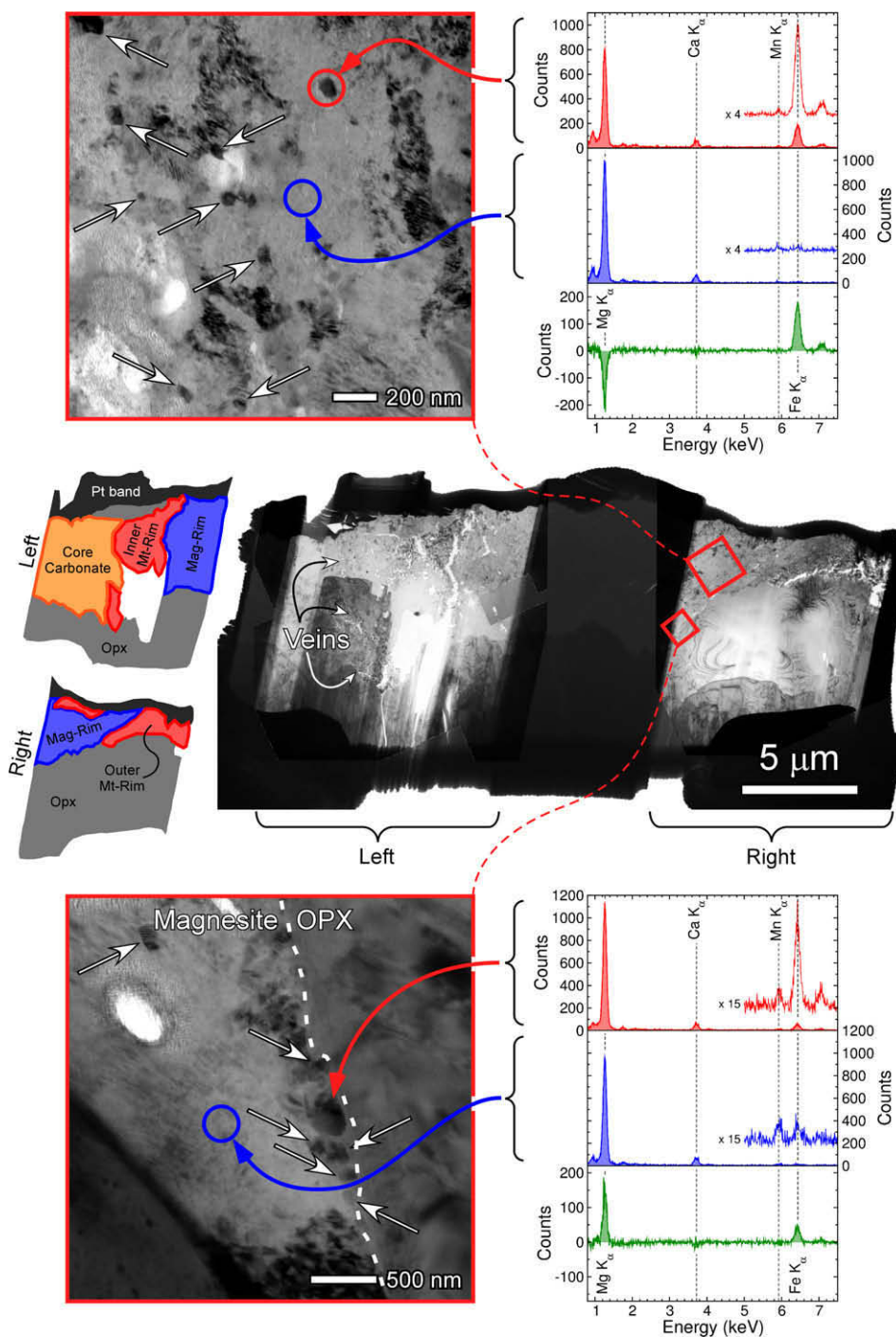


Fig. 3F. Upper: TEM view of 'Poster Boy' FIB Section 2 (also see 3B). Lower: expanded view of ROI outlined by red box showing discrete nanophase magnetites, some which appear to be associated with voids while others appear to be encased in carbonate. Core carbonate typically displays low porosity (<1 vol.%). (For interpretation of the references to color in this figure legend, the reader is referred to the web version of this paper.)

aggrading neomorphism (Folk, 1965), in which diagenetic carbonate recrystallization has resulted in an increase in crystal size without a concomitant change in the overall chemistry since fine scale cation zoning is still preserved. During recrystallization, crystallographic imperfections such as void spaces would migrate out to grain boundaries, consistent with our observation that the majority of void spaces are located at grain margins (e.g., Fig. 3C). At the carbonate disk surface the interlocking blocky texture is replaced by a fine-grain matrix as seen in Fig. II described

previously. In a small number of cases we have interpreted distinctive polygonally shaped voids to represent negative crystals (see Fig. 3D). Cutting through the core carbonate are numerous branching veins (~200 nm to several  $\mu\text{m}$  in length) that have fine grained porous texture (Fig. 3C). In contrast to the veins previously described in the outer carbonate core which contain embedded magnetite, these veins do not, being composed of fine grained carbonate intermixed with minor S, although no crystalline sulfides or sulfates were observed.



### 3.3. Properties of the magnetites

#### 3.3.1. Relationship and distribution to the host carbonate

While, as previously noted, the vast majority of magnetites within the carbonate disks reside within the inner and outer rims (Figs. 3E, 3H and 3I), it is important to note magnetites are also distributed, albeit at a low concentrations, throughout the entire inner and outer core carbonate (Figs. 3C and 3D, 3F) and magnesite band (Fig. 3G).

The nanometer-sized magnetites present in the inner and outer rims are embedded in a fine grained carbonate matrix

(primarily  $(\text{Fe}_{\sim 0.5}\text{Mg}_{\sim 0.5})\text{CO}_3$ ) containing minor Fe-sulfides and a poorly characterized amorphous silica phase as described previously. The volume percentages of the three phases are approximately 60 vol.% magnetite, 35 vol.% carbonate and 5 vol.% silica and sulfides. In contrast, those in the core occur either as discrete crystals orientated along carbonate grain boundaries or clustered within veins, accounting for  $\sim 10$ –25 vol.% of the core. The lowest magnetite abundances are found within the magnesite bands where they occur as isolated crystals accounting for  $< 1$  vol.% of the magnesite band (Fig. 3G).

Fig. 3G. Center: TEM view of 'Poster Boy' FIB Section 4 showing complete rim structure (as illustrated in schematic inset; also see 3B). Outer core carbonate contains an extensive network of magnetite-rich veins, some which lie at the carbonate-OPX interface (e.g., base of the carbonate disk). Magnetite veins are texturally identical to the magnetite-rich rims and contain ~50–70 vol.% magnetite embedded in a fine-grained carbonate matrix. The hole in the center of the section was produced by ion beam milling. In order to preserve the integrity of this FIB section, a region of the magnesite band (center of section) was not thinned to electron transparency (~100 nm thick). This section is unusual in that, in addition to the archetypal carbonate rim structure with inner and outer magnetite bands separated by a magnesite band, it contains a third partial magnetite-rich rim that overlies the upper center of the magnesite band but does not extend down to the underlying OPX (see right schematic inset). Magnetite-rich veins cut across the outer core carbonate, extending from the upper carbonate surface to the carbonate-OPX interface. OPX is also present partially overlying part of the upper surface of the outer core (see carbonate schematic on left). Two ROIs in the magnesite band are indicated by red boxes. Upper: the ROI shown in the upper box demonstrates the presence of magnetite grains (arrows) embedded within the magnesite band, which are not obviously associated with a magnetite rich vein. The composition of one of these magnetites (red circle and arrow) and the surrounding magnesite matrix (blue circle and arrow) is shown in the EDX spectra to the right along with the resulting difference spectrum (green). Both spectra were obtained using identical spot sizes and dwell times (300 s). These EDX spectra demonstrate that the magnesite host matrix is essentially Fe-free while the embedded magnetite is conversely Mg-free. In such a case it is impossible, either thermodynamically and/or kinetically, for this magnetite to have arisen from partial thermal decomposition of the surrounding matrix. Lower: The ROI shown in the lower red box demonstrates the presence of magnetites (arrows) at the base of the magnesite band and lying parallel to the magnesite-OPX interface, which are also not obviously related to the presence of a magnetite-rich vein. As with the upper ROI, EDX spectra of one of these magnetites (red) and the surrounding magnesite (blue) in which it is embedded are shown to the right along with the difference spectrum (green). Both magnetite and magnesite spectra were obtained under the same analytical conditions. Again, the magnesite is Fe-free while the magnetite is conversely essentially Mg-free, the small Mg peak in the difference spectrum being due to magnesite either under or overlying the magnetite grain, since its size is comparable to that of the section thickness. The same argument developed for the upper ROI is also applicable, namely such a magnetite cannot have originated from partial thermal decomposition of the surround magnesite. As an illustration, the EDX analysis beam spot was refocused onto the upper left section of the ROI and the beam density increased to above the damage threshold of the magnesite to begin thermal decomposition. This resulted in the formation of an elliptical hole, but did not in the formation of any detectable magnetite. (For interpretation of the references to color in this figure legend, the reader is referred to the web version of this paper.)

In TEM thin sections while some magnetites appear completely encapsulated in carbonate, others are associated with void space. The latter observation has been interpreted as evidence for their formation by thermal decomposition of the host carbonate (Barber and Scott, 2002; Brearley, 2003), since the decarboxylation of siderite to magnetite results in a volume decrease of ~50.5%, due to the higher density of the product magnetite ( $\rho_{\text{magnetite}} \sim 5.21 \text{ g} \cdot \text{cm}^{-3}$ ) relative to reactant siderite ( $\rho_{\text{siderite}} \sim 3.87 \text{ g} \cdot \text{cm}^{-3}$ ). However, in many cases the void space volume observed is far greater than that which could be accounted for density differences. An alternative explanation is that during carbonate recrystallization grain boundary migration allowed for initially unrelated impurities including void space and magnetites to relocate along grain boundaries, as is observed in terrestrial carbonates (Kennedy and White, 2001; Reid and Macintyre, 1998).

There have been several reports of individual ALH84001 magnetites having either an epitaxial or topotactic relationship to their host carbonate (Barber and Scott, 2002; Bradley et al., 1996; Brearley, 2003). Although this has again been interpreted as evidence for the partial thermal decomposition of the carbonate matrix we note that such relationships also result as a consequence of low temperature carbonate recrystallization. Numerous observations at low temperature of epitaxial/topotactic overgrowths include quartz on microfibrillar opal-CT ( $\text{SiO}_2 \cdot n\text{H}_2\text{O}$ ) (Cady et al., 1996) in marine environments, in vivo formation of calcium oxalate ( $\text{CaC}_2\text{O}_4$ ) on calcite (Geider et al., 1996), and growth of aragonite ( $\text{CaCO}_3$ ) and calcite on strontium carbonate ( $\text{SrCO}_3$ ) from solution (McCauley and Roy, 1974).

### 3.3.2. Stoichiometrical 'Pure' ALH84001 magnetite

In previous studies, we characterized magnetites isolated from entire carbonate disks by chemical dissolution of the

carbonate phase using 3M ethanoic acid ( $\text{CH}_3\text{CO}_2\text{H}$ ). Compositional analyses by EDX showed that the vast majority of these magnetites (>95%) were stoichiometrically pure  $\text{Fe}_3\text{O}_4$  within detection limits<sup>7</sup> (Thomas-Keptra et al., 2000a). While this approach yields an abundant population of magnetites for analysis, all information on their distribution within the host carbonate was lost. In order to preserve this information in this study we performed in situ EDX analyses of individual magnetites present in the 'Posterboy' and 'Texas' thin sections. Our results indicate that these magnetites share a similar physical size and morphology to those previously characterized and also appear to be stoichiometrically pure  $\text{Fe}_3\text{O}_4$ . In cases where minor amounts of Mg, Si, and Ca were also observed they were at, or below, levels that could be fully accounted for by spurious X-ray fluorescence<sup>8</sup> from the surrounding carbonate.

<sup>7</sup> Based on thin film and doped glass standards the minimum level of detection (i.e.,  $>3\delta$  background) for Mg and Mn in 100 nm magnetite crystals, with an integration time of 1500 s, is on the order of 0.05 wt.% for Mg and 0.02 wt.% for Mn.

<sup>8</sup> This can occur through either primary or secondary X-ray fluorescence of surrounding carbonate. In the former case, this arises through fluorescence of carbonate that either over or underlies magnetite in the section or through the scattering of the incident electron beam by the magnetite crystal into the surrounding carbonate. In the latter case, Fe  $K_\alpha$  X-rays from the magnetite can excite secondary X-ray fluorescence from the surrounding carbonate. Therefore the presence of trace to minor amounts of Mg, Si, and Ca should not be construed to indicate their necessary inclusion as impurities within magnetite, a supposition that is supported by the observation of either the greatly attenuated or the complete absence of Mg, Si, and/or Ca in the subset of magnetites that serendipitously bordered or project into void space.

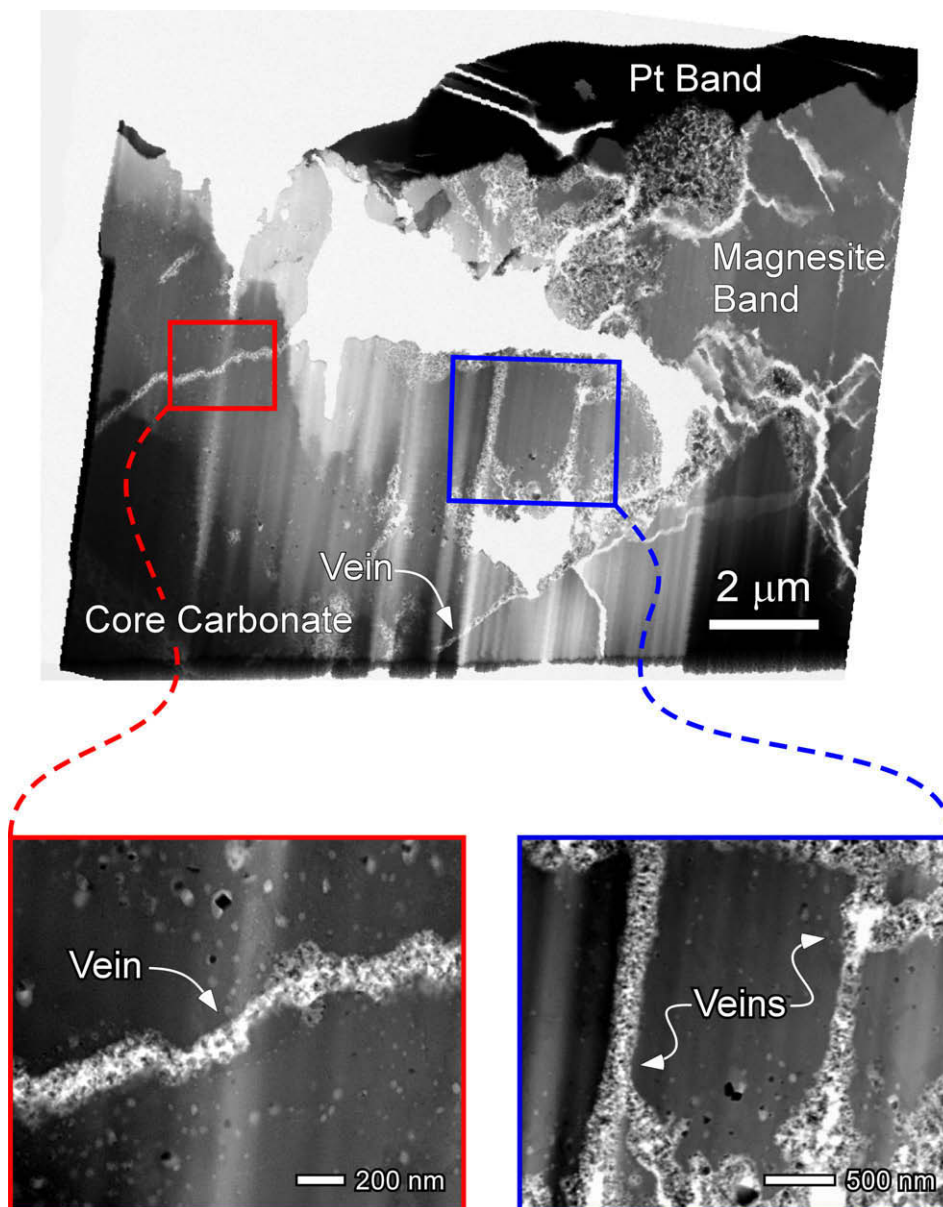


Fig. 3H. Upper: TEM view of 'Poster Boy' FIB Section 3 (see Fig. 3B). Magnetite-rich veins extend from the inner magnetite-rich rim into core carbonate. A magnetite-rich vein lies along the interface of the carbonate disk and the underlying OPX. Lower: expanded view of ROIs outlined by the red and blue boxes showing magnetite-rich veins ranging from  $\sim 2$  to  $4 \mu\text{m}$  in length and  $\sim 250 \text{ nm}$  in width, which extend into the outer core carbonate. Veins are texturally identical to the inner and outer magnetite-rich rims being composed of abundant nanophase magnetite embedded in a fine-grained carbonate matrix. Both rims and veins are enriched in Si, present as an amorphous phase (see Figs. 5A and 5D), compared to the surrounding carbonate matrix. However the veins are different from the rims in that they contain far fewer Fe-sulfides (see Figs. 5A and 5D). (For interpretation of the references to color in this figure legend, the reader is referred to the web version of this paper.)

### 3.3.3. Impure ALH84001 magnetite

Although the vast majority of the magnetites observed in situ in the 'Posterboy' and 'Texas' thin sections were chemically pure, there were several notable exceptions. In several cases, Cr at trace to minor levels was observed in a particular magnetite crystal, but absent in the surrounding carbonate (Fig. 5C). This is similar to our previous observation of Al and Cr in some magnetites liberated by acid dissolution of ALH84001 carbonate (Thomas-Keprta et al., 2000a). In that instance, Treiman (2003) argued that

the Al and/or Cr may have been present as an unobserved Fe-bearing phyllosilicate surface coating. In the present study although we attempted to identify such a magnetite surface phase we were unable to find any evidence to support it on any of the magnetites analyzed in situ within the carbonate.

While both Al and Cr are known to be readily incorporated into the inverse  $Fd3m$  magnetite spinel structure (Karl and Deborah, 2004; Razjigaeva and Naumova, 1992; Thomas-Keprta et al., 2000a), neither has ever been docu-

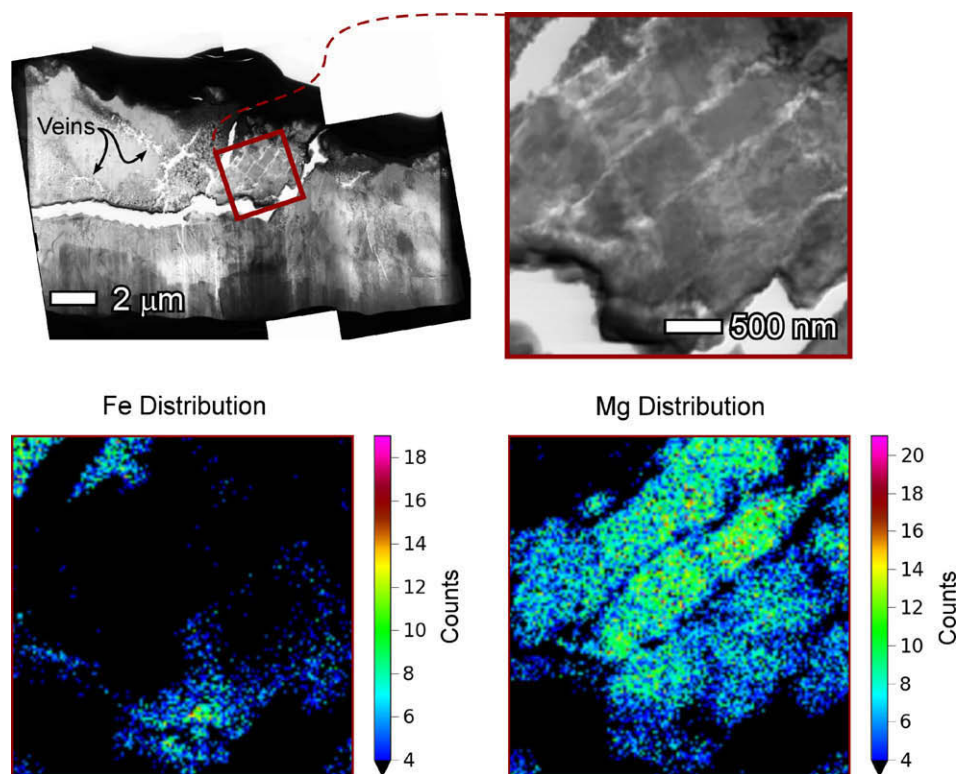


Fig. 3I. Upper: TEM view of 'Poster Boy' FIB Section 5 (see Fig. 3B). Magnetite-rich veins extend from the inner magnetite-rich rim into core carbonate. ROI highlights a region of the magnesite band. *Note:* see Fig. 5A for quantitative element maps of another ROI of this FIB section. Lower: expanded view of the ROI outlined by the red box with corresponding quantitative Fe and Mg maps ( $K_2$  line). Vertical color bars to the right of each of the element maps represent the number of X-ray counts per pixel. The magnesite displays a blocky texture intimately associated with a minor Fe component present as a fine-grained, amorphous phase consistent with ferrihydrite. Influx of secondary (i.e., ferrous-ferric fluid(s)) after carbonate disk formation is likely responsible for the presence of this amorphous Fe phase. (For interpretation of the references to color in this figure legend, the reader is referred to the web version of this paper.)

mented to substitute into the  $R\bar{3}c$  calcite-type carbonate structure. In the absence of any speculative surface coating to explain their presence, those magnetite containing Al and/or Cr could not have formed through thermal decomposition of the surrounding carbonate. To suggest otherwise would require the presence of either a non-existent Al/Cr substituted precursor siderite, or the coexistence of an unknown and indeterminable Al/Cr phase miscible with the precursor carbonate that underwent simultaneous decomposition.

### 3.4. Roxbury siderite

#### 3.4.1. Characterization of unheated Roxbury siderite

Unheated Roxbury siderite was observed to be composed of both coarse and fine-grain components (Fig. 6A). The coarse fraction is characterized by lath-shaped grains ranging in length from  $\geq 0.1$  to  $1 \mu\text{m}$ , although the upper size limit is likely artificially constrained due to chattering during microtome cutting. In contrast, the fine fraction is characterized by equant particles  $< 50 \text{ nm}$  in diameter ranging in geometries from angular to pseudo-spherical (Fig. 6A). Mixing between the two size fractions was highly variable and sample dependant, giving rise to regions either composed of almost entirely coarse or fine

grain carbonate, or an intimate mixture of both. While selected area electron diffraction (SAED) patterns of both coarse and fine grain fractions are consistent with bulk  $\text{FeCO}_3$  (Fig. 6A; Table 4), they are compositionally distinct with respect to the degree of cation substitution of Fe by Mg. The fine grained carbonate contains only minor amounts of Mg compared to the coarse grained carbonate which contains major amounts of Mg (Fig. 6A). In both size fractions, however, Mn and Si (in an unidentified amorphous phase) were observed uniformly as minor and trace components respectively (Fig. 6A). No evidence of any Fe-oxide phases was noted.

#### 3.4.2. 'Slow' heated Roxbury siderite

'Slow' heating of Roxbury siderite resulted in the formation of an optically black product composed of irregular-shaped discrete crystals of magnetite, ranging from  $\sim 20$  to  $500 \text{ nm}$  in the longest dimension (Fig. 6B; Table 5). Minor to trace amounts of both Mg and Mn were detected in every magnetite crystal analyzed (Fig. 6C). SAED analysis (Fig. 6B; Table 5). Composition of the 'slow' heated product phase (Fig. 6C) is consistent with a (Mg,Mn)-ferrite ( $(\text{Mg}_{1-x}\text{Mn}_x)\text{Fe}_2\text{O}_4$ ) product whose end members are magnetite ( $\text{Fe}_3\text{O}_4$ ), magnesioferrite ( $\text{MgFe}_2\text{O}_4$ ) and jacobsonite ( $\text{MnFe}_2\text{O}_4$ ) (Table 5). No

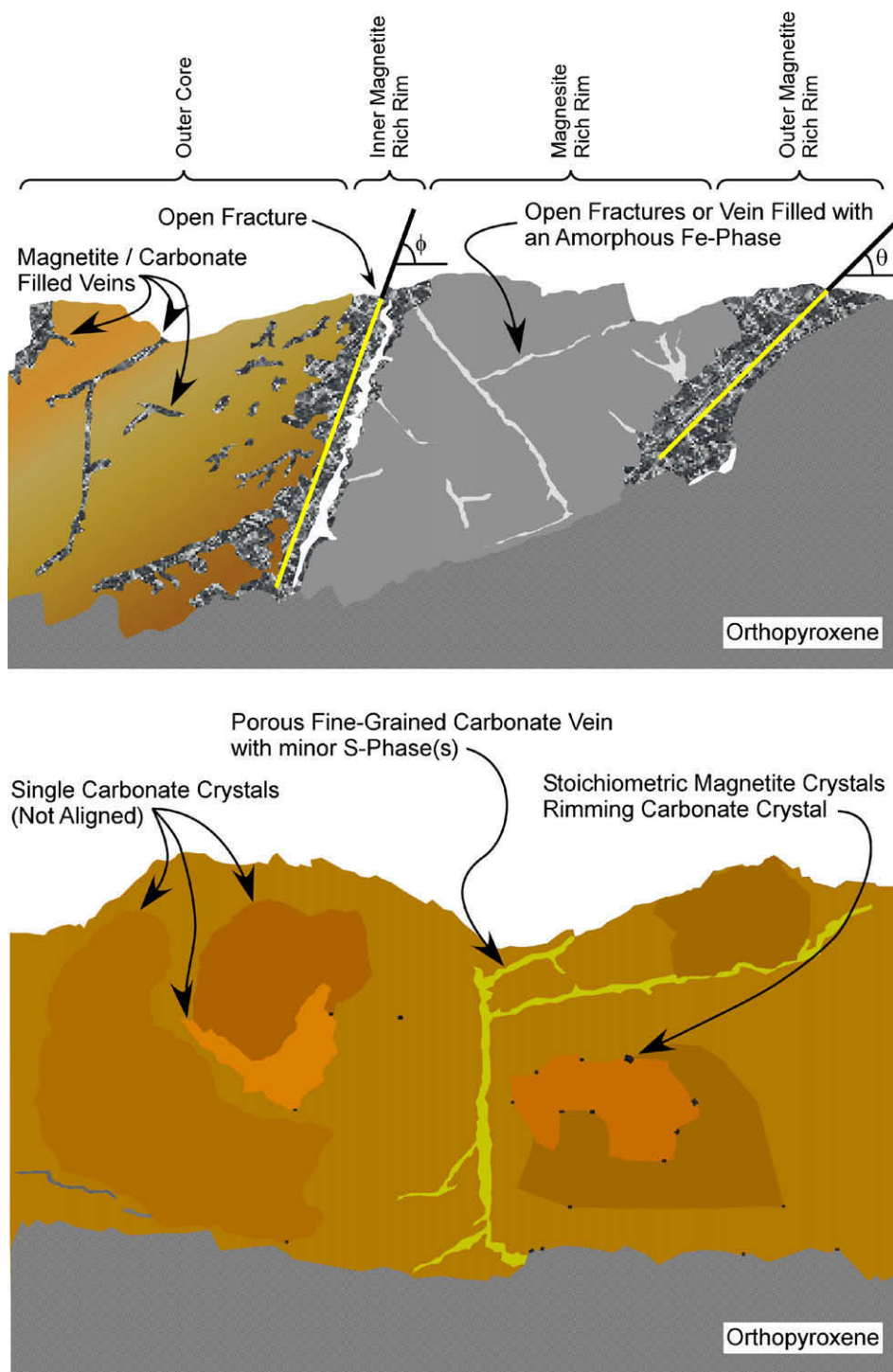


Fig. 4. Upper: schematic representation of the typical carbonate rim structure based on the four ‘Poster Boy’ FIB rim extractions (‘Poster Boy’ Sections 1; 3–5). The inner and outer magnetite-rich rims are not simple radial bands but show a complex network of veins that penetrate both the magnesite rim and the outer core carbonate. These veins are magnetite rich and appear intimately associated with fine-grained Fe-sulfides phases and minor amorphous silica phase. In addition to those magnetites associated with veins, numerous individual magnetites are also distributed throughout the magnesite rims and outer core. As with the vein magnetites these appear chemically pure, that is they are free of cations that characterize the surrounding carbonate, but they are not associated with any sulfides or silica phases (see text for a detailed discussion). Lower: schematic representation of the typical carbonate core structure based on three core FIB extractions, two from ‘Texas’ carbonate and one from ‘Poster Boy’ carbonate (Section 2). In general, the inner core carbonate is composed of multiple interlocked blocky irregularly shaped crystals that are not crystallographically aligned. Rimming the boundaries between these crystals are individual magnetite grains that can account for up to several percent of the volume of the inner core carbonate. Unlike the magnesite band and outer core no magnetite rich veins were observed in inner core sections, however numerous porous fine grained carbonate veins intimately associated with a poorly defined S-rich phase that appears either amorphous or proto-crystalline are observed. These veins run in all orientations and do not correlate with crystallographic boundaries (also see Fig. 3C).

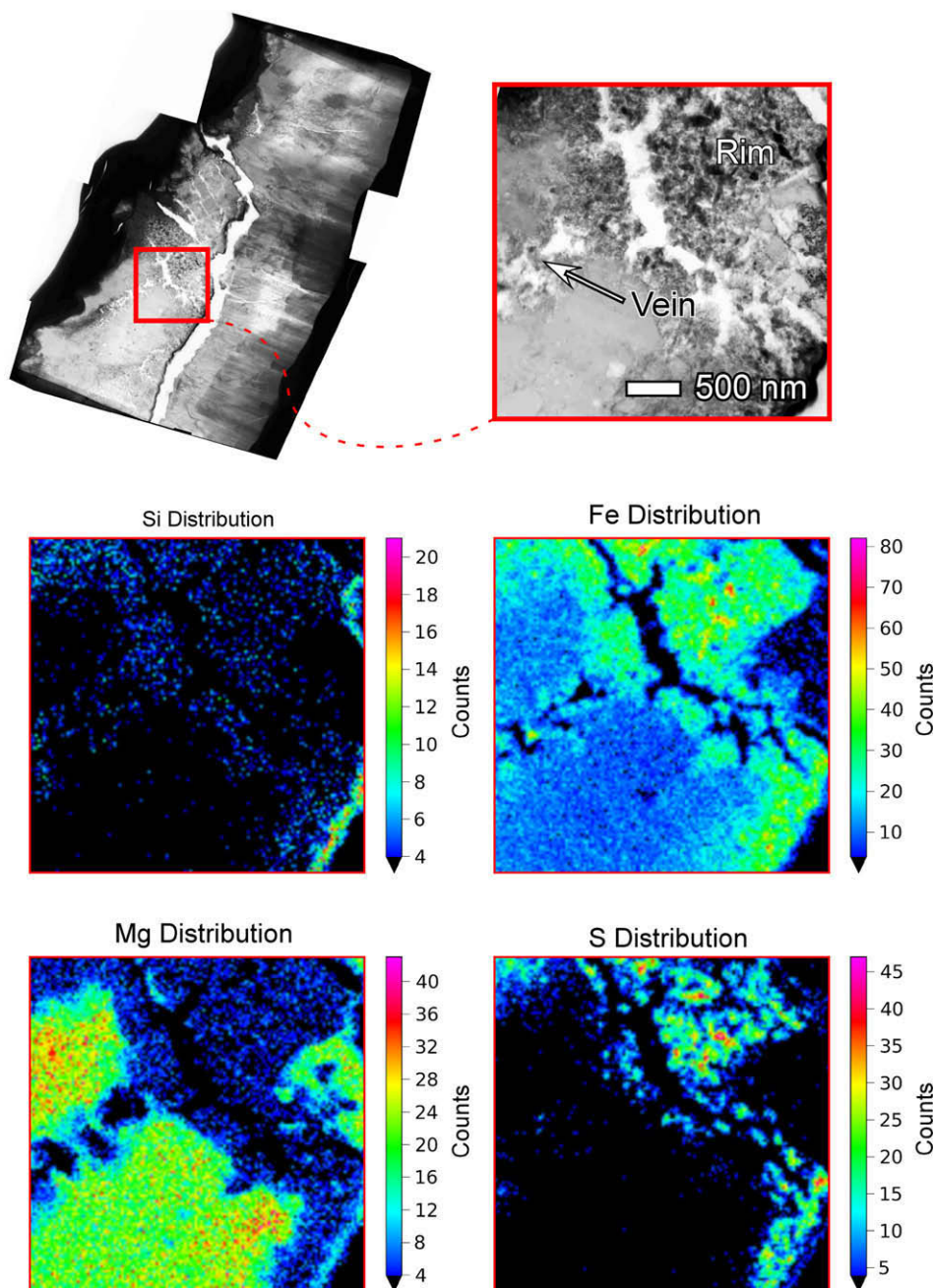


Fig. 5A. Upper left: 'Poster Boy' FIB Section 5 showing the location of a magnetite-rich vein that extends from the inner magnetite-rich rim into outer core carbonate. Expanded view of the ROI outlined by the red box on the upper right shows the intersection of the magnetite-rich vein with the inner magnetite-rich rim. Lower views: quantitative Si, Fe, Mg, and S maps ( $K_{\alpha}$  line) of the ROI above. Vertical color bars to the right of each of the element maps represent the number of X-ray counts per pixel. The core carbonate in the lower left quadrant of the ROI, contains an approximately equimolar (Fe,Mg)-carbonate with an intimately associated minor Si component that is present either as an amorphous (glass, gel, colloid) or opaline phase. The magnetite-rich rim, upper right quadrant of the ROI, and magnetite-rich vein that penetrates the outer core carbonate also show a minor Si component but this is enriched by a factor of  $\sim 3 \times$  relative to outer core carbonate. Additionally the rim shows a significant S enrichment due to the presence of nanophase Fe-sulfides, which contrast sharply with both the vein and outer core carbonate. We suggest that the presence of an amorphous Si phase in the magnetite-rich rim and vein suggests that the carbonate disk was penetrated, post formation, by a Si-rich fluid. Furthermore, since both the magnetite-rich rim and vein are texturally indistinguishable, the paucity of Fe-sulfides within the vein implies different origins for these two populations.

evidence was observed for residual carbonate indicating the decomposition reaction had proceeded to completion, nor was there any evidence for non-ferrous oxides such as periclase (MgO).

#### 3.4.3. 'Fast' heated Roxbury siderite

'Fast' laser heating of Roxbury siderite under vacuum resulted in a pronounced optical darkening of the original iridescent siderite surface (Fig. 6D). Microtome

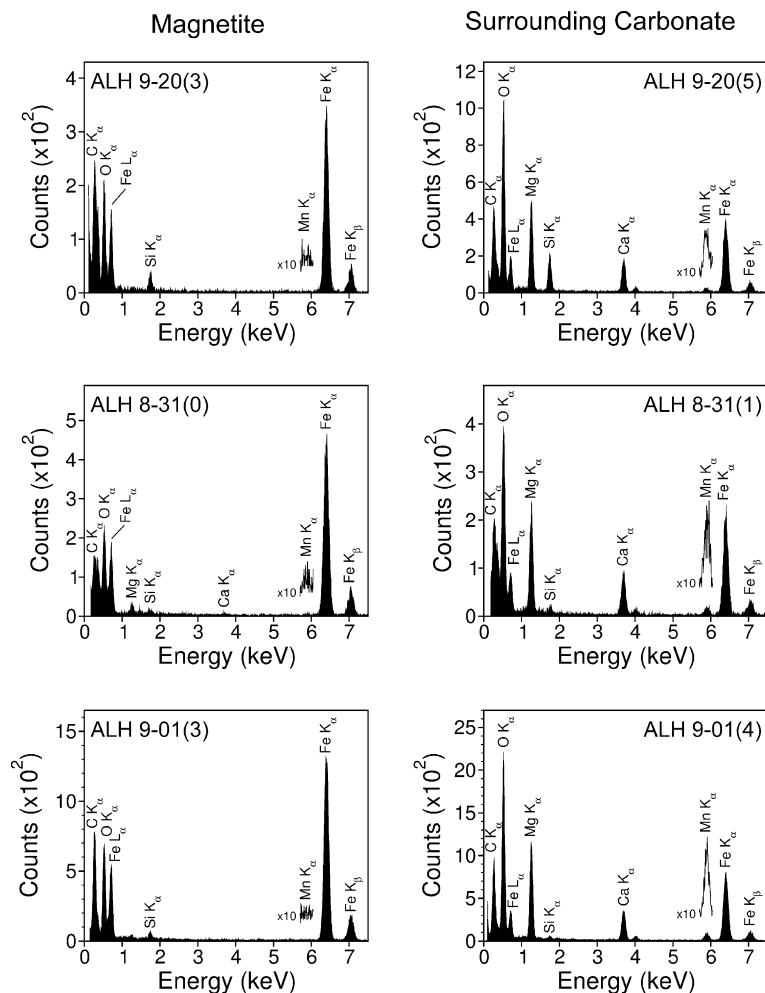


Fig. 5B. Paired EDX spectra taken in situ with a 50 nm beam spot size from ‘Poster Boy’ FIB sections illustrating the compositional inhomogeneity between individual magnetite grains and the respective host carbonate matrix in which they are embedded. Spectra on the left are of the individual magnetite grains while those on the right are taken from the carbonate matrix immediately (<100 nm) adjacent to the given magnetite. Both ALH 9-20 and ALH 9-01 paired spectra were acquired with a 1500 s dwell time, while the ALH 8-31 paired spectra were acquired with a 3000 s dwell time owing to a reduced count rate. In all three cases, major Mg and Mn present in the carbonate host matrix are, within experimental error, absent from the respective magnetite. In the case of ALH 8-31(0) spectra although trace amounts (<0.1 wt.%) of Mg are apparent in the magnetite spectrum, this most likely arises from spurious primary and secondary X-ray fluorescence of carbonate due to the thickness of the FIB sections that could be over- or underlying the magnetite grain.

cross-sections through the altered surface indicated that the laser induced heating penetrated down to a depth of  $\sim 1.0\text{--}1.5\ \mu\text{m}$  (see Fig. 6E). Based on textural differences, the ‘fast’ heated Roxbury siderite can be subdivided into three regions (Fig. 6E). Beginning at the surface and extending down to a depth of  $\sim 400\ \text{nm}$  (Region 1) the carbonate decomposition has gone to completion to produce closely packed assemblage of Fe-oxides ranging from  $\sim 20$  to  $100\ \text{nm}$  in size (Figs. 6E and 6F). In some cases, the temperature excursion created by the laser was sufficient to allowed surface-energy minimization of this Fe-oxide phase resulting in pseudo-spherical morphologies. As with the ‘slow’ heated siderite these Fe-oxides contain variable amounts of Mg but a uniform amount of Mn (Fig. 6F), and SAED patterns implies the formation of both well and poorly crystallized (Mg,Mn)-ferrites (Figs. 6E and 6F; Region 1, Table 5) as defined above. Below this is a

second region (Region 2) that extends downward a further  $\sim 800\ \text{nm}$  in which the carbonate appears to have undergone extensive vesiculation but has not otherwise decomposed as indicated by the absence of Fe-oxides (Fig. 6G; Region 2, Table 4). Finally, below this the carbonate appears indistinguishable from the unheated starting material (Figs. 6A, 6E, Region 3, Table 4).

#### 4. DISCUSSION

Partial thermal decomposition of sideritic carbonate has been proposed as the origin of the nanocrystalline magnetite present within and throughout ALH84001 carbonate disks (Brearley, 2003; Treiman, 2003). This reaction is most commonly formulated as:



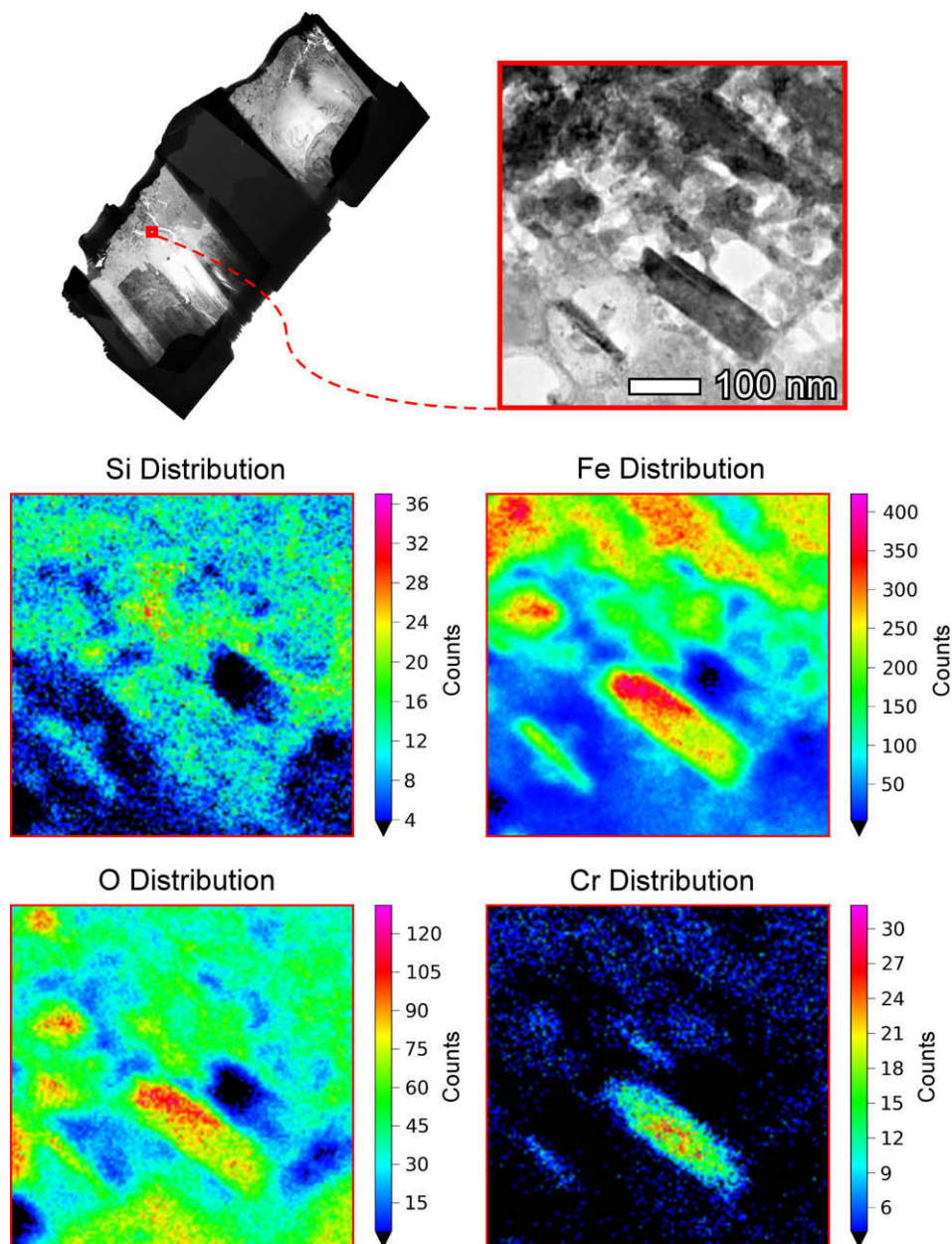


Fig. 5C. Upper left: ‘Poster Boy’ FIB Section 4 showing the location of a Cr-bearing magnetite. Expanded view of the ROI outlined by the red box (upper right) shows the Cr-bearing magnetite embedded in the inner magnetite-rich rim. Lower views: quantitative elements maps ( $K_{\alpha}$  line) for Si, Fe, Cr, and O of the ROI. The rectangular-shaped Cr-bearing magnetite crystal is  $\sim 200$  nm in length embedded in the inner magnetite-rich rim enriched in Si. No Cr-bearing phases (i.e., phyllosilicates or iron-oxides/hydroxides) surrounded or coated this magnetite. The presence of Cr-bearing magnetite has important implications for thermal decomposition models proposed for the formation of ALH84001 magnetite since this magnetite cannot be the product of thermal decomposition of Cr-free carbonate. We suggest this magnetite is an allochthonous (i.e., detrital) component which became embedded in carbonate during or subsequent to disk formation. ALH84001 magnetites extracted from the carbonate matrix with similar compositions were described previously by Thomas-Keprta et al. (2000a). (For interpretation of the references to color in this figure legend, the reader is referred to the web version of this paper.)

Would such a process be feasible given the physical and chemical properties of ALH84001 carbonate? Since such a reaction could not have occurred in isolation, we also need to address whether putative thermal decomposition is consistent with the experimental observations of ALH84001 carbonates. Our approach to these issues was to first consider the nature and timing of the heating events that

ALH84001 is known to have experienced after carbonate formation and which could have facilitated carbonate decomposition. We argue this provides a natural and convenient way to categorize the various thermal decomposition hypothesis into two groups – those that are subject to kinetic control as exemplified by the model of Brearley (2003) or those that are subject to thermodynamic control

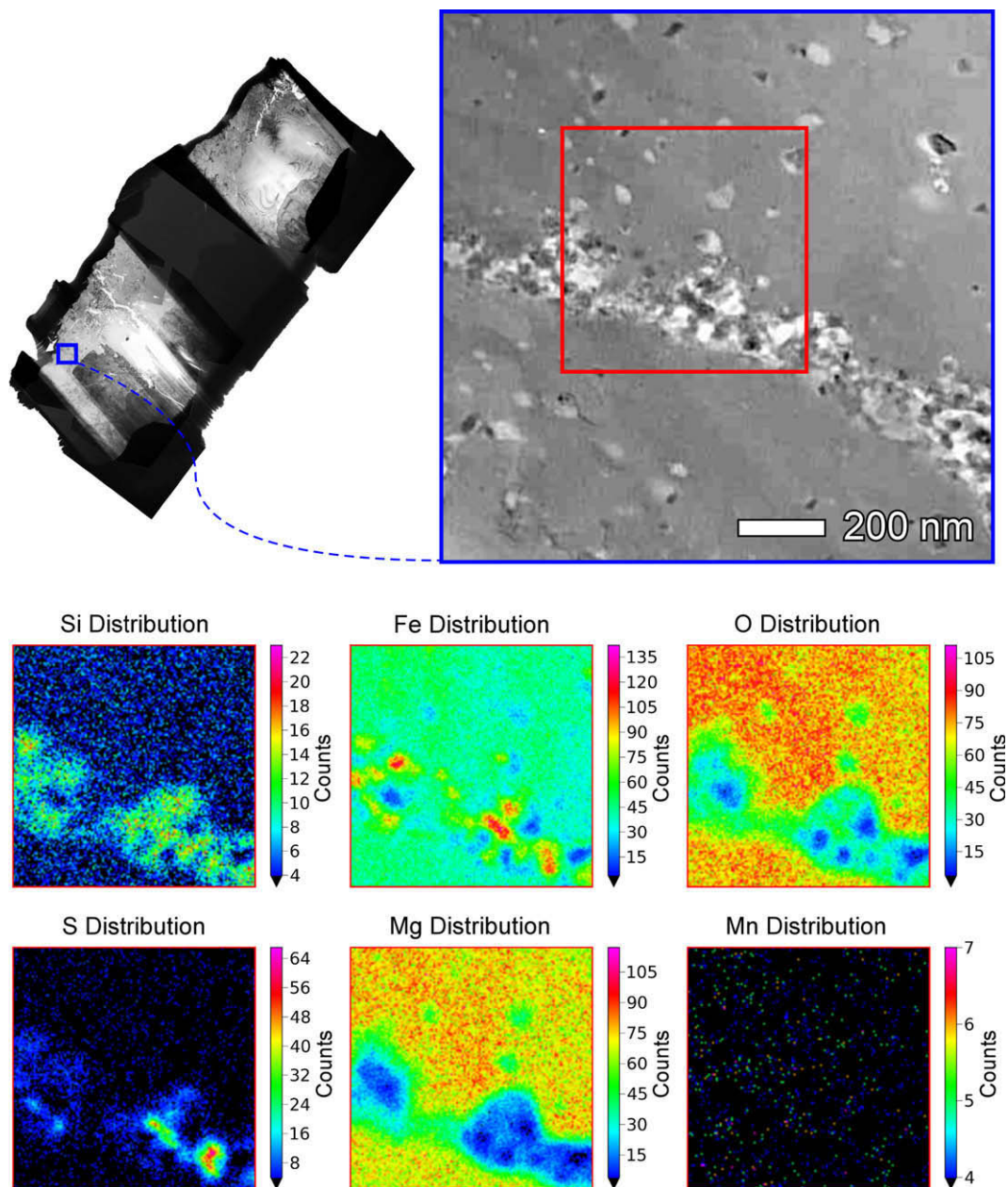


Fig. 5D. Upper left: ‘Poster Boy’ FIB Section 5. Expanded view of the ROI outlined by the blue box shows a magnetite-rich vein cross-cutting outer core carbonate. This vein is not associated with the magnetite-rich rim; it begins at the interface of outer core carbonate and an isolated patch of OPX adhering to the uppermost carbonate surface. Lower views: elements maps ( $K_{\alpha}$ -line) for Si, Fe, O, S, Mg, and Mn of the ROI shown in the red box (upper right). The vein is texturally identical to the magnetite-rich rims being composed of nanophase magnetite embedded in a fine-grained carbonate matrix, but contains few Fe-sulfides and is enriched in Si by approximately a factor of three relative to core carbonate. Note Mg is not enriched at the interface of the vein/host carbonate indicating a lack of evidence for cation diffusion (see Section 4). (For interpretation of the references to color in this figure legend, the reader is referred to the web version of this paper.)

as exemplified by the model of Treiman (2003). We consider both the Brearley (2003) and Treiman (2003) hypotheses first on their intrinsic merits as presented, and second in the light of new observations reported here.

#### 4.1. The ‘ALH84001 Heating Event’

If the partial thermal decomposition of sideritic carbonate is the source of magnetite in ALH4001 disk carbonates,

then the nature and distribution of the product magnetites will be a reflection of both the initial carbonate composition and the nature of the heating event from which they formed.

At this stage it is important to make some general remarks on the mechanisms by which reactions in the solid-state are affected. Thermal decomposition of siderite represents the solid-state transformation of an ionic crystal lattice from rhombohedral ( $R\bar{3}c$ ) to cubic ( $Fd\bar{3}m$ ) symmetry.

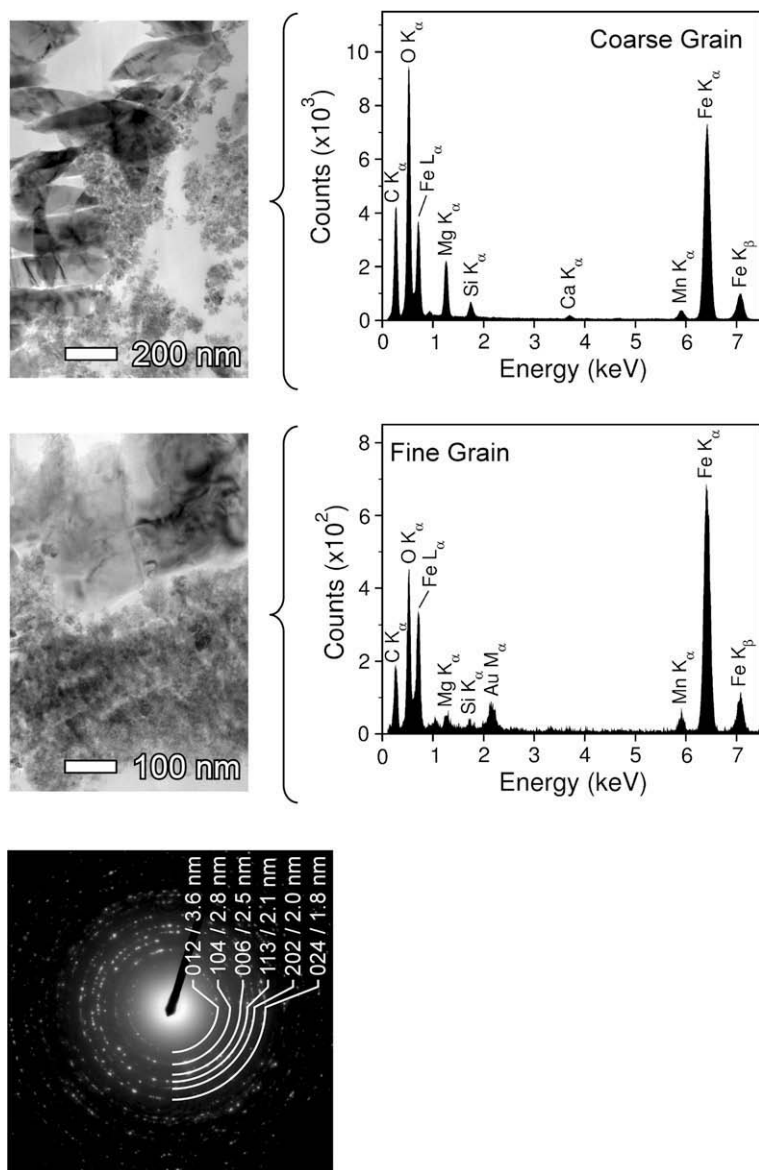


Fig. 6A. TEM images and accompanying EDX spectra of ultramicrotome sections ( $\sim 100$  nm thick) of Roxbury siderite (bulk composition  $(\text{Fe}_{0.84}\text{Mg}_{0.10}\text{Mn}_{0.04}\text{Ca}_{0.02})\text{CO}_3$  (Lane and Christensen, 1997)), composed of both coarse ( $\mu\text{m}$ ) (upper view) and fine ( $<100$  nm) grained (middle view) components. From the EDX spectra it is apparent that while Mn appears to be uniformly distributed in both fractions, Mg is enriched by a factor of  $\sim 4$  in the coarse grained fraction. Both EDX spectra contain minor Si lack  $d$ -spacings consistent with crystalline silicates, indicating the presence of an intimately mixed, homogeneous, amorphous silica component (e.g., a glass, gel, or opaline phase). Both EDX spectra were acquired with an analysis spot size of  $\sim 200$  nm and acquisition time of 1000 s. Lower view: SAED pattern of Roxbury siderite (both coarse and fine grained components). Observed  $d$ -spacings are consistent with a sideritic carbonate that is free of any Fe-oxides.

In general solid-state transformations are initiated by a bond redistribution process, in the case of carbonates this is the reversible endothermic dissociation of the carbonate anion  $\text{CO}_3^{2-} \rightleftharpoons \text{O}^{2-} + \text{CO}_2$  (de La Croix et al., 1998), followed by reorganization and remobilization of the isolated anion/cation aggregates thus formed into nascent nucleation sites. At the nucleation sites subsequent growth then occurs preferentially due to the enhanced reactivity of the reactant interface surrounding the nucleating product. This enhanced reactivity is derived in part from the lattice strain induced by differing unit cell parameters and symmetries

existing between reactant and product. Nuclei growth can be envisioned as the progressive advancement of this activated reaction interface into the surrounding reactant phase. Growth will continue until either the interface between the product and reactant is terminated and/or the thermal energy driving the decomposition is dissipated. This process of crystal nucleation and growth is a fundamental assumption in solid state transformations of ionic solids (Galwey and Brown, 1999).

One of the defining characteristics of magnetites embedded in ALH84001 carbonate is their sub-micron size

Table 4  
Carbonate *d*-spacings: unheated and ‘fast’ heated Roxbury siderite.

<i>hkl</i>	Siderite <sup>a</sup>	Magnesite <sup>a</sup>	Rhodochrosite <sup>a</sup>	Mg–Fe carbonate <sup>a</sup>	Roxbury siderite (unheated and ‘Fast’ heating-Region 3)	Roxbury siderite (‘Fast’ heating-Region 2)
	<i>d</i> -spacings (nm)	<i>d</i> -spacings (nm)	<i>d</i> -spacings (nm)	<i>d</i> -spacings (nm)	This study <i>d</i> -spacings (nm)	This study <i>d</i> -spacings (nm)
012	0.359	0.354	0.366	0.354	0.36	0.36
104	0.279	0.274	0.284	0.275	0.28	0.28
006	0.256	0.250	0.262	0.251	0.26	
110	0.235	0.231	0.239	0.232	0.24	0.23
113	0.213	0.210	0.217	0.210	0.21	0.21
202	0.196	0.194	0.200	0.194	0.20	0.20
024	0.179	0.184	0.183	–	0.18	–
108	0.173	0.177	0.177	0.173	–	0.17

<sup>a</sup> International Centre for Diffraction Data Powder Diffraction Database – PDF-2 release 1998.

distribution. If we assume that the rates of nucleation and growth can be approximated by a Arrhenius-type temperature dependence (see Electronic Annex, EA-1) this would infer that the thermal decomposition of siderite occurred at high temperature so as to facilitate rapid nucleation over crystal growth. Furthermore it is implicit that the heating rate was fast enough to prevent significant carbonate decomposition from occurring before the peak temperature was reached. Otherwise, fewer and larger decomposition products would be expected. Hence, if the magnetites in ALH84001 formed by thermal decomposition, the responsible heating event would have been characterized by a rapid thermal step to high temperature. Given these requirements, and the evidence for multiple shock events experienced by ALH84001, the most probable geological scenario for decomposition would have been during the diabatic propagation of an impact-generated shockwave, either during the impact that ejected the ALH84001 meteorite, e.g., Brearley (2003), or during an earlier pre-ejection impact while ALH84001 remained buried in the Martian regolith, e.g., Treiman (2003). In both cases the shock heating would have been characterized by a near instantaneous rise in temperature followed by a slower monotonic cooling back to ambient. The key difference between the two scenarios is the timescale over which cooling could have occurred. In the first case, cooling would have been rapid and occurred through radiative loss into the vacuum, while in the second case, cooling would have been far slower occurring instead primarily through conduction into the surrounding regolith.

#### 4.1.1. Ejection cooling

It is difficult to tightly constrain the thermal history of ALH84001 immediately following its ejection; nevertheless we can make a reasonable order-of-magnitude estimation by modeling the meteorite as an idealized black body that cools solely by radiative emission (see EA-2). Under such conditions, the time to cool from some initial temperature  $T_0$  down to temperature  $T_1$  is given approximately by the expression:

$$t_{\text{cooling}} \approx 3.11 \times 10^{11} \cdot \left[ \frac{1}{T_1^3} - \frac{1}{T_0^3} \right] \quad (2)$$

From this we estimate that the time for ALH84001 to cool to ambient ( $\sim 233$  K; see EA-2) following its ejection would have been only a matter of hours, corresponding to cooling rates of  $\sim 10^{11}$ – $10^{12}$  K · Ma<sup>-1</sup>.

#### 4.1.2. Subsurface cooling

If cooling following a shock heating event had occurred while buried in the Martian regolith then the cooling rate would be a function of both the burial depth and the process by which cooling occurs (e.g., hydrothermal cooling or thermal diffusion). The paucity of hydrous minerals in ALH84001 (Brearley, 1998) implies limited hydrothermal exposure suggesting that heat diffusion would have been the dominant cooling mechanism. In terrestrial impact structures cooling rates in the melt-rich portions are on the order of  $10^7$  K · Ma<sup>-1</sup>, while deeper within the impact structure cooling rates can be much slower, typically  $10^2$ – $10^3$  K · Ma<sup>-1</sup>. Several estimations for the cooling histories of the ALH84001 carbonate disks have been made based on cation diffusion studies. Fislser and Cygan (1998) and Kent et al. (2001) have independently determined solid state cation diffusion rates of Mg<sup>2+</sup> and Ca<sup>2+</sup> in calcite and magnesite from which they suggest a lower limit for the cooling rate of  $\sim 10^2$ – $10^3$  K · Ma<sup>-1</sup>. If the cooling rate were any slower the fine-scale chemical zoning of the carbonates could not have been preserved (Fig. 7A). Most recently, Domenghetti et al. (2007) have used the degree of fractionation of Fe<sup>2+</sup> and Mg<sup>2+</sup> between the two non-equivalent octahedral sites, *M1* and *M2*, in OPX ( $\text{Fe}_{M2}^{2+} + \text{Mg}_{M1}^{2+} \rightleftharpoons \text{Fe}_{M1}^{2+} + \text{Mg}_{M2}^{2+}$ ) to estimate the cooling rate of the last significant thermal event experienced by the OPX in ALH84001. Their results infer a closure temperature,  $T_c$ , of  $802 \pm 30$  K as a lower limit for the last impact heating event, with a corresponding cooling rate of  $\sim 0.1$  K · day<sup>-1</sup>. This suggests that if partial thermal decomposition of ALH84001 carbonates occurred as a consequence of impact heating during burial, it would have

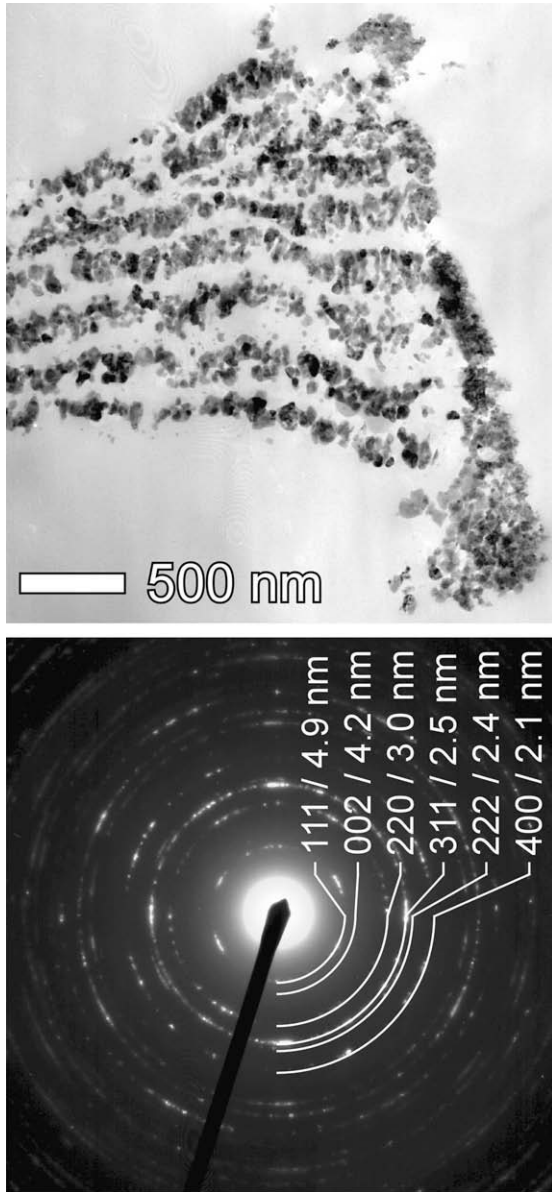


Fig. 6B. Upper: TEM view of an ultramicrotome section of Roxbury siderite after heating to 848 K using the LSQT method of Golden et al. (2006). The heating rate was  $1 \text{ K} \cdot \text{min}^{-1}$  (i.e., ‘slow’ heating) with the peak temperature being maintained for 24 h (see Methods section). The grain size ranges from  $\sim 20$  to 200 nm. Lower: SAED pattern of heated Roxbury siderite shown above. Measured  $d$ -spacings indicate the siderite has converted completely to magnetite.

had to have occurred on a timescale of only a few decades or less. In either case to prevent complete, as opposed to partial, decomposition of the carbonate globules, the heating event would have had to have occurred under higher pressure conditions than Mars atmospheric. Assuming a Mars crustal density of  $\rho_{\text{Mars}} \approx 3000 \text{ kg} \cdot \text{m}^{-3}$  (McSween, 2002), and a surface gravity of  $G_{\text{Mars}} \approx 3.72 \text{ m} \cdot \text{s}^{-2}$ , the pressure  $P$  in bars, at a depth  $d$  in meters, can be approximated as  $P \approx \frac{\rho_{\text{Mars}} \cdot G_{\text{Mars}} \cdot d}{10^5} \approx \frac{d}{9}$ . Hence a pressure of 10 bars implies a burial depth of  $\sim 9$  m, while a pressure of 100 bars

suggests a burial depth of  $\sim 90$  m. This is broadly consistent with other estimations of burial depth using cosmic ray exposure data for ALH84001<sup>9</sup> and the other Martian meteorites (Shuster and Weiss, 2005) that suggest burial depths of at least a few meters for nearly all of their histories. Mikouchi et al. (2006) calculated a burial depth of less than four meters for several nakhlites, which is the original volcanic cooling depth.

#### 4.2. Thermal decomposition models

The two heating scenarios outlined above provide the geological context for the decomposition models developed independently by Brearley (2003) and Treiman (2003). The former is based on carbonate decomposition occurring under “extreme disequilibrium conditions” in which “kinetics are the dominant controlling factor” determining the chemical and physical nature of the magnetites that are formed. This, although never explicitly addressed, is most consistent with the impact event that ejected ALH84001 from Mars. In the latter model, carbonate decomposition occurs “at some depth beneath the Martian surface where the pressure was greater than the atmospheric pressure and the temperature declined slowly.” Under these conditions equilibrium thermodynamics determined the chemical and physical nature of the magnetite formed. In this model, carbonate decomposition occurred prior to ejection, during an earlier epoch, and the eventual ejection event failed to obscure evidence of this earlier thermal episode (as an aside: the Brearley (2003) model is essentially based on inductive reasoning, that is it proceeds from a set of specific observations and experiments to a set of general conclusions. In contrast the Treiman model is based on deductive reasoning, that is, the fundamental postulates of thermodynamics are used to extrapolate the outcome of a single specific event).

It should be noted that these models are necessarily contradictory; that is they cannot both have occurred since application of one model negates the applicability of the other. Indeed as Brearley (2003) noted, “equilibrium phase diagrams have only limited relevance. . . the kinetics of the reaction, rather than the thermodynamics, control the phase and their compositions.” It is also necessary in the subsequent discussion to bear in mind in each model the key question is *not* whether a siderite-magnesite-[calcite] carbonate can undergo preferential decomposition of the sideritic component, since to some extent this may well be true. Rather the question is *can the sideritic component of such a mixed carbonate undergo decomposition to the complete exclusion of the magnesite-calcite components*, since this is what would be necessary to explain the observations of ALH84001 carbonates. The lack of any evidence whatsoever for the partial or complete thermal decomposition of the magnesite and calcite-rich components of ALH84001 carbonates requires that any proposed thermal decomposition mechanism must be tightly limited to the siderite-rich

<sup>9</sup> Although ALH84001 probably formed as a cumulate in an intrusion several 10s of kilometers in depth (McSween and Treiman, 1998), its shock history suggests that it was later excavated to much shallower depths.

Table 5  
Magnetite *d*-spacings: ‘Slow’ and ‘fast’ heated Roxbury siderite.

<i>hkl</i>	Magnetite <sup>a</sup> <i>d</i> -spacings (nm)	Magnesio-ferrite <sup>a</sup> (Mg-ferrite) <i>d</i> -spacings (nm)	Jacobsite <sup>a</sup> (Mn-ferrite) <i>d</i> -spacings (nm)	Mg–Mn-ferrite <sup>a</sup> <i>d</i> -spacings (nm)	Roxbury Siderite (‘Slow’ Heated) This study <i>d</i> -spacings (nm)	Roxbury Siderite (‘Fast’ Heated-Region 1) This study <i>d</i> -spacings (nm)
111	0.484	0.484	0.492	0.491	0.49	0.49
200	0.420	–	–	–	0.42	–
220	0.297	0.296	0.300	0.298	0.30	0.30
311	0.253	0.253	0.256	0.254	0.25	0.25
222	0.242	0.241	0.245	0.243	0.24	–
400	0.210	0.210	0.212	0.211	0.21	0.21
331	0.192	0.192	–	–	–	–
422	0.171	0.171	0.173	0.177	–	0.17

<sup>a</sup> International Centre for Diffraction Data Powder Diffraction Database – PDF-2 release 1998.

carbonate only. Consequently, we address the merit of each model separately, and consider only those aspects of each model that relates specifically to chemical and physical nature of magnetites formed from carbonate decomposition.

#### 4.2.1. Kinetically controlled carbonate decomposition – Brearley (2003) model

The key aspects, as relevant to the discussion herein, of the hypothesis proposed by Brearley (2003) can be condensed into three main points:

1. ALH84001 underwent a rapid heating and cooling event as a consequence of a shock event.
2. The most sideritic component of the carbonate disks “...decomposed preferentially and at a significantly lower temperature than either the magnesite, calcite, or rhodochrosite component in solid solution.”
3. The timescale for this thermal event was short enough to prevent any re-equilibration of the decomposition products or compositional zoning patterns remaining in the residual carbonate.

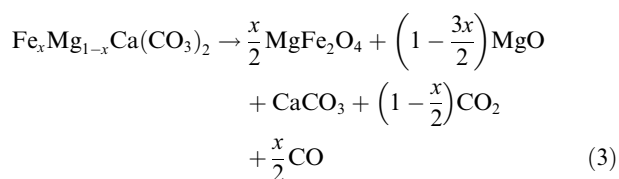
Critical to this hypothesis is the supposition that under conditions characterized by a “high degree of disequilibrium,” partial decomposition of sideritic carbonate would favor the formation of pure magnetite. The rationale is that “under disequilibrium conditions, the earliest phase that forms is the one which is kinetically the easiest to nucleate, in this case, a simple binary oxide [i.e., magnetite] rather than a more complex solid solution [i.e., magnetite-magnesioferrite].” Several problems, however, exist with the Brearley (2003) hypothesis, particularly with over-generalizations that are made on the basis of limited or ambiguous experimental data.

4.2.1.1. *Preferential decomposition of siderite solid solutions.* Brearley (2003) argues that a substantial body of experimental data exists to support the contention “that a complex carbonate solid solution can undergo progressive decomposition, such that one component in solid solution breaks down without the entire phase decomposing.” By way of example, “the behavior of ferromanganous dolomite (Iwafuchi et al., 1983) and carbonates in the

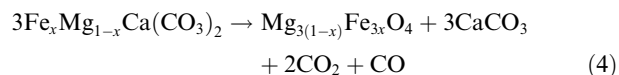
dolomite-ferroan, dolomite-ankerite series (Milodowski et al., 1989) [which] exemplify the decomposition behavior of complex carbonate solutions,” is cited. In both studies “...the decomposition of dolomite and ankerite is complex and involves distinct stages of CO<sub>2</sub> evolution, indicating that decomposition is taking place in different stages.” From this is argued that both studies “...demonstrate that preferential decomposition of one of two carbonate components (i.e., FeCO<sub>3</sub>, MgCO<sub>3</sub>) can occur, leaving the third (CaCO<sub>3</sub>) intact.”

We argue, however, that the relevance of this example is in fact limited and more applicable experimental results need to be considered. In the decomposition studies of ankerite-dolomite solid solutions (Fe<sub>x</sub>Mg<sub>(1-x)</sub>Ca(CO<sub>3</sub>)<sub>2</sub>; 0 ≤ x ≤ 0.7) discussed above, decomposition was interpreted as proceeding in a series of three consecutive stepped reactions, with the first step involves the preferential decomposition of the Fe<sub>x</sub>Mg<sub>(1-x)</sub>CO<sub>3</sub> ‘component’ in the presence of the CaCO<sub>3</sub> ‘component,’ that is:

for (0 ≤ x < 2/3)...



for (2/3 ≤ x ≤ 7/10)...



While it is true that this represents an example of a preferential decomposition of one component (Fe, Mg) of a solid solution carbonate in the presence of another (Ca), it in and of itself does not address the more relevant question as to whether the sideritic component of a siderite-magnesite solid solution would also preferentially decompose (under disequilibrium conditions). The reason that calcitic component of ankerite-dolomite solid solution does not undergo decomposition with the siderite-magnesite solid solution is that neither siderite nor magnesite can form a complete solid solution series with calcite. In contrast,

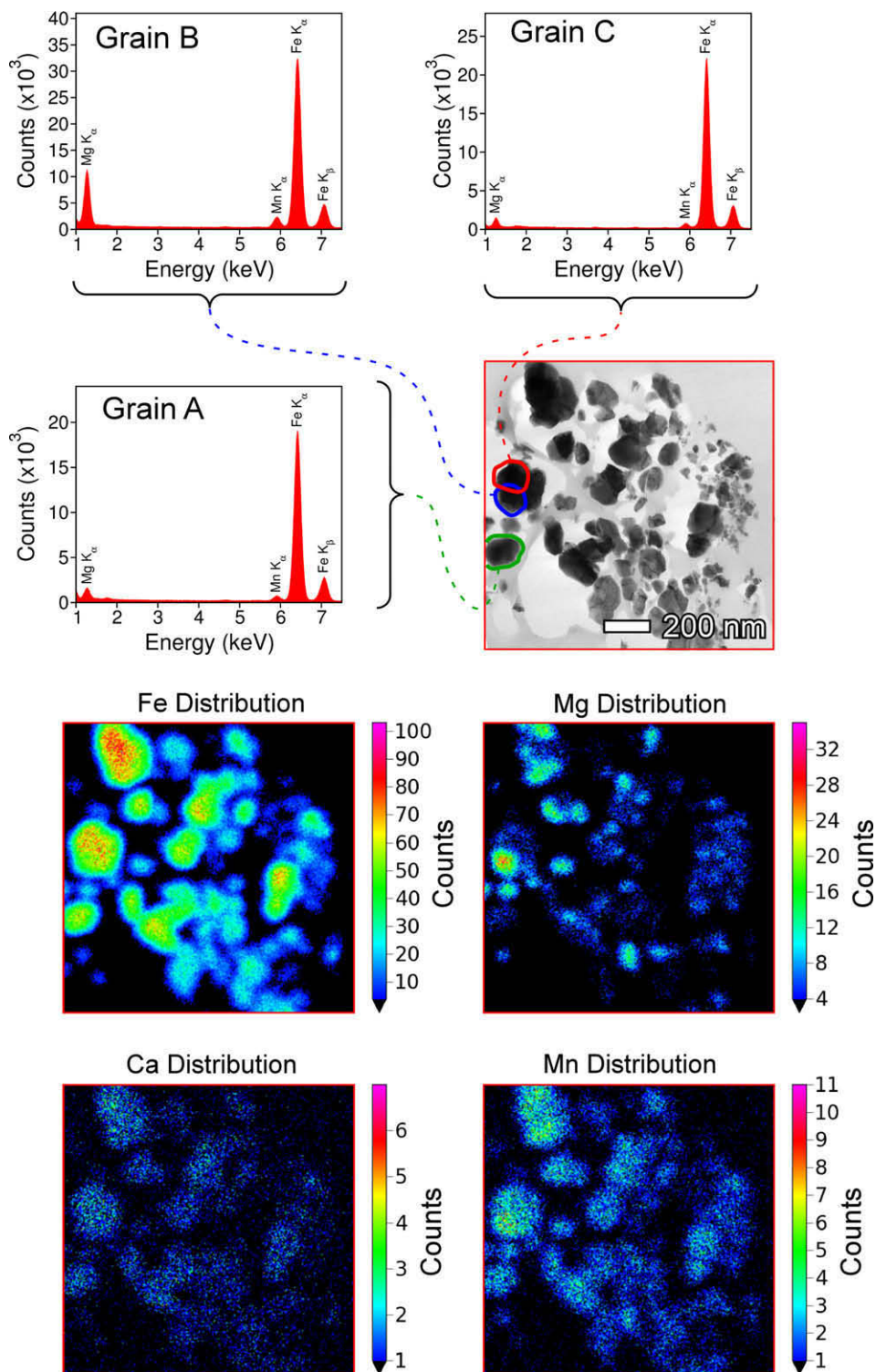


Fig. 6C. Upper views: TEM image and accompanying EDX spectra (1000 s acquisition time) of a grouping of magnetite crystals produced by the 'slow' heating of Roxbury siderite. Three magnetite crystals labeled 'A', 'B', and 'C' (outlined in green, blue, and red) are highlighted. Magnetites 'A' and 'C' contain only minor Mg relative to magnetite 'B', while minor Mn is present in all three grains in approximately the same concentration. Lower views: element maps ( $K_{\alpha}$  line) of Fe, Mg, Ca, and Mn for the entire grouping of magnetites shown in the upper TEM view (red box), illustrating the compositional heterogeneity of Mg in the magnetite product (color bar to right of map represents the number of counts per pixel). Since the observed cation variations mirror those of the unheated Roxbury siderite (see 6A) there is no significant cation diffusion occurring during the 'slow' heating thermal decomposition. That is, the cation composition of a given magnetite grain simply reflects the cation composition of the progenitor carbonate grain from which it formed. (For interpretation of the references to color in this figure legend, the reader is referred to the web version of this paper.)

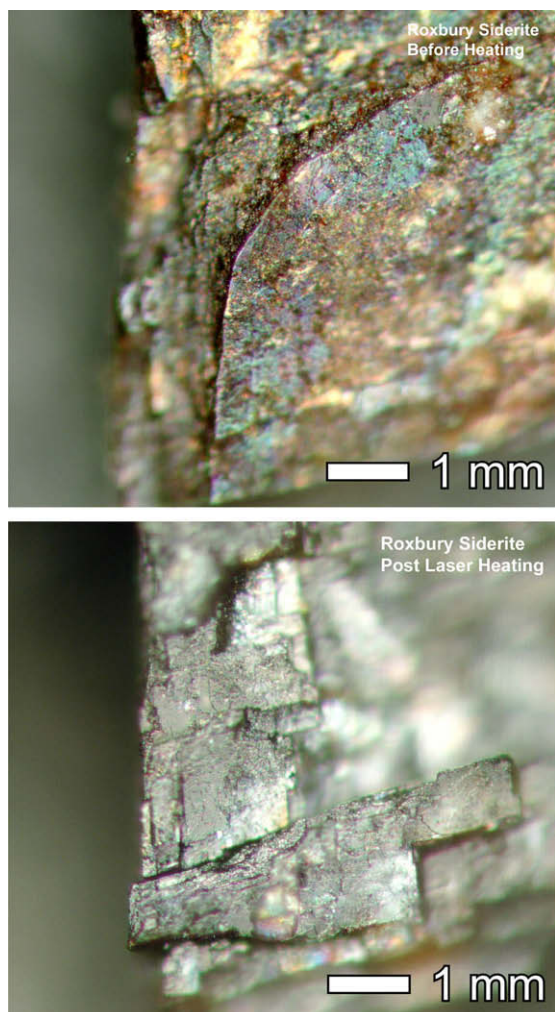


Fig. 6D. Optical views of Roxbury siderite before (upper view), and after ‘fast’ heating (lower view), by laser irradiation (pulsed 10.6  $\mu\text{m}$   $\text{CO}_2$  laser) in a vacuum. The unheated siderite is composed of interlocking mm to sub-mm rhombohedral blocks displaying a variety of iridescent colors due to birefringence. After ‘fast’ heating the color of the carbonate surface is reduced to a silver-gray. (Note: the upper right section of the surface present in the unheated carbonate is absent in the image after heating due to thermally induced cleavage during laser irradiation.)

siderite–magnesite solid solutions do form a complete series between end members. Hence, the decomposition of ankerite-dolomite solid solution is an example of a spinodal decomposition in which a phase transform/separation to calcite and a siderite–magnesite solid solution occurs prior to nucleation and growth of the decomposition product phases. In fact, in these studies the siderite–magnesite solid solution that initially decomposes forms a mixed cation spinel which would appear to directly conflict with the argument for which this reaction was proposed to support, namely that of the exclusive decomposition of the sideritic component of a siderite–magnesite solid solution to form pure magnetite. The data from these experiments show that pure magnetite does not result, rather, a mixed Fe–Mg spinel is the product.

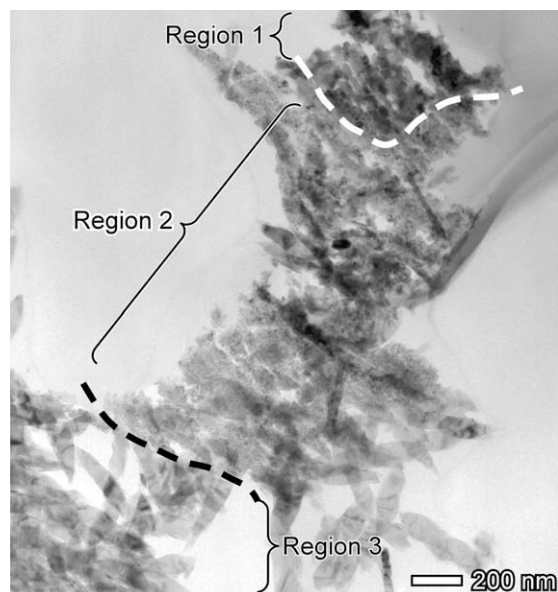


Fig. 6E. TEM view of a region of an ultramicrotome section extracted from the upper surface of the ‘fast’ heated Roxbury siderite sample shown in 6D. The section represents a vertical profile of the irradiated carbonate, with the top of the image corresponding to the uppermost irradiated surface. Three distinct textural regions are apparent and correlate with increasing vertical distance from the irradiated surface. Region 1 represents the uppermost half micron of the carbonate surface that was directly exposed to laser irradiation. This region is composed exclusively of impure magnetite. Underlying this is a layer, several microns thick, composed of a heavily vesiculated carbonate, Region 2, that delineates the transition from the completely decomposed carbonate of Region 1 to the unheated carbonate represented by Region 3. No magnetites were observed in either of the underlying Regions 2 and 3.

While the kinetics of the thermal decomposition of siderite and its solid-solutions have been extensively studied (Dhupe and Gokarn, 1990; Jagtap et al., 1992; Kubas and Szalkowicz, 1971; Zakharov and Adonyi, 1986) great care needs to be taken in interpreting the results of such studies since there are many discrepancies between datasets. The reasons appear to be two fold: first, reaction kinetics are sensitive to the physical parameters of the sample, e.g., degree of crystallinity, surface area, presence of impurities, particles size, and the degree of compaction or porosity. Second, non-isothermal decomposition traces alone can typically be fitted, with good correlation coefficients, to any number of kinetic models. Consequently we consider here the work of Gotor et al. (2000) who have utilized both linear heating rate (TG) and constant rate thermal analysis (CRTA) procedures to investigate the decomposition kinetics of both a pure ‘synthetic’ siderite and a ‘natural’ Mg-bearing siderite ( $\text{Fe}_{0.626}\text{Mg}_{0.300}\text{Mn}_{0.052}\text{Ca}_{0.022}\text{CO}_3$ , under identical conditions. Their results indicated that the thermal decomposition reaction of pure siderite followed an Avrami-Erofeev A2 random nucleation and growth model, while the natural Mg-bearing siderite instead followed an  $F_1$  unimolecular decay model. Fig. 7B shows

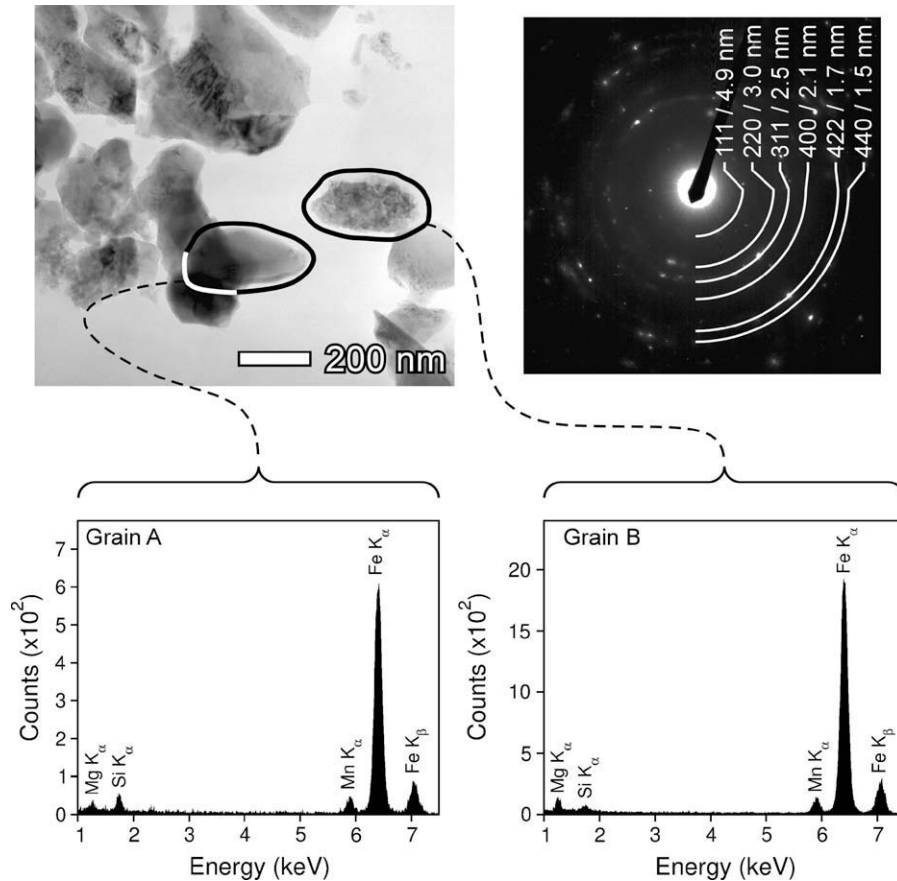


Fig. 6F. TEM image of an ultramicrotome section from Region 1 (see 6E) of ‘fast’ heated Roxbury siderite. The accompanying SAED pattern to the right indicates complete conversion of carbonate to polycrystalline magnetite. Some magnetites are well-formed, single crystals, for example grain ‘A’, while others, such as grain ‘B’, exhibit a mottled texture consistent with a paracrystalline structure that is intermediate between amorphous and crystalline states. The accompanying EDX spectra show that both magnetites ‘A’ and ‘B’ contain minor impurities Mg and Mn that were present in the progenitor Roxbury siderite. Both spectra were acquired using the same analytical spot size and acquisition time of 1000 s.

the model decomposition curves, calculated from the results of Gotor et al. (2000) for both pure and natural siderites under heating rates of 0.52, 5.2, and 52 K · min<sup>-1</sup>. Several important observations can be drawn from the experiments:

- For both pure and natural siderites at all heating rates the onset of decomposition occurs at temperatures that greatly overstep the thermodynamic stability limit predicted for both pure siderite and magnesite–siderite solid solutions.
- The kinetic effect on the stability of siderite as a consequence of magnesium substitution is at least an order of magnitude larger than would be predicted from thermodynamic equilibrium arguments alone.
- Mg-bearing siderite does not decompose in two or more separate stages in which preferential decomposition of the siderite component occurs first.

From the first observation it is clear that even at heating rates that are far slower than those associated with shock heating, decomposition still occurs under conditions that

are far from equilibrium. If this is true then the all the carbonate decomposition studies listed in Table 6 can be considered pertinent to the origin of magnetite in ALH84001 carbonate. Results from these investigations *all show* that decomposition of magnesite–siderite solid solution carbonate under a variety of atmospheres and a range of heating regimes invariably produces an impure Mg-substituted magnetite in which there is little to no evidence of the preferential decomposition of the siderite component of solid solution. While Brearley (2003) suggests “that Fe-rich phases with little or no Mg can be formed as metastable phases during the very earliest stages of decomposition,” it is unclear how this is relevant to magnetite in ALH84001 carbonate for two reasons: first, the magnetites in ALH84001, while sub-micron in size, are still well beyond the size associated with primary nuclei (as demonstrated by their well defined crystal faceting); and, second, since at least 50% of the volume in the magnetite rims of ALH84001 carbonate is accounted for by magnetite and if these magnetites were formed from thermal decomposition, this would require nearly 70% of the carbonate

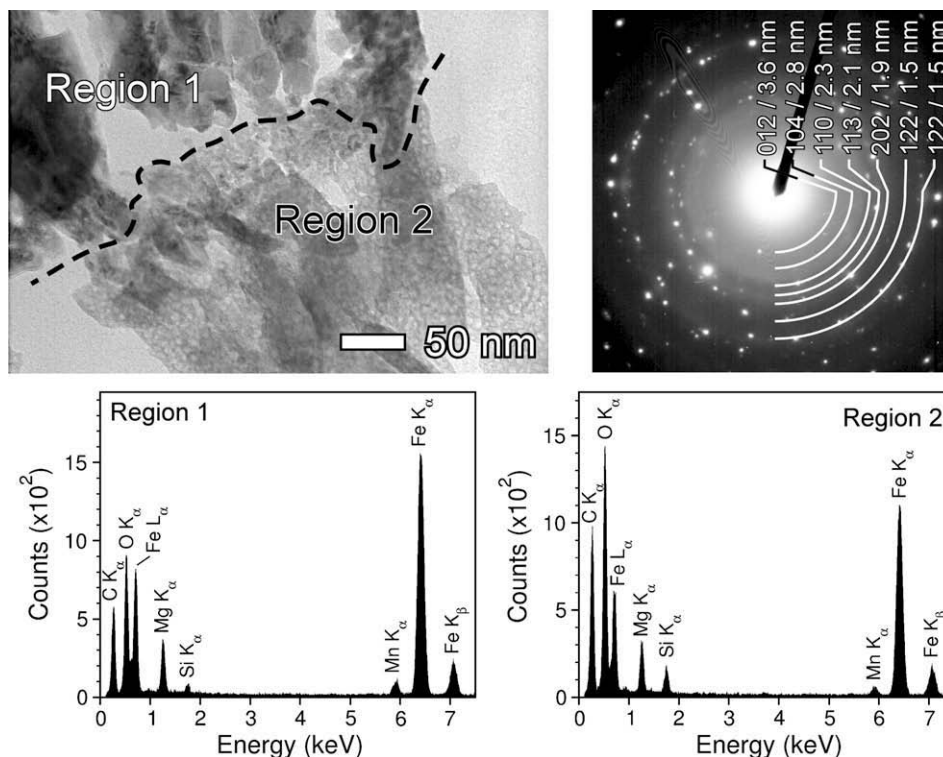


Fig. 6G. TEM view of an ultramicrotome section of the interface between Regions 1 and 2 (see 6E) of the ‘fast’ heated Roxbury siderite indicated by the dashed line. The SAED pattern (upper right) of Region 2 (lower right in TEM view) indicates that it is composed of poorly-to-moderately crystalline carbonate with no associated magnetite. The EDX spectra of both regions show they contain nearly identical amounts of Mg and Mn indicating that the cation composition of the carbonate is preserved in the magnetite decomposition product. That is, the ‘fast’ thermal decomposition of Roxbury siderite does not facilitate the formation of chemical pure magnetite with Mg and Mn cations preferentially partitioning into residual carbonate (and/or oxide phase). The residual C present in the EDX spectrum of Region 1 is due to the epoxy mounting substrate and not from unreacted carbonate. Spectra were acquired using the same analytical spot size ( $\sim 200$  nm) and an acquisition time of 1000 s.

initially present in the rims to have decomposed.<sup>10</sup> A reaction having gone to this extent cannot be construed as being in its initial stages. To be able to rapidly decompose nearly 70% of a siderite-magnetite carbonate in a near instantaneous, highly non-equilibrium, decomposition event and expect the product to be essentially pure magnetite is highly implausible. The Fe/Mg ratio of the decomposition products would more likely be similar to the Fe/Mg ratio of the initial carbonate and show little, if any, chemical fractionation except lost of CO and CO<sub>2</sub>, especially given the results of pulse laser heating experiments on mixed composition Roxbury siderite, which are able to duplicate and even exceed impact shock heating rates and yet always produced impure magnetites (see Results section ‘Roxbury Siderite’; also see Table 6).

<sup>10</sup> Assuming carbonate decomposes via the reaction  $3\text{FeCO}_3 \rightarrow \text{Fe}_3\text{O}_4 + 2\text{CO}_2 + \text{CO}$  then the volume ratio of carbonate to magnetite ( $V_{\text{ratio}}$ ) when the extent of reaction is  $\alpha$  ( $0 \leq \alpha \leq 1$ ) is given by  $V_{\text{ratio}} = \frac{3 \cdot V_{\text{carb}} \cdot (1-\alpha)}{\alpha \cdot V_{\text{magn}}}$ , where  $V_{\text{carb}}$  and  $V_{\text{magn}}$  are the molar volumes of carbonate and magnetite respectively. Assuming  $V_{\text{carb}} \sim 2.9 \text{ cm}^3$  and  $V_{\text{magn}} \sim 4.5 \text{ cm}^3$  and solving for  $\alpha$  when  $V_{\text{ratio}} \sim 1$ , gives the extent of reaction as  $\sim 67\%$ .

4.2.1.2. *Interpretation of siderite–magnesite decomposition studies.* The experimental studies of Koziol (2001) are used in Brearley (2003) as evidence for the preferential decomposition of siderite in a siderite-magnesite solid solution, where it is stated that “pure magnetite was formed, rather than Mg-bearing spinel.” However, this view is not reflected by Koziol (2001) who concludes merely that “preliminary compositional data indicate that magnetite [formed from thermal decomposition] may have a magnesioferrite (MgFe<sub>2</sub>O<sub>4</sub>) component.” The primary results in the partial siderite–magnesite decomposition studies presented in Koziol (2001) and subsequently in Koziol and Brearley (2002) were:

- Residual carbonates all exhibited unit cell contractions, specifically “unit cell volumes [of the residual carbonate] are reduced by 0.27–1.09% with progressively more contraction seen at the more sid[erite]-rich starting compositions.” (Koziol and Brearley, 2002).
- “[m]agnetite formed during these experiments also exhibited contraction of its unit cell, as evidenced by the change in  $d$ -spacing of the mt 311 X-ray reflection.” Specifically, the  $\{311\}$   $d$ -spacing reported for the spinel product formed from partial decomposition

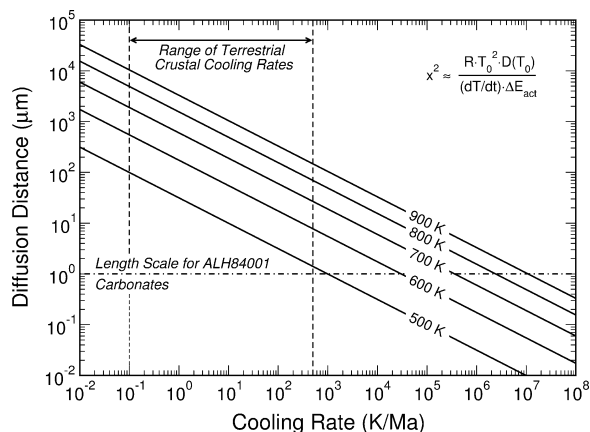


Fig. 7A. Length scale,  $x$ , over which  $\text{Mg}^{2+}$  heterogeneities in calcite ( $\text{CaCO}_3$ ) would be homogenized by thermal diffusion-adapted from Kent et al. (2001). The thermal event that drives the diffusion is assumed to be characterized by an instantaneous rise in temperature to some peak value, followed by slow monotonic cooling back to ambient. Diffusion lengths for peak temperatures  $T_0$  ranging from 500 to 900 K are shown by the solid lines in the plot. For a given initial cooling rate denoted on the abscissa axis, the diffusion distance,  $x$ , can be determined by tracing a vertical line from the abscissa up to the intercept with the solid line corresponding to the given peak temperature. From this intercept a horizontal line traced to the ordinate axis gives the diffusion distance below which compositional heterogeneities would not be preserved. The explicit form of the relationship between diffusion distance and cooling rate is shown on the plot, where  $D_{T_0}$  is the diffusivity of  $\text{Mg}^{2+}$  in calcite at the peak temperature  $T_0$ , where  $E_{\text{Act}}$  is the diffusion activation energy and  $R$  is the gas constant. In the terrestrial geological environment typical cooling rates range from  $\sim 500 \text{ K} \cdot \text{Ma}^{-1}$  to  $\sim 0.1 \text{ K} \cdot \text{Ma}^{-1}$ . Cation heterogeneities in ALH84001 carbonate have length scales of  $x \leq 1 \mu\text{m}$  hence the cooling rate for any putative thermal event responsible for partial carbonate decomposition must have been extremely rapid in a terrestrial geological context.

of  $(\text{Fe}_{0.1}\text{Mg}_{0.9})\text{CO}_3$  was 0.25010 nm, while that for  $(\text{Fe}_{0.8}\text{Mg}_{0.2})\text{CO}_3$  was 0.25227 nm.

Neither observation provides compelling evidence for the preferential decomposition of siderite in a solid solution carbonate to form pure magnetite. In the first case, lacking any data pertaining to the fraction of carbonate that underwent decomposition, the spinel product formed could have had any composition between  $\text{Fe}_3\text{O}_4$  and  $\text{Mg}_{0.3}\text{Fe}_{2.7}\text{O}_4$  (see EA-3). While in the second case, the 0.25010 nm line reported by Koziol (2001) for the  $d_{311}$  line of magnetite formed from the decomposition of  $(\text{Fe}_{0.1}\text{Mg}_{0.9})\text{CO}_3$  is below any reported value of any documented (Mg,Fe)-spinel, and most likely assignable to the  $d_{006}$  line of the undecomposed starting carbonate (see EA-3).

#### 4.2.2. Thermodynamic carbonate decomposition – Treiman model

Treiman (2003) has proposed a “comprehensive abiotic hypothesis” to explain the presence of fine-grained magnetite embedded in ALH84001 carbonate disks that “invokes high pressures, significant time for chemical reactions and

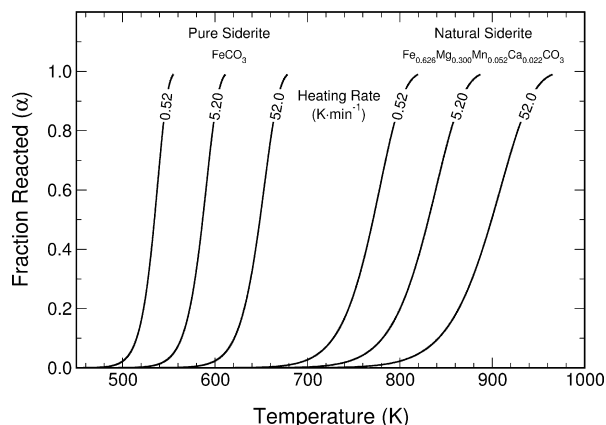


Fig. 7B. Decomposition kinetics of pure and Mg-substituted siderite as a function of linear heating rates. The two curves corresponding to a heating rate of  $0.52 \text{ K} \cdot \text{min}^{-1}$  are the best fits to the experimental data of Gotor et al. (2000) corresponding to an Avrami-Erofeev A2 random nucleation and growth model for pure siderite, and an  $F_1$  unimolecular decay model for the Mg-substituted siderite. The curves corresponding to heating rates of 5.2 and  $52 \text{ K} \cdot \text{min}^{-1}$  are extrapolated using these kinetic models and the pre-exponential factors ( $A$ ) and activation energies ( $E_{\text{Act}}$ ) calculated by Gotor et al. (2000). For pure siderite  $d\alpha = \sqrt{-\log_e[1-\alpha]} \cdot A \cdot \exp(-\frac{E_{\text{Act}}}{RT}) \cdot dt$  where  $A = 7.88127 \times 10^6 \text{ s}^{-1}$  and  $E_{\text{Act}} = 106 \text{ kJ} \cdot \text{mol}^{-1}$ , and for natural siderite  $d\alpha = (1-\alpha) \cdot A \cdot \exp(-\frac{E_{\text{Act}}}{RT}) \cdot dt$  where  $A = 2.52625 \times 10^9 \text{ s}^{-1}$  and  $E_{\text{Act}} = 192 \text{ kJ} \cdot \text{mol}^{-1}$ . Numerical solutions for these differential equations were determined using the Adams–Bashforth–Moulton predictor-corrector method (Mathews and Fink, 2004). The effect of Mg substitution in siderite has a profound consequence on the decomposition temperature and is substantially larger than that predicted based solely on equilibrium thermodynamics.

chemical equilibria.” The geological context for the hypothesis assumes that while ALH84001 was buried at “some depth beneath the Martian surface”, it was subjected to an impact shock (I3 event<sup>11</sup>) that resulted in it being heated “rapidly to super ambient conditions,” resulting in the thermal decomposition of the most sideritic carbonate according to the reaction:



The ALH84001 rock subsequently cooled back slowly to ambient temperature over “a relatively short time geologically... less than centuries.” Under these conditions the size distribution of magnetites is determined by kinetic factors since the nearly instantaneous temperature increase associated with passage of the shock wave results in carbonate decomposition under conditions far from equilibrium. The chemical composition of these magnetites, is however, determined subsequently by thermodynamic constraints during cooling where re-equilibration of magnetite with the host residual carbonate is presumed to have occurred. The conditions of such re-equilibration implicitly requires a closed system in which the  $2\text{CO}_2 + \text{CO}$  gas phase evolved during the initial decomposition is not dissipated or diluted,

<sup>11</sup> I3 event in shock chronology proposed by Treiman (1998).

Table 6  
Previous decomposition studies of natural and synthetic siderites.

Composition of Unheated Carbonate	Atmosphere	Decomposition Temperature and Product Phases	References
Synthetic solid solution siderite (0.0 to 100.0 mol.% FeCO <sub>3</sub> )	O <sub>2</sub>	<ul style="list-style-type: none"> <li>• 770 °C</li> <li>• Solid solutions from 0–66.6 mol.% FeCO<sub>3</sub> ⇒ <b>magnesioferrite spinel (MgFe<sub>2</sub>O<sub>4</sub>) and MgO</b></li> <li>• Solid solutions from 66.7 to 100 mol.% FeCO<sub>3</sub> ⇒ <b>magnesioferrite spinel (MgFe<sub>2</sub>O<sub>4</sub>) and Fe<sub>2</sub>O<sub>3</sub></b></li> </ul>	(Chai and Navrotsky, 1996a)
Ankerite solid solution <sup>a</sup> Ca(Fe <sub>x</sub> Mg <sub>1-x</sub> )(CO <sub>3</sub> ) <sub>2</sub> where 0 < x < 1	O <sub>2</sub>	<ul style="list-style-type: none"> <li>• 770 °C</li> <li>• <b>CaO</b></li> <li>• <b>MgO</b></li> <li>• <b>Ca<sub>2</sub>Fe<sub>2</sub>O<sub>5</sub></b></li> </ul>	(Chai and Navrotsky, 1996b)
(Fe <sub>0.7</sub> Mg <sub>0.3</sub> )CO <sub>3</sub>	Vacuum	<ul style="list-style-type: none"> <li>• Decomposition begins 452 °C</li> <li>• <b>Mixed Mg–Fe oxides</b></li> <li>• <b>No MgO</b></li> </ul>	(Gotor et al., 2000)
Mixed cation FeCO <sub>3</sub> (1) 95.3 mol.% FeCO <sub>3</sub> , 4.2 mol.% MnCO <sub>3</sub> , 0.4 mol.% MgCO <sub>3</sub> (2) 85.5 mol.% FeCO <sub>3</sub> , 4.0 mol.% MnCO <sub>3</sub> , 7.6 mol.% MgCO <sub>3</sub> , 0.9 mol.% CaCO <sub>3</sub> (3) 81.7 mol.% FeCO <sub>3</sub> , 6.4 mol.% MnCO <sub>3</sub> , 9.5 mol.% MgCO <sub>3</sub> , 1.5 mol.% CaCO <sub>3</sub>	N <sub>2</sub> and O <sub>2</sub>	<ul style="list-style-type: none"> <li>• Decomposition begins at lower <i>T</i> in N<sub>2</sub></li> <li>• In N<sub>2</sub>: <b>mixed Mg–Mn ferrites</b></li> <li>• In O<sub>2</sub>: <b>mixed Mg–Mn ferrites and hematite</b></li> <li>• <b>Spinel impurities increase with increasing carbonate impurities</b></li> </ul>	(Gallagher and Warne, 1981b)
Mn-bearing natural siderite	Air	<ul style="list-style-type: none"> <li>• 480–530–700 (°C)</li> <li>• <b>Hematite (initial)</b></li> <li>• <b>Mn-ferrite (final)</b></li> </ul>	(Hakonardottir et al., 2002)
Siderite: 79.16 wt.% FeCO <sub>3</sub> , 1.04 wt.% MnCO <sub>3</sub> , 16.40 wt.% MgCO <sub>3</sub> , 3.76 wt.% Fe <sub>2</sub> O <sub>3</sub> , 0.43 wt.% CaCO <sub>3</sub>	N <sub>2</sub> and O <sub>2</sub>	<ul style="list-style-type: none"> <li>• 0 to 1000 °C</li> <li>• N<sub>2</sub>: <b>major impurities incorporated into the spinel product</b></li> <li>• O<sub>2</sub>: no spinel intermediate phases detected</li> </ul>	(Gallagher and Warne, 1981a)
Siderites: Approximate mole fraction Fe (Fe/(Fe + Mn + Mg + Ca)) (1) 0.0 (2) 0.3 (3) 0.6 (4) 0.7 (5) 0.8 (6) 0.9	N <sub>2</sub>	<ul style="list-style-type: none"> <li>• Onset and Peak Temperature of Decomposition (°C): (1) ~560, ~640 (2) ~530; ~650 (3) ~480; ~580 (4) ~450; ~540 (5) ~440; ~540 (6) ~440; ~540</li> <li>• Mixed composition products from mixed composition siderite <ul style="list-style-type: none"> <li>◦ Ferroan magnesite ⇒ <b>Mg-ferrite</b></li> <li>◦ Mn–Mg–siderite ⇒ <b>Mn–Mg–Fe-oxides</b></li> </ul> </li> </ul>	(Dubrawski, 1991b)
Bakal siderite (impure)	Air	<ul style="list-style-type: none"> <li>• Decomposition begins 350 °C</li> <li>• <b>MgFe<sub>2</sub>O<sub>4</sub></b></li> </ul>	(Bagin et al., 1974)
Siderite: (Fe <sub>0.79</sub> Mn <sub>0.12</sub> Mg <sub>0.07</sub> Ca <sub>0.02</sub> )CO <sub>3</sub>	Air	<ul style="list-style-type: none"> <li>• <b>Magnesiowustite</b></li> <li>• 700 °C</li> <li>• <b>Mn-magnetite</b></li> </ul>	(Isambert and Valet, 2003)
Ankerite: (Ca(Mg,Fe,Mn)(CO <sub>3</sub> ) <sub>2</sub> )	CO <sub>2</sub> (1 atm)	<ul style="list-style-type: none"> <li>• Siderite, 500–700 °C</li> <li>• Ankerite, 600–800 °C</li> <li>• <b>Significant amounts of Mn and Mg in ferrites</b></li> </ul>	(Cohn, 2006)

Table 6 (continued)

Composition of Unheated Carbonate	Atmosphere	Decomposition Temperature and Product Phases	References
Copper Lake Siderite ~0 to 21 mol.% Mg	Impact shock CO <sub>2</sub> (10 <sup>-3</sup> torr) 30 to 49 GPa	<ul style="list-style-type: none"> <li>• &gt;470 °C</li> <li>• Ferrites with range in composition (~0 to 21 mol.% Mg)</li> </ul>	(Bell, 2007)
Siderite: Fe <sub>0.79</sub> Mn <sub>0.12</sub> Mg <sub>0.07</sub> Ca <sub>0.02</sub>	Laser under vacuum 8.4 to 25.9 GPa,	<ul style="list-style-type: none"> <li>• Mn-“magnetite-like”</li> </ul>	(Isambert et al., 2006)
(1a,b) Siderite (2a,b) Magnesite (3a,b) Calcite	N <sub>2</sub> and O <sub>2</sub>	<ul style="list-style-type: none"> <li>• Decomposition begins at lower <i>T</i> in N<sub>2</sub>: (1a) N<sub>2</sub> 450–550 °C (1b) O<sub>2</sub> increased by ~50 °C over 1a (2a) N<sub>2</sub>~500–600 °C (2b) O<sub>2</sub> increased by ~70 °C over 2a (3a) N<sub>2</sub>~680–780 °C (3b) O<sub>2</sub> increased by ~150 °C over 3a</li> </ul>	(Ware and French, 1984)
Siderite (>90 wt.% FeCO <sub>3</sub> ) Ca-siderite (70–90 wt.% FeCO <sub>3</sub> , ~10 wt.% CaCO <sub>3</sub> ) Mn-siderite (up to 28 wt.% MnCO <sub>3</sub> ) Mg-siderite (10–30 wt.% MgCO <sub>3</sub> ) High Mg-siderite (30–60 wt.% MgCO <sub>3</sub> ) Ferroan magnesite (>60 wt.% MgCO <sub>3</sub> )	N <sub>2</sub> , O <sub>2</sub> , CO <sub>2</sub> , H <sub>2</sub> O	<ul style="list-style-type: none"> <li>• Siderite decomposition <i>T</i> increases proportional to extent of substitution by Mg, Mn, and Ca</li> <li>• Decomposition <i>T</i> decreases with increasing FeCO<sub>3</sub></li> <li>• Non-linear decrease in decomposition <i>T</i> with increase in partial pressure H<sub>2</sub>O</li> <li>• Decomposition <i>T</i> increases non-linearly with increasing CO<sub>2</sub> <ul style="list-style-type: none"> <li>◦ Low partial pressure (&lt;25 kPa) CO<sub>2</sub> produces increase in decomposition <i>T</i> (e.g., in N<sub>2</sub>, FeCO<sub>3</sub> decomposes at 375 °C; in CO<sub>2</sub>, FeCO<sub>3</sub> decomposes at 500 °C)</li> </ul> </li> </ul>	(Hurst et al., 1993)

<sup>a</sup> Results typical for decomposition of carbonates in ankerite–dolomite solid solution series. Compositions of phases formed are variable, determined by compositions of the precursor carbonates. Formation of chemically pure Fe<sub>3</sub>O<sub>4</sub> by thermal decomposition of carbonates in this series has not been reported.

and furthermore the  $f_{\text{O}_2}$  is solely defined by this  $2\text{CO}_2 + \text{CO}$  gas phase. Unfortunately, the merit of the Treiman (2003) hypothesis is undermined by the use of erroneous or questionable thermodynamic data and the application of incongruous experimental results as discussed below.

**4.2.2.1. Siderite stability field.** The thermodynamic stability field of siderite is calculated incorrectly in Treiman (2003) and this subsequently affects many of the later calculations. In a closed system, the decomposition of siderite according to reaction (5) will be a function of the intensive variables of pressure and temperature, and if the siderite is not pure, but rather present as a solid solution, its activity as well. In calculating the siderite stability field Treiman (2003) used the thermodynamic software package THERMOCALC (Holland and Powell, 1998; Powell et al., 1998) in combination with a regular solid solution activity-composition model (Chai and Navrotsky, 1996a) to describe the siderite–magnesite solid solution series. Regrettably, the results of these calculations are incorrect since it appears that no consideration was made to address the absence of an appropriate equation-of-state (EOS) for CO in the THERMOCALC package, which only includes a compensated Redlich-Kwong EOS to determine fugacities for CO<sub>2</sub> and H<sub>2</sub>O. Hence, all the calculations in Treiman (2003) relating to siderite decomposi-

tion involving the presence of a CO gas phase product are wrong. Using the most recent version of the thermodynamic dataset used by THERMOCALC v3.26 (and hence for referred to as HP98<sup>12</sup>), in combination with the Peng–Robertson–Gasem cubic EOS (Gasem et al., 2001), and assuming Lewis Randall fugacity mixing rules (Lewis and Randall, 1961), the correct siderite stability *P*–*T* plot is shown in Fig. 7C. From this it is apparent that the correct thermodynamic decomposition temperature of siderite is actually considerably higher than that shown Figs. 3 and 4 of Treiman (2003) (a more comprehensive description of the relevant thermodynamic calculations can be found in EA-4).

**4.2.2.2. Composition of magnesioferrite–magnetite solid solutions.** The equilibrium extent of Mg<sup>2+</sup> substitution in the magnetite product produced from the decomposition of sideritic carbonate can be addressed thermodynamically by casting an Mg<sup>2+</sup>-substituted magnetite as a solid solution between magnesioferrite and magnetite proper, that is:

<sup>12</sup> <http://www.earthsci.unimelb.edu.au/tpg/thermocalc>

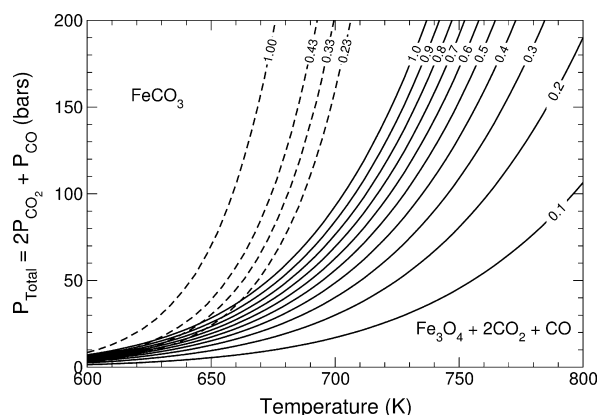
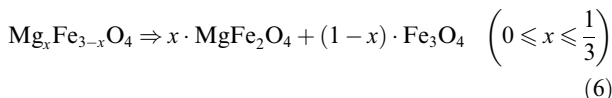


Fig. 7C. Univariant equilibrium decomposition curves (solid lines) calculated for siderite-magnesite solid solutions in  $P$ - $T$  space subject to the reaction. Calculations were made using thermodynamic data from the updated Holland and Powell (1998) database (THERMOCALC Ver. 3.26) and assuming a Peng–Robinson–Gasem EOS for gas phase species (Gasem et al., 2001). The numbers associated with each curve represent the mole fraction of siderite present in the carbonate solid solution (i.e.,  $x$  in  $(\text{Fe}_x\text{Mg}_{1-x})\text{CO}_3$ ) with the curve labeled “1.0” representing pure siderite ( $x = 1$ ). The set of four curves shown by the dashed lines represent those calculated erroneously by Treiman (2003).



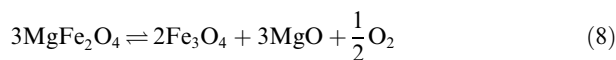
Under the conditions of siderite decomposition proposed by Treiman (2003) two thermodynamic methods are developed to provide limits to the mole fraction of magnesioferrite present in ALH84001 magnetites. Both approaches appear to yield similar results, namely that the mole fraction of magnesioferrite is expected to be very low and probably undetectable by TEM/EDX. This is, however, misleading as both approaches use either erroneous or logically inconsistent data and the similarity in the results for each is simply coincidental, as discussed in EA-5, where we show that because of the omission of an equation of state in the THERMOCALC package used by Treiman (2003), the calculated minimum concentration of Mg-spinel component in the Fe-spinel decomposition product is  $\sim 3\times$  higher than estimated by Treiman (2003) and would be detected by TEM/EDX analysis.

As shown in EA-5, the use of data from multiple sources in the THERMOCALC treatment of oxygen fugacity also produces a significant underestimation of the activity of the magnesioferrite component in the resulting decomposition product. A more consistent database predicts that the magnesioferrite component would be much higher and detectable by TEM/EDX techniques.

**4.2.2.3. Where is the graphite? Metastability of  $\text{CO}_2$ - $\text{CO}$  gas mixture and the formation of graphite.** Central to the Treiman (2003) hypothesis is that the decomposition of siderite occurs in a closed system via reaction (1) to produce magnetite and a  $2\text{CO}_2 + \text{CO}$  gas phase. It is the presence of this  $2\text{CO}_2 + \text{CO}$  gas that allows re-equilibration of  $\text{Mg}^{2+}$  between magnetite and carbonate via the following reaction:



Additionally it is also used to define the  $f_{\text{O}_2}$  conditions for the reduction of magnesioferrite to magnetite proper and periclase via the following reaction:



Nevertheless, thermodynamically under the reaction conditions presumed for siderite decomposition (“pressures on the order of tens to hundreds of bars” and temperatures in the range of 600–800 K) CO would be unstable with respect to disproportionation via the Boudouard reaction:



Consequently, the thermodynamically favored reaction for thermal decomposition of sideritic carbonates is:



Fig. 7D shows the  $P$ - $T$  phase stability curves for both pure siderite and siderite-magnesite solid solutions calculated using thermodynamic data from THERMOCALC and assuming the regular solid-solution mixing model described previously for siderite-magnesite solid solutions. While Treiman (2003) does note that formation of a graphite phase ought to be one of the products of siderite decomposition under conditions approaching equilibrium, it is argued that “formation of graphite, the thermodynamically stable phase, would be kinetically hindered.” In other words, although the Boudouard reaction is thermodynamically spontaneous, graphite deposition in the absence of a catalyst is minimal due to the high activation barrier. For practically all laboratory investigations of siderite decomposition, it is true that in most cases experiments are conducted over time intervals of less than a few days. Hence, while French and Eugster (1965) noted

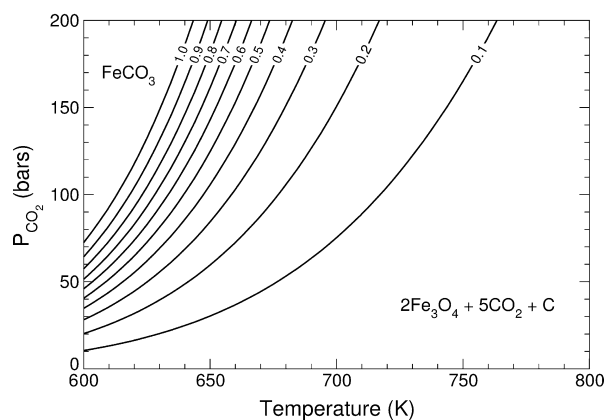


Fig. 7D. Univariant decomposition curves for siderite-magnesite solid solutions in  $P$ - $T$  space according to the reaction. The numbers associated with each curve represent the mole fraction of siderite present in the solid solution, with the curve labeled “1.0” representing pure siderite. Calculations were made using thermodynamic data from the updated Holland and Powell (1998) database (THERMOCALC Ver. 3.26) and assuming a Peng–Robinson–Gasem EOS (Gasem et al., 2001) for gas phase species.

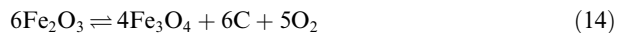
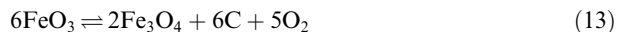
that “it is possible that rates of equilibration between graphite and gas are slow enough so that a gas phase with metastably low  $\text{CO}_2/\text{CO}$  ratios could be maintained without precipitation, particularly at low temperatures” their experimental data indicated “that equilibrium is attained through precipitation of graphite during runs of long (*two weeks*) duration.” Tamaura and Tabata (1990) showed conversion efficiencies near 100% using cation excess magnetite ( $\text{Fe}_{2.887}\text{O}_4$ ) as a catalyst in  $\text{CO}_2$  to form graphite at 563 K. It should also be noted that the use of  $\text{CO}_2$ -CO gas furnace mixtures to fix  $f_{\text{O}_2}$  in mineral equilibria investigations are usually restricted to temperatures above  $\sim 1200$  K due to problems associated with graphite precipitation (Huebner, 1975; Jurewicz et al., 1993). These studies all suggest that graphite should be one of the decomposition phases in ALH84001, if siderite was decomposed to form magnetite.

Although no exact analogues to ALH84001 carbonate have been identified in the terrestrial geological record, ancient ( $>3.5$  Ga) secondary carbonate deposits occurring in vein fractures of rocks forming the in 3.8 Ga old Isua supracrustal belt in southern West Greenland do provide an interesting comparison (Zuilen et al., 2002). These carbonate deposits are intimately associated with the presence of magnetite and graphite inclusions. Carbon isotope analyses indicate the parentage of the graphite to be derived from the carbonate, and it is generally accepted that both the magnetite and graphite formed by “the disproportionation of  $\text{Fe}^{+2}$ -bearing carbonates at high temperature” as shown in reaction (10) (Zuilen et al., 2002).

Since no graphite has ever been observed by us in any ALH84001 carbonate, if we assume the magnetite formed by thermal decomposition then the time available for the attainment of thermodynamic equilibrium would have had to have been short, perhaps on the order of weeks (or less depending on the ability of magnetite to promote precipitation of graphite through surface catalysis). This is a far more rigorous constraint than the “. . . less than centuries” as proposed by Treiman (2003), and would arguably be too short to allow any significant degree of chemical equilibration between magnetite and carbonate in ALH8001.

**4.2.2.4. Siderite-magnetite stability and oxygen fugacity.** In the thermodynamic model of siderite decomposition it has been implicitly assumed that the system is closed. Although not specifically a criticism of the Treiman (2003) hypothesis it is useful at this point to consider the consequences if this were not the case. Specifically let us consider the situation in which the  $f_{\text{O}_2}$  is influenced by the external environment, as is often the case in geological settings. Since the thermal decomposition of siderite to magnetite involves a change in oxidation state of the Fe cation we can expect there to be only a limited range of  $f_{\text{O}_2}$  values for which both siderite and magnetite can coexist. This should be contrasted with the analogous decompositions of magnesite to periclase or calcite to lime which are  $f_{\text{O}_2}$  invariant since they involve no changes in redox. In order to explicitly determine the  $f_{\text{O}_2}$  dependence of the partial decomposition of siderite to magnetite we need to consider the stability field of siderite

in  $P - T - f_{\text{O}_2}$  space, which is defined by the bivariate reaction<sup>13</sup> surfaces representing oxidation to either hematite or magnetite, and the interconversion between hematite and magnetite, that is:



From inspection of reactions (12) and (13) it can be seen that their equilibrium surfaces in  $P - T - f_{\text{O}_2}$  space will intersect on the graphite buffer surface defined by the reaction:



To visualize these relationships it is convenient to consider 2-D slices through the relevant region of  $P - T - f_{\text{O}_2}$  space perpendicular to one of the axis vectors, in our case this will be pressure. Under isobaric conditions the bivariate reaction surfaces for reactions (11–14) appear as univariate curves in  $T - f_{\text{O}_2}$  space. Provided that the partial pressure of  $\text{O}_2$  defined by the value of  $f_{\text{O}_2}$  is negligible in comparison to the total gas pressure of the system, the position of the univariate curves defined by reactions (11–14) can be calculated by equating the respective thermodynamic equilibrium constants to the Gibbs free energy of reaction, that is:

$$f_{\text{O}_2} = \exp \left[ -\frac{\Delta G_{rxn}^{P_1, T_1}}{R \cdot T_1} \right] \quad (16)$$

<sup>13</sup> The Gibbs phase rule  $\omega = \eta + \nu - \phi - r$  establishes a relationship between the variance ( $\omega$ ) of a thermodynamic system and the number of components ( $\eta$ ), the number of intensive variables ( $\nu$ ), the number of phases ( $\phi$ ) and the number of independent chemical reactions that are occurring in the system ( $r$ ). In the Fe-C-O system there are three components (i.e., Fe, C, and O) so  $\eta = 3$ , while in  $P - T - f_{\text{O}_2}$  space there are three intensive variables (i.e.,  $P$ ,  $T$  and  $f_{\text{O}_2}$ ) and so  $\nu = 3$ . Thus the Gibbs phase rule can be rewritten as  $\omega = 6 - \phi - r$ . For reactions (11, 12) we have two solid phases in equilibrium with a gas so  $\phi = 3$ , and setting  $r = 1$  we find the variance  $\omega = 2$  defining a surface in  $P - T - f_{\text{O}_2}$  space. Under isobaric conditions in  $T - f_{\text{O}_2}$  space the number of intensive variables is reduced to  $\nu = 2$  (i.e.,  $T$  and  $f_{\text{O}_2}$ ) so that  $\omega = 1$  defining a univariate curve. In the case of reaction (13) before applying the phase rule it must necessary to realize that we are implicitly assuming the presence of an imaginary or inert gas is also present in the system otherwise we would not be able to vary the partial pressure of  $\text{O}_2$  since it would be the only gas in the system and hence would always be at the system pressure  $P$ . We account for this imaginary or inert gas by increasing the number of components necessary to describe the system, i.e.,  $\eta = 3 + 1 = 4$ . Since we have three solid phases in equilibrium with a gas we have  $\phi = 4$  and  $r = 1$ . Now applying the phase rule we obtain a variance  $\omega = 4 + 3 - 4 - 1 = 2$  in  $P - T - f_{\text{O}_2}$  space and  $\omega = 1$  in  $T - f_{\text{O}_2}$  space. Finally for reaction (14) since C is absent the number of components is two (i.e., Fe and O) + the imaginary or inert gas necessary allow variation of the partial pressure of  $\text{O}_2$ , hence  $\eta = 3$ . There are two solids and a gas phase described by a single reaction so  $\phi = 3$  and  $r = 1$ . Hence from the phase rule the variance  $\omega = 3 + 3 - 3 - 1 = 2$  in  $P - T - f_{\text{O}_2}$  space and  $\omega = 1$  in  $T - f_{\text{O}_2}$  space.

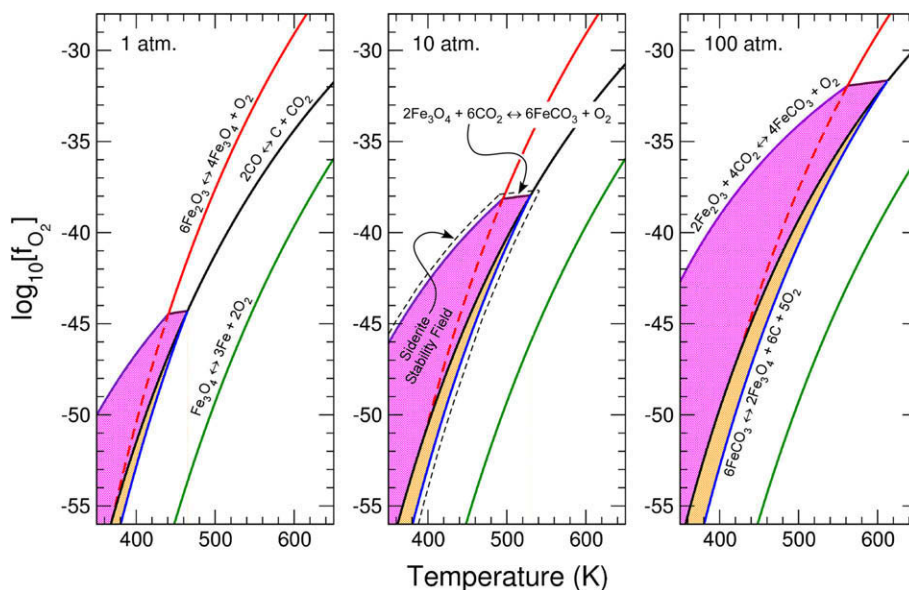


Fig. 7E. Siderite stability field in  $P$ – $T$ -space, using thermodynamic data from the updated Holland and Powell (1998) database (THERMOCALC Ver. 3.26) and assuming a Peng–Robinson–Gase EOS for gas phase species (Gase et al., 2001). Each plot represents a 2-D slice through  $P$ – $T$ -space under isobaric conditions corresponding to pressures of 1, 10, and 100 bars, respectively. The siderite stability field is indicated by the magenta plus gold shaded wedge (shown outlined by the black dashed line in the middle plot) that splits the hematite and magnetite fields. The presence of siderite coexisting with magnetite in the absence of graphite occupies a restricted region in  $T$ -space defined by the curve, which defines the upper limit of the siderite stability field. This line connects the two invariant points in  $T$ -space corresponding at lower temperature to the coexistence of siderite + magnetite + hematite + gas, and at higher temperature to siderite + magnetite + graphite + gas. Note that the siderite stability field is itself divided into the magenta and gold shaded regions by the black line corresponding to the equilibrium  $2\text{CO} \rightleftharpoons \text{C} + \text{CO}_2$ . (For interpretation of the references to color in this figure legend, to reader is referred to the web version of this paper.)

where  $\Delta G_{rxn}^{P_1, T_1}$  is the free energy of the given reaction calculated at pressure  $P_1$  and temperature  $T_1$ . In the case of reaction (15) this is complicated by the necessity of taking into account the Boudouard reaction ( $\text{C} + \frac{1}{2}\text{O}_2 \rightleftharpoons \text{CO}$ ) so that thermodynamic expression for the dependence becomes:

$$f_{\text{O}_2} = [\gamma_{\text{CO}} \cdot P_{\text{CO}}]^2 \cdot \exp\left(\frac{\Delta G_{rxn}^{P_1, T_1}}{R \cdot T_1}\right) \quad (17)$$

where  $\gamma_{\text{CO}}$  is the pure gas fugacity of CO at a partial pressure  $P_{\text{CO}}$  (see EA-6). The values of  $\Delta G_{rxn}^{P_1, T_1}$  for each of the reactions can be evaluated using the same procedure as that described for the siderite decomposition reaction (see EA-4). Using thermodynamic data from the most recent HP98 dataset and assuming a Peng–Robertson–Gase cubic EOS for gas phase species the calculated univariant curves for reactions (11–15) at isobaric pressures of 1, 10 and 100 bars are shown in Fig. 7E.

From Fig. 7E the stability field for siderite can be viewed as a narrow wedge separating the hematite and magnetite stability fields that expands upward to lower  $f_{\text{O}_2}$  values with increasing pressure. Under the range of temperatures and pressures considered (350–650 K and 1–100 bar) siderite is only thermodynamically stable at relatively low  $f_{\text{O}_2}$  values<sup>14</sup> with the upper section of the stability wedge defined by the interface between the siderite + gas  $\rightleftharpoons$  magnetite + gas fields corresponding to reaction (12). The upper and lower

temperature limits for reaction (12) are bound by two invariant points in  $T$ – $f_{\text{O}_2}$  space. The low temperature limit corresponds to the intersection of reactions (11, 12, and 14) at which point siderite is in equilibrium with both hematite and magnetite according to the equilibrium<sup>15</sup>:



While the higher temperature limit corresponds to the intersection of reactions (12, 13) and the graphite buffer reaction (15) at which point siderite is in equilibrium with magnetite and graphite according to the equilibrium<sup>16</sup>:

<sup>15</sup> Applying the Gibbs phase rule we start with  $\omega = \eta + \nu - \pi - r$ . In the Fe–C–O, system we have three components plus an imaginary or inert gas (see footnote 14) so  $\eta = 3 + 1 = 4$ . There are three solid phases in equilibrium with a gas phase and so  $\phi = 4$ . The system has two independent chemical reactions (11) and (12) and so  $r = 2$  (note reaction (14) is not independent since reaction (13) =  $\frac{1}{2}$  · reaction (11) – reaction (12)). Hence in  $T$ – $f_{\text{O}_2}$  space ( $\nu = 2$ ) the variance is given by  $\omega = 4 - 2 - 4 + 2 = 0$  defining an invariant point.

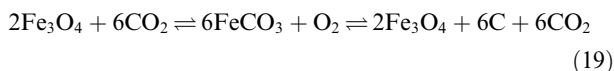
<sup>16</sup> Again applying the Gibbs phase rule  $\omega = \eta + \nu - \phi - r$ , we have three components for the Fe–C–O system plus an imaginary or inert gas so  $\eta = 3 + 1 = 4$ . There are three solid phases and one gas phase so  $\omega = 4$ , and we have two independent chemical reactions (12) and (13) so  $r = 2$  (note reaction (15) is not independent since reaction (15) =  $\frac{1}{6}$  · (reaction (12) + reaction (13))). Hence in  $T$ – $f_{\text{O}_2}$  space ( $\nu = 2$ ) the variance is given by  $\omega = 4 + -2 - 4 + 2 = 0$  again defining an invariant point.

<sup>14</sup> For reference  $f_{\text{O}_2}$  values for the current atmospheres of Earth and Mars are  $\sim 2 \times 10^{-1}$  and  $1 \times 10^{-4}$  bar, respectively.

Table 7  
ALH84001 carbonate compositions and inferred magnetite volumes.

	Outer magnetite rim <sup>a</sup>	$V_{\text{fraction magnetite}}$
Initial carbonate	$\text{Fe}_{0.424 \pm 0.068} \text{Mg}_{0.558 \pm 0.072} \text{Ca}_{0.065 \pm 0.015} \text{Mn}_{0.012 \pm 0.005} \text{CO}_3$	
Residual carbonate	$\text{Fe}_{0.227 \pm 0.057} \text{Mg}_{0.716 \pm 0.024} \text{Ca}_{0.047 \pm 0.035} \text{Mn}_{0.010 \pm 0.003} \text{CO}_3$	15.2%
	Inner magnetite rim <sup>a</sup>	
Initial-carbonate	$\text{Fe}_{0.752 \pm 0.144} \text{Mg}_{0.241 \pm 0.143} \text{Ca}_{0.004 \pm 0.005} \text{Mn}_{0.003 \pm 0.001} \text{CO}_3$	
Residual carbonate	$\text{Fe}_{0.393 \pm 0.032} \text{Mg}_{0.599 \pm 0.031} \text{Ca}_{0.007 \pm 0.001} \text{Mn}_{0.002 \pm 0.002} \text{CO}_3$	42.9%

<sup>a</sup> From Treiman (2003).

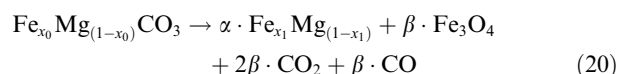


Hence, it is therefore apparent that the partial decomposition of siderite to magnetite in the absence of graphite is only possible under an extremely limited set of  $f_{\text{O}_2}$  conditions ( $-44.46 < f_{\text{O}_2} < -44.30$  @ 1 bar;  $-38.15 < f_{\text{O}_2} < -37.95$  @ 10 bar; and,  $-31.95 < f_{\text{O}_2} < -31.67$  @ 100 bar).

4.2.2.5. *Why is the residual carbonate composition so different?* Table 1 of Treiman (2003) gives the composition of individual carbonate grains present in both in the inner and outer magnetite-bearing layers. The average composition of these carbonate grains in the two layers therefore defines the residual carbonate composition that would have had to have been in equilibrium with magnetite during decomposition under thermodynamic control. Table 7 shows the average carbonate composition of both inner and outer magnetite layers based on data from Table 1 of Treiman (2003). This suggests that in the outer magnetite layer a residual carbonate with a 23 mol.% siderite component would have been stable with respect to further decomposition. Yet, the residual carbonate in the inner magnetite rim has a siderite component of ~39 mol.%, almost twice that of the outer rim. Such a carbonate would not have been thermodynamically stable under the temperature at which the outer carbonate would have been in equilibrium with magnetite. In the absence of any plausible mechanism to enable a large temperature gradient between the two layers, whose separation is only on the order of tens of microns, the sideritic composition of the residual carbonate in both layers should be very similar. The fact that they are not, makes any subsequent inferences based on the data provided in the Treiman (2003) Table 1 questionable. Treiman (2003) does suggest that the presence of other mineral phases in the carbonate grains analyzed could account for such inconsistencies, however no other investigation of ALH84001 carbonate has documented such phases at more than trace levels. This extreme difference in residual carbonate composition can be used to completely negate the Treiman (2003) equilibrium model for siderite decomposition.

4.2.2.6. *Inferred volume abundances of magnetite in magnetite-bearing layers.* Assuming all the magnetite present in the inner and outer magnetite rich rims are the products of partial thermal decomposition, and that these magnetites are essentially stoichiometric pure  $\text{Fe}_3\text{O}_4$ , then the initial composition of the carbonate prior to decomposition would

have had a higher siderite content and a correspondingly lower magnesite content than the remaining residual carbonate. If we let the composition of the initial carbonate be  $\text{Fe}_{x_0} \text{Mg}_{(1-x_0)} \text{CO}_3$ , and the composition of the residual carbonate be  $\text{Fe}_{x_1} \text{Mg}_{(1-x_1)} \text{CO}_3$ , then the relevant chemical reaction is:



where  $\alpha = \left(\frac{1-x_0}{1-x_1}\right)$  and  $\beta = \frac{1}{3} \cdot \left(\frac{x_0-x_1}{1-x_1}\right)$ . Several important observations can be immediately deduced:

- The number of moles of Fe and Mg in both the initial carbonate, and the carbonate–magnetite product are equivalent. Hence, the composition of the initial carbonate can be directly determined from the bulk composition of the carbonate–magnetite product.
- The number of moles and hence volumes of the residual carbonate and magnetite products are strictly bound by the mole fraction of Fe in the initial and residual carbonates (i.e.,  $x_0$  and  $x_1$ ).
- The greater the proportion of magnetite product the smaller the mole fraction of Fe in the residual carbonate since  $1 > x_0 > x_1 > 0$ .

If we let  $V_0$  and  $V_1$  be the initial and residual volumes of carbonate,  $V_2$  be the volume of magnetite,  $V_3$  be the void space volume (since  $V_0 > V_1 + V_2$ ) and  $V_{\text{FeCO}_3}^\ominus$ ,  $V_{\text{MgCO}_3}^\ominus$  and  $V_{\text{Fe}_3\text{O}_4}^\ominus$  are the molar volumes of siderite, magnesite and magnetite respectively (see Table 8) then from reaction (20) it is easy to show that:

$$\begin{aligned} V_0 &= x_0 \cdot V_{\text{FeCO}_3}^\ominus + (1-x_0) \cdot V_{\text{MgCO}_3}^\ominus \\ V_1 &= \alpha \cdot (x_1 \cdot V_{\text{FeCO}_3}^\ominus + (1-x_1) \cdot V_{\text{MgCO}_3}^\ominus) \\ V_2 &= \frac{\beta}{3} \cdot V_{\text{Fe}_3\text{O}_4}^\ominus \\ V_3 &= V_0 - V_1 - V_2 \end{aligned} \quad (21)$$

Table 8  
Molar volumes of siderite, magnesite, and magnetite.

Species	$V^0$ ( $\times 10^{-5} \text{ m}^3$ )
$\text{FeCO}_3$	2.938
$\text{MgCO}_3$	2.803
$\text{Fe}_3\text{O}_4$	4.452

From the Eq. (21) the fractional volume of magnetite,  $V_{\text{Fe}_3\text{O}_4}^{\text{Fraction}}$ , in the final residual carbonate–magnetite assemblage is given by:

$$V_{\text{Fe}_3\text{O}_4}^{\text{Fraction}} = \frac{V_2}{V_1 + V_2} = \frac{V_{\text{Fe}_3\text{O}_4}^{\ominus} \cdot (x_0 - x_1)}{V_{\text{Fe}_3\text{O}_4}^{\ominus} \cdot (x_0 - x_1) + 3 \cdot (1 - x_0) \cdot (x_1 \cdot V_{\text{Fe}_3\text{O}_3} + (1 - x_1) \cdot V_{\text{MgCO}_3}^{\ominus})} \quad (22)$$

Taking the inferred compositions of the initial and residual ALH84001 carbonate in the inner and outer rims from Tables 1 and 2 of Treiman (2003) we find that the fractional volume of magnetite inferred to be present in the outer rim to be only ~15% and only ~43% in the inner rim (Table 7). These values are inconsistent with any magnetite rim abundances reported in the literature, based on our observations, the volume fraction magnetite in these rims typically lies in the range of 50–70%. This again suggests the data provided by Tables 1 and 2 of Treiman (2003) are too inaccurate to be useful in elucidating the origin of magnetite. This simple mass balance treatment shows that the magnetite in the rims could not have formed from an initial carbonate composition now reflected by the assumed post-decomposition residual carbonate. The decomposition hypothesis cannot explain the data in Treiman (2003).

#### 4.3. Conflicting experimental observations

Two sets of direct experimental observations indicate a significant fraction of magnetites in ALH84001 carbonate arguably could not have formed by either the Brearley (2003) or Treiman (2003) models. These observations are:

- Magnetites embedded within the magnesite layer separating the inner and outer magnetite rich bands (e.g., Fig. 3G).
- Chemically impure magnetites with minor to trace amounts of Cr and/or Al (Fig. 5C).

In the first case, since the carbonate in the magnesite layer is essentially free of Fe, there is no siderite with which to decompose to form magnetite. In the second case since neither Cr nor Al can substitute into the trigonal ( $R\bar{3}c$ ) structure of carbonate, thermal decomposition of carbonate alone cannot form magnetites with these elemental impurities. While we note that Treiman (2003) does allude to the presence of “smectite or Fe-oxyhydroxide adhering to the grains’ irregularities”, we have not observed any evidence of such surface coating in any TEM imaging of embedded

magnetites. If such coating were the source of the observed Cr and/or Al then they would need to be relatively thick and would be obvious, even in casual observation.

#### 4.4. Thermal decomposition studies of sideritic carbonates

Carbonate solid solutions between siderite and magnesite, rhodochrosite, and calcite can be viewed as the interpenetration, on an atomic scale, of two chemically different but structurally similar lattices (i.e., calcite;  $R\bar{3}c$ ). For ionic systems such as the carbonate minerals, the limits of solubility generally correlate with the relative size of the ions and their electrical charge in accordance with the Hume–Rothery rules (Hume–Rothery et al., 1969). Since the ionic radii for octahedrally coordinated  $\text{Mg}^{2+}$ ,  $\text{Mn}^{2+}$ , and  $\text{Fe}^{2+}$  are all similar (Table 9) they demonstrate complete solid solution series in essentially all geological environments. In the case of  $\text{Ca}^{2+}$ , where the mismatch in radii is greater than ~10%, solid solutions within the calcite crystal structure are only possible over a relatively limited compositional range.

##### 4.4.1. Prior studies

Thermal decomposition of mixed cation (Mg,Ca,Mn)-siderites have been investigated under a wide variety of conditions, not only because of their geochemical importance, but also because they provide a convenient synthetic route to the preparation of complex metal oxides via the so-called ‘solid-solution-precursor’ method (Vidyasagar et al., 1984; Vidyasagar et al., 1985). The results of such studies are summarized in Table 6 and invariably demonstrate that thermal decomposition yields a mixed metal oxide phase as the product<sup>17</sup>. In general, substitution of  $\text{Fe}^{2+}$  by  $\text{Mg}^{2+}$  or  $\text{Mn}^{2+}$  in siderite increases its thermal stability (Dubrawski, 1991a; Dubrawski, 1991b), generally to a far greater extent than thermodynamic factors alone could account for. Furthermore, thermogravimetric analysis demonstrates that decomposition is accompanied by only a single endothermic peak (Dubrawski, 1991b) indicating the siderite component of the solid solution does not decompose independently.

##### 4.4.2. Thermal decomposition of Roxbury siderite

Roxbury siderite represents a good terrestrial analog to the siderite-rich carbonate compositions suggested by Treiman (2003) to have decomposed to form the magnetite rich bands of the ALH84001 carbonates. Lane and Christensen

Table 9  
Crystal and ionic radii for octahedral  $\text{Mg}^{2+}$ ,  $\text{Mn}^{2+}$  and  $\text{Fe}^{2+}$ .

Cation (VIII coord.)	Crystal radius (nm)	Ionic radius (nm)
$\text{Mg}^{2+}$	0.103	0.089
$\text{Ca}^{2+}$	0.126	0.112
$\text{Mn}^{2+}$	0.111	0.096
$\text{Fe}^{2+}$	0.106	0.092

<sup>17</sup> In this respect, it is worth re-emphasizing that not only do (Mg,Mn)-siderites form a continuous substitutional solid solution series (magnesiumsiderite manganosiderite), but so do the intermediate (Mg,Mn)-Fe-monoxides (magnesiowustite manganowustite) and product (Mg,Mn)-spinel (magnesioferrite manganoferrite).

(1997) reported the bulk composition of Roxbury siderite as  $(\text{Fe}_{0.84}\text{Mg}_{0.10}\text{Mn}_{0.04}\text{Ca}_{0.02})\text{CO}_3$ , based on electron microprobe analyses at a maximum spatial resolution of  $\sim 1 \mu\text{m}$ . High resolution TEM characterization at the sub-micron scale however, indicates significant deviations in Fe:Mg ratio from the bulk composition, correlating with grain size. The fine grain ( $< 100 \text{ nm}$ ) component is Mg-poor (Fe:Mg  $> 20:1$ ) while, by comparison, the coarse grained component is Mg-rich (Fe:Mg  $< 8:1$ ) (see Fig. 6A). In both cases Mn and Ca appeared relatively uniform in composition.

Carbonate decomposition under both ‘slow’ and ‘fast’ heating resulted in the formation of impure Fe-oxides or ferrites (Figs. 6C and 6F). The only significant difference between the samples was the degree to which the carbonate had undergone decomposition. In the ‘slow’ heated sample no residual carbonate remained (Figs. 6B and 6C). In the ‘fast’ heated<sup>18</sup> sample only the very upper surface of the siderite exposed to laser heating underwent complete decomposition to ferrites (Figs. 6E and 6F), while the underlying carbonate phase, although heavily vesiculated, contained no ferrites (Fig. 6G). This observation is in sharp contrast to the magnetite rich rims and veins of ALH84001 carbonate disks that are characterized by an intimate mixture of magnetites embedded in a host carbonate matrix. The absence of any co-mixed carbonate/ferrite zone in our experiments is consistent with the proposed decomposition mechanism of siderite involving the endothermic formation of a wüstite (FeO) intermediate that is rapidly oxidized in an exothermic reaction to produce the  $\text{Fe}_3\text{O}_4$  product.

In products produced by both ‘slow’ and ‘fast’ heating, the Mg content of the mixed ferrite varied from one crystal to another (Figs. 6C and 6F) while the Mn content remained relatively constant. However, since this compositional distribution appeared to mirror that of the unheated carbonate we believe this is simply a reflection of the initial Mg and Mn content of the carbonate (notably, in the product phases produced by both ‘slow’ and ‘fast’ heating we did not find any evidence for discrete periclase or lime).

*4.4.2.1. Comparison to decomposition studies of Copper Lake siderite.* Golden et al. (2006) have recently reported they were able to produce almost pure nanophase magnetite from the slow thermal decomposition of a natural siderite from Copper Lake, Nova Scotia. From these results, they have argued for an “exclusively inorganic origin” for magnetite in ALH84001. Clearly these results would appear to be in stark conflict with both prior literature (see Table 6), and the results from the Roxbury siderite studies

reported here<sup>19</sup>; both of which find that the thermal decomposition of a mixed cation siderite *invariably* results in the formation of mixed cation magnetite. We suggest, however, that the *results* obtained by Golden et al. (2006) are in fact entirely consistent with prior literature and the Roxbury siderite studies – it is only the interpretation of these results by Golden et al. (2006) that is flawed.

To illustrate this, it is first necessary to review the materials and methods used by Golden et al. (2006). The natural siderite used for their experiments was from Copper Lake, Antigonish County, Nova Scotia and is reported to have a bulk chemical composition of  $(\text{Fe}_{0.643}\text{Mg}_{0.345}\text{Mn}_{0.012})\text{CO}_3$  (Golden et al., 2006). This siderite was partially decomposed in an evacuated sealed quartz tube by controlled heating, both in the presence of, and absence of, a natural pyrite containing minor silicate inclusions. The heating profile used was a slow temperature ramp ( $1 \text{ K} \cdot \text{min}^{-1}$ ) from ambient up to 623 K for nine days before then cooling back again to ambient. Since the siderite only underwent partial decomposition to magnetite the residual carbonate was removed by dissolution in “20% acetic acid followed by multiple washings with distilled  $\text{H}_2\text{O}$ .” The chemical composition of the remaining magnetite was then determined using TEM/EDX. In their results they report that Copper Lake siderite in the absence of pyrite produced magnetite containing only 7.1 mol.% Mg, while siderite in the presence of pyrite produced chemically pure magnetite ( $< 1 \text{ mol.}\%$  Mg). At this point it is necessary to inject a few observations. It is clear that while the bulk composition of Copper Lake siderite may contain 34.5 mol.% Mg it cannot have been homogeneously distributed, since if it was there would be a single decomposition temperature associated with the siderite, and after nine days it would have either all decomposed or not decomposed at all. Though it could be argued that re-equilibration, by solid state cation diffusion, of Mg between magnetite product and unreacted carbonate could have lead to the thermal stabilization of the residual carbonate by increasing its Mg mole fraction, such cation diffusion at 623 K would not have been sufficiently facile to allow such a process (as discussed earlier). Fortunately, the issue of the compositional homogeneity of Copper Lake siderite was reported previously by Bell (2007), who is affiliated with the same research group as Golden et al. (2006) and so presumably used the same parent siderite sample.<sup>20</sup> Fig. 7F taken from Fig. 3A, 3B–3G of Bell (2007) illustrates the variation of Mg and Fe abundances in a single grain surface  $\sim 175 \times 175 \mu\text{m}$  of Copper Lake siderite. In this single region, there are at least three distinct carbonate compositions as illustrated in the histogram shown in Fig. 7F. More importantly, one of these carbonate compositions is nearly pure siderite with only minor to trace Mg. Turning back to the decomposition experiments of Golden et al. (2006) it is clear that decomposition of Copper Lake

<sup>18</sup> “The use of high-power lasers with short wavelengths allows generation of the most extreme shock pressures in laboratories, but only in conjunction with extremely short pulse durations in the nanoseconds range. Laser irradiation shock experiments may be regarded as adequate simulations of hypervelocity impacts of microgram-mass micrometeorites onto atmosphere-free bodies such as the Moon as well as onto spacecraft” from Langenhorst et al. (2002).

<sup>19</sup> The “slow” heating studies of Roxbury siderite were conducted under essentially analogous conditions to those used by Golden et al. (2006).

<sup>20</sup> This is consistent with the observation that both report identical compositions for their bulk Copper Lake siderite.

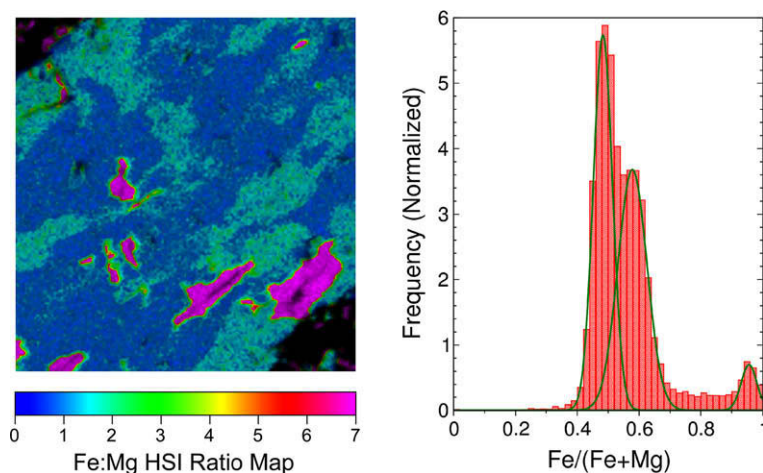


Fig. 7F. Compositional variability of siderite–magnesite solid solutions in a single grain of Copper Lake siderite, data taken from Figs. 3b and c of Bell (2007). The image on the left is a Hue–Saturation–Intensity (HSI) element ratio map for Fe:Mg (see Bensen and Lechene (2005)). The respective Fe and Mg signal intensities are derived from the grey-scale image pixel values of the electron microprobe Fe and Mg element maps shown in Fig. 3b and c of Bell (2007). Since neither electron microprobe map has an accompanying calibrated intensity scale the Fe:Mg values shown for the HSI image represents relative values and so are not absolute. In the HSI image, each pixel has a color determined by value of the Fe:Mg ratio, while the intensity, or brightness, is proportional to the significance of that ratio as determined by the combined intensities of the Fe and Mg pixels in the respective electron microprobe maps. Pixels with low intensities appear darker and pixels with high intensities appear brighter. Three distinct solid-solution compositions for carbonate are apparent. This includes an almost pure siderite component colored pink-purple which is encapsulated by two, more magnesite rich, solid solutions colored blue and green. On the right is a normalized histogram of the Fe:(Fe + Mg) ratios calculated for each grey-scale pixels in the respective electron microprobe maps. Again three distinct distributions are clearly apparent as indicated by the three Gaussian curves shown in green. As with the HSI image the values of Fe:(Fe + Mg) ratios are relative and not absolute. The bulk composition of Copper Lake siderite has been previously reported as  $(\text{Fe}_{0.643}\text{Mg}_{0.345}\text{Mn}_{0.012})\text{CO}_3$  (Golden et al., 2006). (For interpretation of the references to color in this figure legend, the reader is referred to the web version of this paper.)

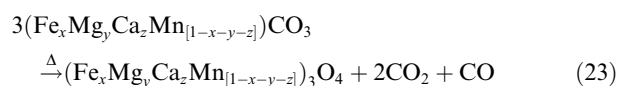
siderite will thus occur in a number of stages with increasing temperature, corresponding to the successive decomposition of progressively more Mg-rich carbonate components. At a temperature of 623 K only the stability field of the most Mg-poor siderite would have been crossed, resulting in the formation of a magnetite product that predictably has only a low Mg abundance. This is completely consistent with prior literature and the siderite decomposition studies reported here. That Golden et al. (2006) failed to fully characterize, or even take into consideration, the composition of their starting materials or determine the fraction of siderite that underwent decomposition or the fraction and composition of the residual carbonate, seem to invalidate any of their interpretations or conclusions.

#### 4.5. Implications and origins of ALH84001 magnetites

The majority of ALH84001 magnetites are stoichiometrically pure  $\text{Fe}_3\text{O}_4$  embedded within all compositions of carbonate ranging from the most Fe-rich ( $(\text{Fe}_{0.60}\text{Mg}_{0.16}\text{Ca}_{0.05}\text{Mn}_{0.04})\text{CO}_3$ ) at the boundary of the inner and outer cores to the most Fe-free magnesite ( $(\text{Mg}_{0.95}\text{Ca}_{0.05})\text{CO}_3$ ). It is difficult to suggest a process by which this magnesite has undergone thermal decomposition to produce chemically pure magnetite based on results from experiments in Table 6 and those of the Roxbury siderite decomposition studies reported here. Only a small fraction of Martian magnetite crystals are chemically impure; they contain trace to minor amounts of Cr (Fig. 5C) and/or Al (Thomas-

Keprta et al., 2000a). Clearly these chemically impure magnetites have detrital origins and did not form as a consequence of thermal decomposition of host carbonate which lacks detectable Cr and/or Al.

Although the “thermal decomposition” hypothesis for the observation of chemically pure magnetites in the rims of ALH84001 carbonate disks appears, on the surface, to provide a simple inorganic explanation of the observations, theoretical and experimental evaluation indicates it is not applicable to the formation of the vast majority of the magnetites in ALH84001 carbonate disks (Table 10). As discussed at length previously, both the Brearley (2003) and Treiman (2003) hypotheses proposed to explain the presence of ALH84001 magnetite are flawed. The importance of experimental data therefore cannot be overestimated. We can summarize the experimental studies of decomposition of a mixed cation siderite with the following generalized reaction:



While it is impossible to completely discount that some of the magnetites embedded in ALH84001 carbonates might be a product of thermal decomposition, we argue at best this can only account for a tiny portion. Consequently, this should not divert our attention from understanding the origin of the remaining majority of magnetites that would appear to have been derived from a detrital or allochthonous

Table 10  
Features in ALH84001 inconsistent with carbonate decomposition.

ALH84001 observations	Incompatibility with partial thermal carbonate decomposition
Micron scale isotopic and chemical heterogeneity present in carbonate disks, e.g., Valley et al. (1997), Saxton et al. (1998), Eiler et al. (2002), McKay et al. (1996) and this study	Increased cation diffusion at high temperatures would have erased chemical and isotopic gradients observed in the carbonate.
$^{40}\text{Ar}/^{39}\text{Ar}$ chronometer in ALH84001 feldspathic glass last reset $\sim 4$ Ga (Weiss et al., 2002)	Heating above the Ar release temperature, $\sim 350\text{--}500$ °C, after 4 Ga would have reset $^{40}\text{Ar}/^{39}\text{Ar}$ chronometer.
Chemically pure magnetites present within all ALH84001 carbonate compositions including those contain no Fe (this study)	Breakdown temperature for thermal decomposition of Fe-containing carbonates to magnetite is a function of cation composition; the differing carbonate compositions in ALH84001 require different and incompatible temperature constraints. Magnetite cation composition reflects that of the carbonate from which it forms, i.e., chemically pure magnetite requires decomposition of chemically pure siderite. Magnetites present within the magnesite rim cannot have formed by magnesite decomposition since it contains no Fe.
A fraction of magnetites present in rim and core carbonate contain minor Cr and/or Al, e.g., Thomas-Keprta et al. (2000a) and this study.	Cr and Al cations cannot substitute in to Fe–Mg–Ca carbonate, therefore the Cr and/or Al containing magnetites could not have formed from decomposition of host carbonate.
Absence of graphite within carbonate disks, e.g., McKay et al. (1996), Flynn et al. (1998), Flynn et al. (1999), Clemett et al. (1998) and this study.	Under thermodynamic equilibrium graphite is a preferred product of siderite decomposition. Presence of nanophase magnetite catalyst would help to lower kinetic barriers for graphite precipitation.
Some magnetites embedded within carbonate show evidence of surrounding void space, e.g., Barber and Scott (2002), Brearley (2003) and this study.	Volume change associated with carbonate decomposition to magnetite too large to account for observed void sizes, while many magnetites lack any association with void spaces.

source (Table 11). There are no convincing data showing that they originated from the carbonate. Although we have not attempted to present a detailed model for a detrital origin of ALH84001 magnetite, we have highlighted the presence of many features consistent with exposure of the carbonates to aqueous fluids after formation (Table 11).

Table 11  
ALH84001 features in ALH84001 consistent with allochthonous magnetite.

ALH84001 observations	Implications
Chemically pure magnetites embedded within a diverse range of carbonate compositions, including magnesite that contains no Fe (this study)	Embedding carbonate is not the progenitor of the magnetite – detrital magnetite incorporated during disk formation.
Fine-grained, S-containing, veins that cross-cut core carbonate (this study).	Influx of a sulfurous fluid(s) after carbonate disk formation.
Ferrihydrite embedded within fissures in the magnesite band (this study).	Influx of ferrous–ferric fluid(s) after carbonate disk formation.
Magnetites containing minor Cr and/or Al present in rim and core carbonate (Thomas-Keprta et al. (2000a) and this study).	Embedding carbonate is not the progenitor of the magnetite – detrital magnetite incorporated during disk formation.
Amorphous Si present in nanophase carbonate magnetite-rich rim and veins (this study).	Influx of siliceous fluid(s) either concurrent with or subsequent to rim/vein formation.
Spatially association of abundant Fe-sulfides with magnetite-rich rims but their relative scarcity within magnetite-rich veins (this study).	Influx of a sulfurous fluid(s) after carbonate disk formation.
Presence of void space associated with some magnetites embedded within both core carbonate and the magnesite band (Barber and Scott (2002), Brearley (2003), and this study). Presence of void space associated with some magnetites located at the interface of carbonate grains (this study).	Carbonate recrystallization enables migration of imperfections, such as magnetite and void spaces are to grain boundaries. (Conversely such spatial associations may simply be coincidental, e.g., void spaces are associated with magnetites in the magnesite band, but these magnetites could not have been produced by magnesite thermal decomposition.)

## 5. SUMMARY AND CONCLUSIONS

Two heating scenarios described herein provide the geological context for the decomposition models developed independently by Brearley (2003) and Treiman (2003). These models are contradictory; that is, they cannot both

have occurred since application of one model negates the applicability of the other. The first is based on carbonate decomposition occurring under “extreme disequilibrium conditions” in which “kinetics are the dominant controlling factor” determining the chemical and physical nature of the magnetites that are formed. Although never explicitly addressed, this model is most consistent with the impact event that ejected ALH84001 from Mars. In the second model, carbonate decomposition occurs “at some depth beneath the Martian surface where the pressure was greater than the atmospheric pressure and the temperature declined slowly.” However, based on kinetic and thermodynamic arguments, both models proposed for the high temperature, inorganic formation of ALH84001 magnetite would not have produced the results observed in ALH84001 carbonate disks.

ALH84001 carbonate assemblages can be best explained as the result of low temperature, disequilibrium precipitation from a single fluid with variable composition or from multiple fluids. Nanophase magnetite and Fe-sulfides were suspended in fluids that formed the disk cores and rims. After deposition ALH84001 carbonate disks were exposed to multiple fluids containing amorphous silica, additional nanophase magnetite, and S- and Fe-rich phases, some of which were deposited in veins. While the majority of ALH84001 magnetites were deposited in silica enriched rims and veins, some are also distributed throughout the cores and within the magnesite bands. Most magnetites are chemically pure, although a few contain minor Al/Cr. Their presence is inconsistent with formation by thermal decomposition of their host carbonate. We suggest that the majority of ALH84001 magnetites has an allochthonous origin and was added to the carbonate system from an outside source. This origin does not exclude the possibility that a fraction is consistent with formation by biogenic processes, as proposed in previous studies.

#### ACKNOWLEDGEMENTS

We acknowledge support from the NASA Mars Fundamental program. We thank FEI Corporation, particularly Trisha Rice and Lucille Giannuzzi, for assistance in preparing the FIB sections of ALH84001 carbonate disks. We also acknowledge Giles Graham for assistance with preparing the Texas FIB sections. We gratefully acknowledge the support of Sean and Nathaniel Keprta and Miss B. and O. Clemett. We thank two anonymous reviewers and Christian Koeberl for suggestions that greatly improved this paper.

#### APPENDIX A. SUPPLEMENTARY DATA

Supplementary data associated with this article can be found, in the online version, at doi:10.1016/j.gca.2009.05.064.

#### REFERENCES

- Bagin V. I., Gendler T. S., Rybak R. S. and Kut'min R. N. (1974) Transformation temperatures of the natural solid solution (Fe,Mg)CO<sub>3</sub>. *Izv. Russ. Acad. Sci. Phys. Solid Earth* **6**, 73–84.
- Barber D. J. and Scott E. R. D. (2002) Origin of supposedly biogenic magnetite in the Martian meteorite Allan Hills 84001. *Proc. Natl. Acad. Sci. USA* **99**, 6556–6561.
- Bell M. S. (2007) Experimental shock decomposition of siderite and the origin of magnetite in Martian meteorite ALH84001. *Meteorit. Planet. Sci.* **42**, 935–949.
- Bensen, D. and Lechene, C. P. (2005) Quantitating MIMS ratios using Hue, Saturation, and Intensity displays. In *Fifteenth International Conference on Secondary Ion Mass Spectrometry*, Manchester, UK, p. 269.
- Borg L. E., Connelly J. N., Nyquist L. E., Shih C.-Y., Wisemann H. and Reese Y. (1999) The age of carbonates in Martian meteorite ALH84001. *Science* **286**, 90–94.
- Bradley J. P., Harvey R. P. and McSween J. H. Y. (1996) Magnetite whiskers and platelets in the ALH84001 Martian meteorite: evidence of vapor phase growth. *Geochim. Cosmochim. Acta* **60**, 5149–5155.
- Brearley, A. J. (1998) Rare potassium-bearing mica in Allan Hills 84001: additional constraints on carbonate formation. *Martian meteorites: where do we stand and where are we going? Abstracts from a workshop*, p. 6.
- Brearley A. J. (2003) Magnetite in ALH 84001: an origin by shock-induced thermal decomposition of iron carbonate. *Meteorit. Planet. Sci.* **38**, 849–870.
- Cady S. L., Wenk H. R. and Downing K. H. (1996) HRTEM of microcrystalline opal in chert and porcelanite from Monterey Formation, California. *Am. Mineral.* **81**, 1380–1395.
- Chai L. and Navrotsky A. (1996a) Synthesis, characterization and enthalpy of mixing of the (Fe,Mg)CO<sub>3</sub> solid solution. *Geochim. Cosmochim. Acta* **60**, 4377–4383.
- Chai L. and Navrotsky A. (1996b) Synthesis, characterization, and energetics of solid solution along the dolomite-ankerite join, and implications for the stability of ordered CaFe(CO<sub>3</sub>)<sub>2</sub>. *Am. Mineral.* **81**, 1141–1147.
- Clemett, S. J., Dulay, M. T., Gillette, J. S., Chillier, X. D. F., Mahajan, T. B. and Zare, R. N. (1998) Evidence for the extraterrestrial origin of polycyclic aromatic hydrocarbons in the Martian meteorite ALH84001. *Chemistry and Physics of Molecules and Grains in Space. faraday Discussions No. 109*, pp. 417–436.
- Cohn, A. (2006) Formation of magnetite nanoparticles by thermal decomposition of iron bearing carbonates: implications for the evidence of fossil life on Mars. In *National Nanotechnology Infrastructure Network, Research Experience for Undergraduates, Accomplishments Program*, Cornell, NY, USA, pp. 58–59.
- de La Croix A., English R. B. and Brown M. E. (1998) Modeling the thermal decomposition of solids on the basis of lattice energy changes. *J. Solid State Chem.* **137**, 332–345.
- Dhupe A. P. and Gokarn A. N. (1990) Studies in the thermal decomposition of natural siderites in the presence of air. *Int. J. Miner. Process.* **20**, 209–220.
- Domeneghetti M. C., Fioretti A. M., Cámara F., Molin G. and Tazzoli V. (2007) Thermal history of ALH 84001 meteorite by Fe<sup>2+</sup>-Mg ordering in orthopyroxene. *Meteorit. Planet. Sci.* **42**, 1703–1710.
- Dubrawski, J. V. (1991a). Differential scanning calorimetry and its applications to mineralogy and the geosciences. In: *Thermal Analysis in the Geosciences, Lecture Notes in Earth Sciences* (eds. W. Smykatz-Kloss and S. St. J. Warne). Springer, Berlin/Heidelberg, pp. 16–59.
- Dubrawski J. V. (1991b) Thermal decomposition of some siderite-magnesite minerals using DSC. *J. Therm. Anal.* **37**, 1213–1221.
- Eiler J. M., Valley J. W., Graham C. M. and Fournelle J. (2002) Two populations of carbonate in ALH84001: geochemical evidence for discrimination and genesis. *Geochim. Cosmochim. Acta* **66**, 1285–1303.
- Fisler D. K. and Cygan R. T. (1998) Cation dissolution in calcite: determining closure temperatures and the thermal history for the Allan Hills 84001 meteorite. *Meteorit. Planet. Sci.* **33**, 785–789.

- Flynn G. J., Keller L. P., Jacobsen C. and Wirrick S. (1998) Carbon in Allan Hills 84001 carbonate and rim. *Meteorit. Planet. Sci.* **33**, A50–A51.
- Flynn, G. J., Keller, L. P., Jacobsen, C. and Wirrick, S. (1999) Organic carbon in Mars meteorites: a comparison of ALH84001 and Nakhla. *Lunar Planet. Sci. XXX Lunar Planet. Inst., Houston.* #1087 (abstr.).
- Folk, R. L. (1965) Some aspects of recrystallization in ancient limestones. *Society of Economic Paleontologists and Mineralogists Special publication 13*, pp. 14–48.
- Forster B., Van de Ville B., Berent J., Sage D. and Unser M. (2004) Complex wavelets for extended depth-of-field: a new method for the fusion of multichannel microscopy images. *Microsc. Res. Techniq.* **65**, 33–42.
- French B. M. and Eugster H. P. (1965) Experimental control of oxygen fugacities by graphite-gas equilibria. *J. Geophys. Res.* **70**, 1529–1539.
- Fritz J., Artemieva N. and Greshake A. (2005) Ejection of Martian meteorites. *Meteorit. Planet. Sci.* **40**, 1393.
- Fritz J., Greshake A. and Soffler D. (2004) Micro-Raman spectroscopy of plagioclase and maskelynite in Martian meteorites: evidence of progressive shock metamorphism. *Antarct. Meteorit. Res.* **18**, 96–116.
- Fritz, J., Greshake, A. and Stöffler, D. (2003) Launch conditions for Martian meteorites: plagioclase as a shock pressure barometer. *Lunar Planet. Sci. XXXIV.* Lunar Planet. Inst., Houston. #1355 (abstr.).
- Gallagher P. K. and Warne S. S. J. (1981a) Application of thermomagnetometry to the study of siderite. *Mater. Res. Bull.* **16**, 141–144.
- Gallagher P. K. and Warne S. S. J. (1981b) Thermomagnetometry and thermal decomposition of siderite. *Thermochim. Acta* **43**, 253–267.
- Galwey A. K. and Brown M. E. (1999) *Thermal Decomposition of Ionic Solids, 86: Studies in Physical and Theoretical Chemistry.* Elsevier Science, Amsterdam.
- Gasem K. A. M., Gao W., Pan Z. and Robinson R. L. J. (2001) A modified temperature dependence for the Peng-Robinson equation of state. *Fluid Phase Equilib.* **181**, 113–125.
- Geider S., Dussol B., Nitsche S., Veessler S., Berthéze P., Dupuy P., Astier J. P., Boistelle R., Berland Y., Dagorn J. C. and Verdier J. M. (1996) Calcium carbonate crystals promote calcium oxalate crystallization by heterogeneous or epitaxial nucleation: possible involvement in the control of urinary lithogenesis. *Calcified Tissue Int.* **59**, 33–37.
- Giannuzzi L. A. and Stevie F. A. (1999) A review of focused ion beam milling techniques for TEM specimen preparation. *Micron* **30**, 197–204.
- Golden, D. C., Ming, D. W., Lauer, H. V. J., Morris, R. V., Treiman, A. H. and McKay, G. A. (2006) Formation of “chemically pure magnetite from Mg–Fe carbonates: implications for the exclusively inorganic origin of magnetite and sulfides in Martian meteorite ALH84001. *Lunar Planet. Sci. XXXVII.* Lunar Planet. Inst., Houston. #1199 (abstr.).
- Gotor F. J., Macias M., Ortega A. and Criado J. M. (2000) Comparative study of the kinetics of the thermal decomposition of synthetic and natural siderite samples. *Phys. Chem. Miner.* **27**, 495–503.
- Hakonardottir, K. M., Hogg, A. J. and Johannesson, T. (2002) Flow of a granular avalanche over an obstacle. *Eur. Geophys. Union Gen. Assembly XXVII.* #1925 (abstr.).
- Harvey R. P. and McSween J. H. Y. (1996) A possible high-temperature origin for the carbonates in the Martian meteorite ALH84001. *Nature* **382**, 49–51.
- Holland T. and Powell R. (1998) An internally-consistent thermodynamic dataset for phases of petrological interest. *J. Metamorph. Geol.* **16**, 309–343.
- Huebner J. S. (1975) Oxygen fugacity values of furnace gas mixtures. *Am. Mineral.* **60**, 815–823.
- Hume-Rothery W., Smallman R. W. and Haworth C. W. (1969) *The Structure of Metals and Alloys.* Metals & Metallurgy Trust, London.
- Hurst H. J., Levy J. H. and Patterson J. H. (1993) Siderite decomposition in retorting atmospheres. *Fuel* **72**, 885–890.
- Isambert A., De Resseguier T., Gloter A., Reynard B., Guyot F. and Valet J.-P. (2006) Magnetite-like nanocrystals formed by laser-driven shocks in siderite. *Earth Planet. Sci. Lett.* **243**, 820–827.
- Isambert A. and Valet J.-P. (2003) Stable Mn-magnetite derived from Mn-siderite by heating in air. *Earth Planet. Sci. Lett.* **108**, EMP2-1–EMP2-9.
- Iwafuchi K., Watanabe C. and Otsuka R. T. (1983) Thermal decomposition of magnesian kutnahorite. *Thermochim. Acta* **60**, 361–381.
- Jagtap S. B., Pande A. R. and Gokarn A. N. (1992) Kinetics of thermal decomposition of siderite: effect of particle size. *Int. J. Miner. Process.* **36**, 113–124.
- Jurewicz, A. J. G., Lofgren, G. E., Williams, R. J., Lanier, A., Le, L., Carter, W., Wagstaff, J. and Roshko, A. (1993) NASA Johnson Space Center Technical Update: JSC system using a solid electrolytic cell in a remote location to measure oxygen fugacities in CO/CO<sub>2</sub> controlled-atmosphere furnaces, Houston, TX, USA.
- Karl S. and Deborah G. (2004) Petrographic and geochemical analysis of detrital magnetite of last Wisconsinan tills in eastern Indiana and western Ohio. *Geolog. Soc. Am. Abstr. Prog.* **36**, 48.
- Kennedy L. A. and White J. C. (2001) Low-temperature recrystallization in calcite: mechanisms and consequences. *Geology* **29**, 1027–1030.
- Kent A. J. R., Hutcheon I. D., Ryerson F. J. and Phinney D. L. (2001) The temperature of formation of carbonate in Martian meteorite ALH84001: constraints from cation diffusion. *Geochim. Cosmochim. Acta* **65**, 311–321.
- Kirschvink J. L., Maine A. T. and Vali H. (1997) Paleomagnetic evidence of a low-temperature origin of carbonate in the Martian meteorite ALH84001. *Science* **275**, 1629–1633.
- Kozioł, A. M. (2001) A siderite–magnesite decarbonation study. *Geological Society of America National Meeting*, Boston. #25840 (abstr.).
- Kozioł, A. M. and Brearley, A. J. (2002) A non-biological origin for the nanophase magnetite grains in ALH84001: experimental results. *Lunar Planet. Sci. XXXIII.* Lunar Planet. Inst., Houston. #1672 (abstr.).
- Kubas, Z. and Szalkowicz, M. (1971) Application of simultaneous differential thermal analysis, thermogravimetry and analysis of evolved gases to studies on kinetics and mechanism of complex reactions. *Thermal Analysis (Proc. of the 3rd ICTA, Davos, 1971)* **2**, 447–461.
- Lane M. D. and Christensen P. R. (1997) Thermal infrared emission spectroscopy of anhydrous carbonates. *J. Geophys. Res.* **102**, 25581–25592.
- Langenhorst F., Boustie M., Deutsch A., Hornemann U., Matignon C., Migault A. and Romain J. P. (2002) Experimental techniques for the simulation of shock metamorphism: a case study for calcite. In *High-Pressure Shock Compression of Solids V: Shock Chemistry with Application to Meteorite Impacts* (eds. L. Davison, Y. Horie and T. Sekine), pp. 1–27. High-Pressure Shock Compression of Solids V: Shock Chemistry with Application to Meteorite Impacts. Springer Materials, Berlin.

- Langenhorst, F., Shaw, C. S. J. and Metzler, K. (2000) Mineral chemistry and microstructures in ALH84001. *Lunar Planet. Sci. XXXI*. Lunar Planet. Inst., Houston. #1866 (abstr.).
- Lauer, H. V., Ming, D. W. and Golden, D. C. (2005) Thermal characterization of Fe<sub>3</sub>O<sub>4</sub> nanoparticles formed from poorly crystalline siderite. *Lunar Planet. Sci. XXXVI*. Lunar Planet. Inst., Houston. #2153 (abstr.).
- Lewis G. N. and Randall M. (1961) *Thermodynamics*, second ed. McGraw-Hill, New York.
- Mathews, J. H. and Fink, K. D. (2004) Solution of differential equations: predictor–corrector methods. In: *Numerical Methods using Matlab* (fourth ed.) Prentice-Hall Inc., Upper Saddle River, pp. 505–508. ISBN 0-13-065248-2.
- McCauley J. W. and Roy R. (1974) Controlled nucleation and crystal growth of various CaCO<sub>3</sub> phases by the silica gel technique. *Am. Mineral.* **59**, 947–963.
- McKay D. S., Gibson J. E. K., Thomas-Keprta K. L., Vali H., Romanek C. S., Clemett S. J., Chiller X. D. F., Maechling C. R. and Zare R. N. (1996) Search for past life on Mars: possible relic biogenic activity in Martian meteorite ALH84001. *Science* **273**, 924–930.
- McKay G., Schwandt C. and Mikouchi T. (1998) Feldspathic glass and silica in Allan Hills 84001. *Meteorit. Planet. Sci.* **33**, A102.
- McSween, J. H. Y. (2002) Basalt or andesite? A critical evaluation of constraints on the composition of the ancient Martian crust. *Lunar Planet. Sci. XXXIII*. Lunar Planet. Inst., Houston. #1062 (abstr.).
- McSween J. H. Y. and Harvey R. P. (1998) An evaporation model for formation of carbonates in the ALH84001 Martian meteorite. *Intl. Geol. Rev.* **40**, 774–782.
- McSween J. H. Y. and Treiman A. H. (1998) Martian meteorites. In *Planetary Materials: Reviews in Mineralogy* (ed. J. J. Papike). Mineralogical Society of America, Chantilly (chapter 6).
- McSwiggen P. L. (1993a) Alternative solution model for the ternary carbonate system CaCO<sub>3</sub>–MgCO<sub>3</sub>–FeCO<sub>3</sub>. Part 1. A ternary Bragg–Williams ordering model. *Phys. Chem. Miner.* **20**, 33–41.
- McSwiggen P. L. (1993b) Alternative solution model for the ternary carbonate system CaCO<sub>3</sub>–MgCO<sub>3</sub>–FeCO<sub>3</sub>. Part 2. Calibration of a combined ordering model and mixing model. *Phys. Chem. Miner.* **20**, 42–55.
- Mikouchi, T., Miyamoto, M., Koizumi, E., Makishima, J. and McKay, G. A. (2006) Relative burial depths of Nakhilites: an update. *Lunar Planet. Sci. XXVII*. Lunar Planet. Inst., Houston. #1865 (abstr.).
- Milodowski A. E., Morgan D. J. and Warne S. S. J. (1989) Thermal analysis of studies of the dolomite–ferroan dolomite–ankerite series. II. Decomposition mechanism in flowing CO<sub>2</sub> atmosphere. *Thermochim. Acta* **152**, 279–297.
- Min K. and Reiners P. W. (2006) High-temperature Mars-to-Earth transfer of meteorite ALH84001. *Earth Planet. Sci. Lett.* **260**, 72–85.
- Mittlefehldt, D. W. (1994a) ALH84001 cumulate orthopyroxenite; a previously unappreciated Martian meteorite. *Lunar Planet. Sci. XXV*. Lunar Planet. Inst., Houston. pp. 911–912.
- Mittlefehldt D. W. (1994b) ALH84001, a cumulate orthopyroxenite member of the Martian meteorite clan. *Meteoritics* **29**, 214–221.
- Muxworthy A. R. and Williams W. (2008) Critical superparamagnetic/single-domain grain sizes in interacting magnetite particles: implications for magnetosome crystals. *J. R. Soc. Interface*, ISSN 1742-5689.
- Nyquist L. E., Bogard D. D., Shih C.-Y., Greshake A., Stöffler D. and Eugster O. (2001) Ages and geologic histories of Martian meteorites. *Space Sci. Rev.* **96**, 105–164.
- Powell R., Holland T. and Worley B. (1998) Calculating phase diagrams involving solid solutions via non-linear equations with examples using THERMOCALC. *J. Metamorph. Geol.* **16**, 577–588.
- Razjigaeva N. G. and Naumova V. V. (1992) Trace element composition of detrital magnetite from coastal sediments of northwestern Japan sea for provenance study. *J. Sediment. Res.* **62**, 802–809.
- Reid R. P. and Macintyre I. G. (1998) Carbonate recrystallization in shallow marine environments: a widespread diagenetic process forming micritized grains. *J. Sediment. Res.* **68**, 928–946.
- Romanek C. S., Grady M. M., Wright I. P., Mittlefehldt D. W., Socki R. A., Pillinger C. T. and Gibson J. E. K. (1994) Record of fluid-rock interactions on Mars from the meteorite ALH84001. *Nature* **372**, 655–657.
- Saxton J. M., Lyon I. C. and Turner G. (1998) Correlated chemical and isotopic zoning in carbonates in the Martian meteorite ALH84001. *Earth Planet. Sci. Lett.* **160**, 811–822.
- Scott E. R. D., Krot A. N. and Yamaguchi A. (1997) Formation of carbonates in Martian meteorite ALH84001 from shock melts. *Meteorit. Planet. Sci.* **32**, A117–A118.
- Shuster D. L. and Weiss B. P. (2005) Martian surface paleotemperatures from thermochronology of meteorites. *Science* **309**, 594–597.
- Stöffler D. (1982) Density of minerals and rocks under shock compression. In *Landolt-Börnstein: Numerical Data and Functional Relationships in Science and Technology* (ed. K.-H. Hellwege), pp. 120–183. Landolt-Börnstein: Numerical Data and Functional Relationships in Science and Technology. Springer, Berlin/Heidelberg/New York.
- Stöffler, D. (2000) Maskelynite confirmed as diaplectic glass: indication for peak shock pressures below 45 GPa in all Martian meteorites. *Lunar Planet. Sci. XXXI*. Lunar Planet. Inst., Houston. #1170 (abstr.).
- Tamura Y. and Tabata M. (1990) Complete reduction of carbon dioxide to carbon using cation-excess magnetite. *Nature* **346**, 255–256.
- Thomas-Keprta K. L., Bazylinski B. A., Kirschvink J. L., Clemett S. J., McKay D. S., Wentworth S. J., Vali H., Gibson J. E. K. and Romanek C. S. (2000a) Elongated prismatic magnetite crystals in ALH84001 carbonate globules: potential Martian magnetofossils. *Geochim. Cosmochim. Acta* **64**, 4049–4081.
- Thomas-Keprta K. L., Clemett S. J., Bazylinski D. A., Kirschvink J. L., McKay D. S., Wentworth S. J., Vali H., Gibson J. E. K., McKay M. F. and Romanek C. S. (2001) Truncated hexa-octahedral magnetite crystals in ALH84001: presumptive biosignatures. *Proc. Natl. Acad. Sci. USA* **98**, 2164–2169.
- Thomas-Keprta K. L., Clemett S. J., Bazylinski D. A., Kirschvink J. L., McKay D. S., Wentworth S. J., Vali H., Gibson J. E. K. and Romanek C. S. (2002) Magnetofossils from ancient Mars: a robust biosignature in the Martian meteorite ALH84001. *Appl. Environ. Microbiol.* **68**, 3663–3672.
- Thomas-Keprta, K. L., Wentworth, S. J., McKay, D. S. and Gibson, J. E. K. (2000b) Field emission gun scanning electron microscopy (FEGSEM) and transmission electron (TEM) microscopy of phyllosilicates in Martian meteorites ALH84001, Nakhla, and Shergotty. *Lunar Planet. Sci. XXXI*. Lunar Planet. Inst., Houston. #1690 (abstr.).
- Treiman, A. H. (1997) Chemical disequilibrium in carbonate minerals of Martian meteorite ALH 84001: inconsistent with high formation temperature. *Lunar Planet. Sci. XXVIII*. Lunar Planet. Inst., Houston. #1192 (abstr.).
- Treiman A. H. (1998) The history of ALH 84001 revised: multiple shock events. *Meteorit. Planet. Sci.* **33**, 753–764.

- Treiman A. H. (2003) Submicron magnetite grains and carbon compounds in Martian meteorite ALH84001: inorganic, abiotic formation by shock and thermal metamorphism. *Astrobiology* **3**, 369–392.
- Trunin R. F., Gudarenko L. F., Zhernokletov M. V. and Simakov G. V. (2001) *Experimental Data on Shock Compression and Adiabatic Expansion of Condensed Matter*. Russian Federal Nuclear Center-VNIIEF, Sarov, Russia.
- Valley J. W., Eiler J. M., Graham C. M., Gibson, Jr., E. K., Romanek C. S. and Stolper E. M. (1997) Low-temperature carbonate concretions in the Martian meteorite ALH84001: evidence from stable isotopes and mineralogy. *Science* **275**, 1633–1638.
- van der Bogert, C. H., Schultz, P. H. and Spray, J. G. (1999) Experimental frictional heating of dolomitic marble: new insights for Martian meteorite Allan Hills 84001. *Lunar Planet. Sci. XXX*. Lunar Planet. Inst., Houston. #1970 (abstr.).
- Velbel M. A. (2007) Surface textures and dissolution processes of heavy minerals in the sedimentary cycle: examples from pyroxenes and amphiboles. In *Heavy Minerals in Use* (eds. M. A. Mange and D. T. Wright). Elsevier, Doorwerth, The Netherlands, pp. 113–150.
- Velbel M. A., Wentworth S. J., Thomas-Keprta K. L., Donatelle A. R. and McKay D. S. (2007) Microdenticles: aqueous corrosion textures on weathered chain silicates as terrestrial analogs of pyroxene alteration in Mars meteorites. *Meteorit. Planet. Sci.* **42**, 5172.
- Vidyaşagar K., Gopalakrishnan J. and Rao C. N. R. (1984) A Convenient route for the synthesis of complex metal oxides employing solid solution precursors. *Inorg. Chem.* **23**, 1206–1210.
- Vidyaşagar K., Gopalakrishnan J. and Rao C. N. R. (1985) Synthesis of complex metal-oxides using hydroxide, cyanide, and nitrate solid-solution precursors. *J. Solid State Chem.* **58**, 29–37.
- Viti C. and Frezzotti M.-L. (2001) Transmission electron microscopy applied to fluid inclusion investigations. *Lithos* **55**, 125–138.
- Ware S. S. J. and French D. H. (1984) The application of simultaneous DTA and TG to some aspects of oil shale mineralogy. *Thermochim. Acta* **76**, 179–200.
- Warren P. H. (1998) Petrologic evidence for low-temperature, possibly flood-evaporitic origin of carbonates in the ALH84001 meteorite. *J. Geophys. Res. [Planets]* **103**, 16759.
- Weiss B. P., Kirshvink J. L., Baudenbacher F. J., Vali H., Peters N. T., MacDonald F. A. and Wikswo J. P. (2000) A low temperature transfer of ALH84001 from Mars to Earth. *Science* **290**, 791–795.
- Weiss B. P., Shuster D. L. and Stewart S. T. (2002) Temperatures on Mars from  $^{40}\text{Ar}/^{39}\text{Ar}$  thermochronology of ALH84001. *Earth Planet. Sci. Lett.* **201**, 465–472.
- Zakharov V. Y. and Adonyi Z. (1986) Thermal decomposition kinetics of siderite. *Thermochim. Acta* **102**, 101–107.
- Zenobi R., Zhan Q. and Voumard P. (1995) Multiphoton ionization spectroscopy in surface analysis and laser desorption mass spectrometry. *Microchim. Acta* **124**, 273–281.
- Zuilen M. A., Lepland A. and Arrhenius G. (2002) Reassessing the evidence for the earliest traces of life. *Nature* **418**, 627–630.

Associate editor: Christian Koeberl